

QC851
.C47
NO.33
ARCHIVE

ISSN No. 0737-5352-33

OPTICAL MEASUREMENTS OF AEROSOL SIZE
DISTRIBUTIONS IN GREAT SMOKY MOUNTAINS
NATIONAL PARK: PARTICLE HYGROSCOPICITY AND
ITS IMPACT ON VISIBILITY

Rodger B. Ames and Sonia M. Kreidenweis

Department of Atmospheric Science
Colorado State University
Fort Collins, CO

Funding Agency:
National Park Service # 1443-CA0001-92-006 96.5

August, 1996

CIRA Cooperative Institute for Research in the Atmosphere

**Colorado
State
University**

ABSTRACT

Aerosol size distributions were measured during the 1995 Southeastern Aerosol and Visibility Study (SEAVS) in Great Smoky Mountains National Park using a PMS ASASP-X optical aerosol spectrometer. Ambient aerosol was conditioned in a relative humidity (RH) controlled inlet before sampling. 130 dry ($RH \leq 15\%$) and 112 humidified aerosol size distributions, plus 24 distributions at ambient RH, were recorded during daylight hours for aerosol in the size range $0.1 < D_p < 2.5 \mu\text{m}$. Particle light scattering from the ASASP-X was inverted to particle sizes using Mie theory and applying a refractive index of either 1.530-0i or 1.501-0i for dry conditions, depending on the ambient aerosol chemical composition. A dry aerosol volume concentration time line from this work, when compared with a similar time line of aerosol mass concentration from IMPROVE samplers, indicates the ASASP-X provided a reliable representation of temporal trends in the ambient aerosol loading. The median dry aerosol geometric mass mean diameter measured during SEAVS was $0.28 \mu\text{m}$, with a range from 0.24 to $0.38 \mu\text{m}$, and median geometric standard deviation of 1.64. Sequential dry and humidified aerosol size distributions were corrected for refractive index dependence on RH and used to derive ambient aerosol hygroscopicity as a function of RH. This work demonstrates that experimentally derived water absorption is equivalent to or less than predicted by theory, assuming ambient aerosol water uptake is dictated by ionic compounds that have a chemical composition consistent with the particle fine mass measured during SEAVS. In this work, special consideration is given to the uncertainty in derived aerosol water contents and the degree to which this uncertainty propagates to estimates of light scattering. An ultimate goal of this project is to augment visibility and radiative transfer models through a better understanding of how RH affects the ambient aerosol size distribution in the southeastern U.S.



U18401 5741174

ACKNOWLEDGMENTS

We would like to thank the following people at Colorado State University for their support in this work: Derek Day, Jennifer Hand, Dr. Dave Rogers and Brian Jesse.

We would also like to thank the following people at the Air Quality Division of the National Park Service/CIRA for their assistance: Dr. William Malm and Dr. Jim Sisler.

Finally, our we would like to express our appreciation to Air Resource Specialists Inc. for providing support in the field and individually Roger Tree for his technical assistance.

This research was supported by the National Park Service under contract number 1443-CA0001-92-006 95.6.

TABLE OF CONTENTS

ABSTRACT	ii
ACKNOWLEDGMENTS	iii
TABLE OF CONTENTS	iv
LIST OF TABLES	vi
LIST OF FIGURES	vii
CHAPTER 1. INTRODUCTION	1
CHAPTER 2. BACKGROUND	4
2.1 Particle Light Scattering	7
2.2 Aerosol Hygroscopicity	10
2.3 Optical Particle Counter	13
2.4 Aerosol Size Distribution Statistics	15
CHAPTER 3. NPS/CSU SPECIAL STUDY	17
3.1 Objectives	17
3.2 Local and Synoptic Meteorology During SEAVS	17
3.3 RH Controlled Experimental Design	20
3.3.1 Aerosol Inlet	20
3.3.2 PMS ASASP-X	24
3.3.3 Associated Instruments	26
3.4 Sampling Protocol	26
CHAPTER 4. RESULTS	28
4.1 ASASP-X Dry Aerosol Characterization	28
4.2 Aerosol Water Uptake	34
4.3 Derived Wet-to-Dry Aerosol Diameter Ratios	43
4.4 Uncertainty Analysis	48
4.5 Uncertainty Propagation in a Light Scattering Model	52
CHAPTER 5. DISCUSSION	53
5.1 Dry Aerosol Volume and Density	53
5.2 Derived Aerosol Hygroscopicity	60
CHAPTER 6. CONCLUSION	65
CHAPTER 7. FUTURE WORK	68
REFERENCES	70

APPENDICES

A. SUMMARY OF EXPERIMENTAL DATA	
A.1 [CN] Data	74
A.2 Meteorological Data	74
A.3 Selected Chemical Data	79
A.4 Hurricane Erin Images	84
B. OPTICAL PARTICLE COUNTER CALIBRATION	
B.1 Field Calibration	86
B.2 ASASP-X Post Experiment Calibration	89
B.3 Establishing Unique Instrument Calibration Constants	94
C. OPTICAL PARTICLE COUNTER DATA REDUCTION	
C.1 ASASP-X Data Inversion Using Scattering Response Functions from Mie Theory	97
C.2 Transformation of Bin Data to Aerosol Distributions	102
C.3 Presentation of Aerosol Size Distributions	107
C.4 Data Acquisition and Processing Programs	109
D. PARTIAL MOLAR REFRACTIVE INDEX CALCULATIONS	
D.1 Partial Molar Volume Refractive Index Calculations for Dry and Humidified Aerosol	112
D.2 Conclusions	117
Oversized Table 4.2.1	119

LIST OF TABLES

CHAPTER 3	
3.2.1 Meteorological Periods During SEAVS	18
CHAPTER 4	
4.1.1 Dry Aerosol Size Distribution Statistics	32
4.1.2 Dry Aerosol Relative Humidity Statistics	34
4.2.1 Volume Distribution Parameters and Derived D/Do for the Entire Study	119
4.4.1 Sources of Uncertainty in ASASP-X Data	49
4.4.2 σ_m as a Function of Inversion Refractive Index	50
4.5.1 Uncertainty Propagation a Light Scattering Model	52
CHAPTER 5	
5.1.1 Dry Aerosol Density Derived from OPC and IMPROVE Data	58
5.1.2 Examples of Dry Density for Some Common Atmospheric Aerosols	59
APPENDIX A	
A.3.1 Equivalent Mass Factors Used for IMPROVE Data	80
APPENDIX B	
B.1.1 Field Calibration PSL Distribution Statistics	87
B.3.1 ASASP-X Calibration Constants	95
APPENDIX C	
C.1.1 Post Calibration RH Dependent Refractive Indices	98
C.1.2 ASASP-X Bin Diameters as a Function of RH	101
C.2.1 Description of Final Aerosol Distribution Bin Limits	104
C.2.2 Comparison of Particle Counts in Amplification Range Overlap	106

LIST OF FIGURES

CHAPTER 2	
2.1.1 b_{sp} vs. RH and MMD for Log-normal Aerosol Distributions	9
2.2.1 Size Change of an Ammonium Sulfate Particle with RH	11
CHAPTER 3	
3.3.1.1 Configuration of the ASASP-X Inlet During SEAVS	22
3.3.1.2 ASASP-X Inlet Efficiency	24
3.4.1 Plenum and ASASP-X Temperature and RH	27
CHAPTER 4	
Daily Averages of Dry Aerosol:	
4.1.1 Number Concentration	29
4.1.2 Volume Concentration	31
4.1.3 Mass Mean Diameter	31
4.1.4 Geometric Standard Deviation	31
Examples of Number and Volume Aerosol size Distributions for:	
4.2.1 JD 206	37
4.2.2 JD 207	38
4.2.3 JD 223	39
4.2.1 JD 226	40
4.2.2 JD 227	41
4.2.3 JD 229	42
ASASP-X D/D_0 Profiles for:	
4.3.1 Entire SEAVS Period Based on Integrated Aerosol Volumes	46
4.3.2 Entire SEAVS Period Based on Mass Mean Diameter Ratios	46
4.3.3 Pre-Hurricane Period Compared to Theoretical Curve	47
4.3.4 Transition-Polluted Period Compared to Theoretical Curve	47
4.3.5 Correlation of MMD and Volume Water Uptake Methods	48
CHAPTER 5	
5.1.1 ASASP-X Daily Aerosol Volume and IMPROVE Daily Mass Concentrations	54
5.1.2 Percent Mass Concentrations During SEAVS	54
5.1.3 Correlation of ASASP-X Volume and IMPROVE Mass Concentrations	56
5.1.4 Correlation of ASASP-X Volume and IMPROVE Mass Concentrations for Two SEAVS Time Periods.....	57
5.2.1 Correlation of Experimental and Estimated D/D_0 , Volume Method	62
5.2.2 Correlation of Experimental and Estimated D/D_0 , MMD Method	62

FIGURES IN APPENDICES

APPENDIX A	
A.1.1 [CN] Number Concentration During SEAVS	76
Selected Meteorological Data During SEAVS:	
A.2.1 Wind Direction	77
A.2.2 Relative Humidity	78
Selected Chemical Fine Mass Concentrations During SEAVS:	
A.3.1 Gravimetric Mass	82
A.3.2 Sum of Sulfate and Ammonium	82
A.3.3 Organic Carbon	82
A.3.4 Soil	82
A.3.5 Elemental Carbon	83
A.3.6 Sum of Nitrate and Nitrite	83
A.3.7 Chloride	83
A.3.8 Sulfate Acidity	83
Satellite Images of Hurricane Erin:	
A.4.1 August 3, 1995	85
A.4.2 August 4, 1995	85
APPENDIX B	
B.1.1 Schematic of ASASP-X Optics	88
Normalized PHA Voltages:	
B.2.1 - B.2.2 Range 3, Range 2	92
B.2.3 - B.2.4 Range 1, Range 0	93
B.3.1a-c 0.30 μm and 0.19 μm Post Calibration PSL Distributions	96
APPENDIX C	
C.1.1 Mie Scattering Functions for Two Refractive Indices Used in the ASASP-X Data Processing	100
C.3.1 Code Segment for Accumulation Mode Cutoff Parameter	108
APPENDIX D	
D.1.1 Dry Aerosol Refractive Index During SEAVS	114
D.1.2 Refractive Index as a Function of RH During the Pre-Hurricane Period	116
D.1.3 Refractive Index as a Function of RH During the Transition and Polluted Periods	116

1. INTRODUCTION

In the southeastern U.S., summertime air pollution and high humidity combine to produce some of the worst visibility conditions in the nation. However, the source of the region's air pollution, and the role this air pollution plays in visibility degradation, remain the focus of debate. Some point to the dense forest canopy that covers the rural landscape as the source of natural 'blue haze'. Others implicate anthropogenic emissions of sulfur dioxide from coal fired power plants as the main culprit in causing pollution that degrades visibility. Water associated with haze particles contributes significantly to visibility degradation in the southeastern U.S., although the apportionment of water to individual chemical components of the haze is not yet well understood. This work attempts to characterize the hygroscopic behavior of ambient airborne particles, and further to account for water uptake by individual chemical components of the aerosol fine mass. Results from this work indicate that sulfates can explain the majority, if not all, of the experimentally observed water uptake by ambient particles. If this thesis bears out, the conclusion can be drawn that organics play a minor, if not negligible, role in modifying water uptake by ambient particles in the southeastern U.S. Experimental data is also presented on ambient size distribution parameters for dry and humidified aerosol in the study area since these data are useful in visibility and radiative transfer models.

The field portion of this project was part of the Southeastern Aerosol and Visibility Study (SEAVS) during July and August of 1995 in Great Smoky Mountains National Park (GRSM), Tennessee. Experiments conducted during SEAVS sought to resolve some of the complex relationships between pollutant emissions, secondary aerosols, and air quality, particularly visibility, that affect GRSM and the southeast U.S. Specific goals of SEAVS are to characterize aerosol fine mass, chemistry and hygroscopicity to improve the reliability of computer models that simulate visibility and aerosol properties (Saxena and McMurry,

1995). This work addresses a subset of SEAVS objectives, namely the quantification of aerosol hygroscopicity by a relatively straightforward optical method.

To provide background information relevant to this particular project, Chapter Two introduces the visibility issue at GRSM and reviews other experimental methods currently being used to examine hygroscopic behavior of ambient particles. Particle light scattering and aerosol hygroscopicity are also discussed since these topics are fundamental to understanding the objectives and experimental results of this work. A discussion on the optical particle counter (OPC) used in this work is included as a preface to subsequent sections on OPC calibration and experimental uncertainty. The formulas used to calculate aerosol size distribution statistics in this work are also presented in Chapter Two.

Experimental sections in Chapter Three describe the special study conducted by the National Park Service (NPS) and Colorado State University (CSU) during SEAVS. The objectives of the special study are to quantify the relative humidity (RH) dependence of ambient aerosol size distributions and the ambient light scattering coefficient. The primary instruments used in the special study were a PMS ASASP-X OCP and a Radiance Research nephelometer. The inlet used during the field project allowed for RH control of aerosol sampled by the two primary instruments.

Results from this work are presented in Chapter Four. These results include size distribution statistics for dry ambient aerosol at GRSM, and estimates of water uptake by ambient aerosol in the humidified sampling environment. The size change of ambient particles are reported as wet-to-dry diameter ratios to quantify water uptake. These growth factors are derived from experimental data in two ways. One approach is to take the ratio of humidified to dry aerosol distribution mass mean diameters. The other approach uses only the integrated volume concentrations of humidified and dry aerosol distributions to derive particle size change as a function of RH. Water uptake data are presented as wet to dry

particle diameter ratios for the entire SEAVS period as well as for time periods defined by unique meteorology and aerosol chemistry. Experimentally derived particle size changes are then compared to estimates of water uptake for pure sulfate particles available in the literature and also theoretical size change for internal mixtures of sulfate and organic carbon. A discussion of uncertainty in derived RH dependent size change factors, as well as examples of the propagation of this uncertainty in a visibility model, lend insight into the practicality of this experimental method and its potential success in addressing some of the larger SEAVS goals.

Summaries of relevant meteorology, aerosol chemistry, and condensation nuclei concentration [CN] during SEAVS, are given in Appendix A. Appendix B includes the OPC calibration methods used in this work. The Mie theory inversion for converting raw data from the OPC to aerosol size distributions is given in Appendix C. Finally, Appendix D presents a discussion on the initial choices of refractive index used in the data inversion and whether they are appropriate for aerosol during SEAVS.

2. BACKGROUND

The impetus for SEAVS was the 1977 Amendments to the Clean Air Act (CAA) (165(d)(2)(c)(ii)). The CAA mandates the Prevention of Significant Deterioration in Class 1 Area federally managed lands, including National Parks. In a 1992 Preliminary Notice of adverse impact in GRSM, the Department of Interior moved to block any new permitting of major pollutant sources within 120 miles of the National Park. Only major pollutant sources that could demonstrate their emissions would not adversely impact air quality related values (e.g., visibility and acid deposition) at GRSM would be allowed to begin operation.

The adverse impact of air pollution on visibility in GRSM has been substantiated by air quality monitoring in GRSM and surrounding areas that predate SEAVS (Sisler *et al.*, 1993). Long term monitoring programs in the southeastern U.S. have implicated a sustained increase in anthropogenic sulfur emissions over the past 50 years in the degradation of air quality in GRSM. Spatial emissions trends indicate coal fired power plants are the primary source of fine sulfate mass observed in the southeastern U.S. (Malm *et al.*, 1994).

It is contingent in the current interpretation of the CAA by the Environmental Protection Agency that the impact of any new pollution source be demonstrated explicitly (Renfrow, 1995). However, due to the complex relationship between primary pollutants and formation of secondary particulate pollutants that have an adverse impact on air quality, quantifying the impact a specific source, or source reduction, will have is difficult. It is anticipated that SEAVS will augment the current knowledge in the scientific community, and the understanding held by policy makers, about relationships between pollutants and visibility in the rural southeastern US.

The primary chemical components in the aerosol fine mass in the southeastern U.S. are sulfate compounds, organic carbon, water and soil. Particulate sulfate exists predominantly as either fully neutralized ammonium sulfate, partially neutralized ammonium

bisulfate, or sulfuric acid. A trend towards more acidic sulfate particles exists as one goes from the northeastern to southeastern U.S. (Malm *et al.*, 1991). Data from the Interagency Monitoring of Protected Visual Environments (IMPROVE) samplers indicate the primary water soluble ionic species measured during SEAVS were ammonium sulfate complexes. During pollution episodes sulfate compounds had airborne particle concentrations that exceeded $20 \mu\text{g m}^{-3}$, with peak concentrations during SEAVS in excess of $40 \mu\text{g m}^{-3}$. Organic carbon was present in mass concentrations near those of sulfates during clean periods ($3\text{--}4 \mu\text{g m}^{-3}$). Soil mass generally had lower mass concentrations and displayed more temporal variability than either sulfates or organic carbon. (See Figure 5.1.2 and Figures A.3.1 to A.3.4).

Characterizing the composition and hygroscopic behavior of particulate organic carbon at GRSM is a focus of some research conducted during SEAVS. The source of organic carbon is typically either anthropogenic, via petroleum combustion, or biogenic, from plant volatile organic carbon (VOC) emissions, the latter predominant in the rural southeastern U.S. (Southern Oxidants Study, 1995). Data from urban field studies have shown that organic carbon can decrease water uptake by water soluble ionic species, while in more remote areas organics often enhance aerosol water uptake (Saxena *et al.*, 1995). Water uptake suppression can be explained by the observation that some water insoluble organic compounds form surfactant layers that impede water transfer to a particle's soluble core (Andrews and Larson, 1993). Alternatively, water soluble organics can associate with ambient water vapor and enhance mixed aerosol hygroscopicity. The water solubility of organics is hypothesized to increase with their atmospheric residence time as their structure and functionality are altered through oxidation processes (Mueller *et al.*, 1982).

Other experimentalists have sought to resolve some of the same hygroscopicity issues as those addressed in this work, although their methods were more elaborate and ostensibly yielded more detailed results. In the South Coast Air Quality Study (1987) and the Navajo Generation Station Visibility Study (1990) a tandem differential mobility analyzer (TDMA) measured RH dependent water uptake of size classified ambient particles (Zhang *et al.*, 1993). During SEAVS both the TDMA (McMurry, 1996) and a differential mobility optical particle size spectrometer (DMOPSS, Kreisburg *et al.*, 1996) were used to measure ambient particle hygroscopicity. Both the TDMA and DMOPSS systems were designed to resolve the water uptake of size classified particles within the ambient aerosol size distribution. If particles of one size class exhibit different degrees of water uptake, that is, if the particles separate into more and less hygroscopic fractions, then one can infer that the aerosol population is externally mixed in terms of individual particle chemistry (Zhang *et al.*, 1993). In contrast, the experimental method in this work measured water uptake for a particle size range and was not designed to differentiate between internal and external aerosol mixtures. In short, we report the ‘total’ water uptake by accumulation mode aerosol.

While the TDMA is capable of measuring total water uptake across the aerosol size spectrum, it is generally used to measure water uptake by discrete particle sizes. Size classified hygroscopicity data from the TDMA has been extended, for example, to total water content for humidified aerosol PM 1.8 (particles less than 1.8 μm in diameter) by inferring a size distribution function and integrating size classified water uptake across the aerosol size distribution (Saxena *et al.*, 1995). The DMOPSS system during SEAVS, on the other hand, measured both water uptake by size classified particles and total water uptake by ambient aerosol size distributions. Total water uptake measured by the DMOPSS for SEAVS aerosol

should be directly comparable to the water uptake results from this work, since the experiments differed only in the types of OPCs used to gather size distribution data.

It is descriptive when presenting hygroscopicity results to compare experimental data to theoretical estimates of water uptake. Saxena *et al.* (1995) used a chemical thermodynamic approach to estimate water uptake by ionic species at RH > 80%, and estimated ambient organic carbon hygroscopicity from residual aerosol water content determined by experiment. An alternative method to estimate ionic species water uptake is to take pure solute water activities from the literature (Tang *et al.*, 1981; Tang and Munkelwitz, 1994). In this work, empirical relationships for solute water activity, combined with a mixing rule (Malm and Kreidenweis, 1996), are used to estimate water uptake by atmospheric particles. This work assumes that ionic (ammonium and sulfate ions) and organic compounds are internally mixed and confined to the aerosol accumulation mode, whereas soil mass is restricted to a separate large aerosol mode.

2.1 Particle Light Scattering

Under typical summertime meteorological conditions, the primary contribution to visibility degradation in the southeastern U.S. is diffuse light scattering along the viewer's line of sight. Particles, which can exist as haze drops under humid conditions, are responsible for most of this light scattering. The light extinction coefficient, which is described primarily by particle light scattering in the southeastern U.S., can be thought of as having four components:

$$b_{\text{ext}} = b_{\text{sp}} + b_{\text{ap}} + b_{\text{sg}} + b_{\text{ag}} \quad 2.2.1$$

where b_{ext} (km^{-1}) is the sum of scattering and absorption by particles, b_{sp} and b_{ap} , and scattering and absorption by gas molecules, b_{sg} and b_{ag} , respectively. Within the constraints

of reasonably applicable assumptions, b_{ext} has an inverse relationship to visible range, a more tangible measure of visibility given by the Koschmeider equation (Seinfeld, 1986).

The light scattering coefficient can be calculated by integrating the single particle scattering efficiency, Q_s , over a particle size distribution function, with the following expression;

$$b_{\text{sp}} = \int_0^{\infty} \frac{\pi}{4} D_p^2 Q_s(n, D_p, \lambda) f(D_p) dD_p \quad 2.2.2$$

where D_p is the particle diameter, Q_s is given by Mie theory as a function of particle complex refractive index, n , D_p , and λ , the wavelength of light, and $f(D_p)$ is the aerosol size distribution function (Seinfeld, 1986).

Figure 2.1.1 shows the effect of RH and particle size on b_{sp} . In this figure, b_{sp} is calculated as a function of RH and dry mass median diameter for lognormal distributions of ammonium sulfate with equivalent dry mass concentration ($1 \mu\text{g m}^{-3}$). The light scattering coefficient represents solutions to Equation 2.2.2. A relevant feature of Figure 2.1.1 is the increase in light scattering as RH increases, particularly at humidities over 80%. Note the maximum in the mass scattering efficiency for aerosols near $0.3 \mu\text{m}$. For particle sizes below $0.1 \mu\text{m}$ light scattering is inefficient and b_{sp} drops sharply.

During the summer in the southeastern U.S. high humidity is common. Also, results from this work and others researchers during SEAVS (Kreisburg *et al.*, 1996) indicate that ambient particle size distributions with accumulation mode mass mean diameters near $0.3 \mu\text{m}$, with geometric standard deviation near 1.6, are common. The combination of available ambient water vapor and an aerosol size distribution that scatters light efficiently create ideal conditions for visibility degradation at GRSM.

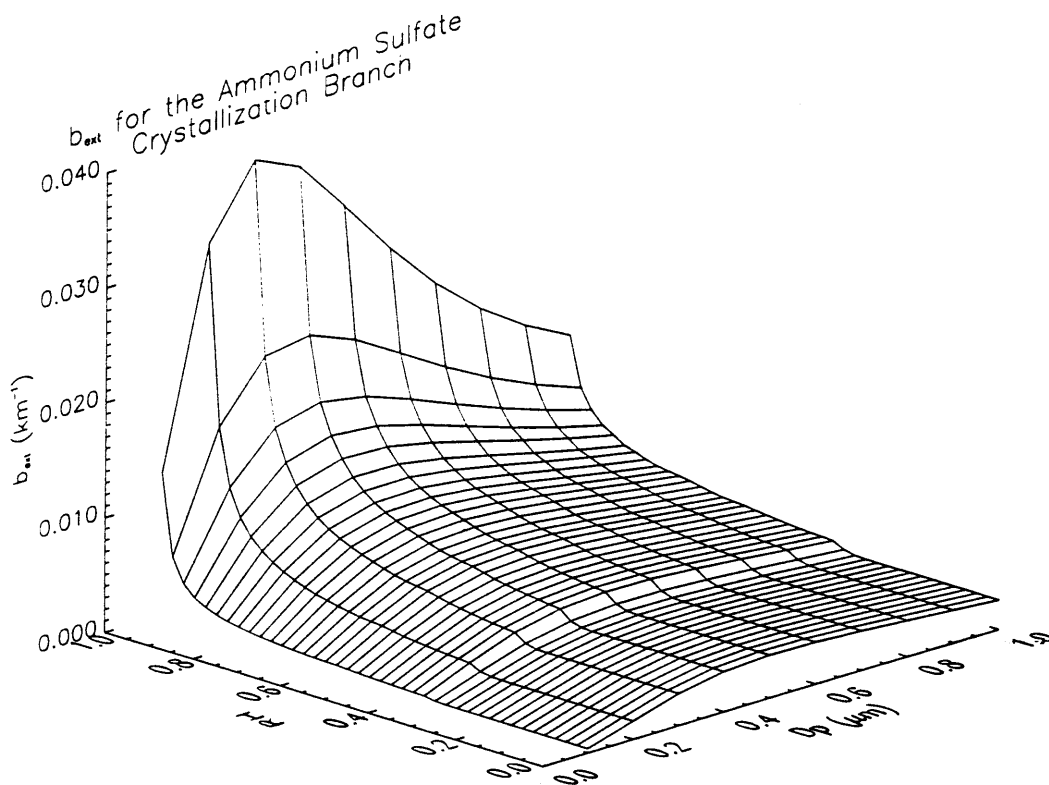


Figure 2.1.1. Output from the Tsay and Stephens (1992) Physical/Optical Model for Atmospheric Aerosols. The graph represents the crystallization branch of condensed ammonium sulfate aerosol, distributed lognormally with a geometric standard deviation of 1.6 and airborne concentration of $1 \mu\text{g m}^{-3}$.

It should be pointed out that in Figure 2.2.1 the MMD shown is for dry aerosol, and as RH increases, particles take up water and increase in size. In fact, it is the particle growth that is responsible for the increase in light scattering at high RH (the added water can equal or exceed the initial aerosol volume), since the light scattering coefficient is proportional to the integrated surface area of an aerosol distribution for geometrically similar particles (Hinds, 1982). Thus, b_{sp} , as presented in the model simulation shown in Figure 2.1.1, is related to the RH dependent growth parameters within the visibility model itself. The particle size change parameters used in Figure 2.1.1 are taken from experimental

determinations of pure ammonium sulfate size change as a function of RH from Tang and Munkelwitz (1994).

2.2 Aerosol Hygroscopicity

The water uptake, or hygroscopicity, of solute aerosol can be expressed as D/D_0 , the ratio of wet to dry particle diameter. This work considers water associated with haze particles, that is, particles that form aqueous solutions below saturation RH.

Particle growth in a humid environment can be predicted from theory by calculating the solute particle water activity as a function of ambient RH. Chemical thermodynamics predicts that a particle will deliquesce, or change from a dry crystalline state to a saturated solution drop, when the ambient RH equals a specific water activity in the solute particle. At humidities greater than the deliquescence RH and below water vapor saturation, the water associated with a solute drop maintains an equilibrium with ambient water vapor. Equations 2.2.1 and 2.2.2 are expressions for the relationship between RH, solute water activity, and the amount of condensed water associated with a solute particle.

$$RH = A_w \exp\left(\frac{4\phi M}{\rho RTD}\right) \quad 2.2.1$$

$$A_w = x_w \gamma_w \quad 2.2.2$$

In Equation 2.2.1, M is the molecular weight of water, ϕ is the surface tension of water above the particle, ρ is the condensed phase density, R the gas constant, T is temperature, and D is the diameter of the condensed particle (Tang *et al.*, 1981). The exponential term is an enhancement in water vapor pressure over the condensed particle which arises due to spherical curvature. Curvature effects for particles larger than $0.1 \mu\text{m}$ are assumed insignificant (Shettle and Fenn, 1979) and the exponential in Equation 2.2.1 can be

neglected. Equation 2.2.2 defines the particle water activity as the product of water mole fraction, χ_w , and the water activity coefficient, γ_w .

The amount of water associated with a haze drop can be predicted by chemical thermodynamics above the relative humidity of deliquescence (RHD). However, at humidities below the RHD, experiments have shown that solute particles often exist in a meta-stable equilibrium with ambient water vapor (Tang *et al.*, 1981; Tang and Munkelwitz, 1994). Due to the water hysteresis exhibited by some solutes, crystallization does not occur until a specific RH, often much lower than the RHD, is achieved (Tang *et al.*, 1981). Figure 2.2.1 shows the size change for an ammonium sulfate particle as a function of RH. A separate deliquescence branch, for increasing the aerosol equilibrium RH starting from below the RHD, and crystallization branch, for decreasing equilibrium RH from above the RHD, are shown.

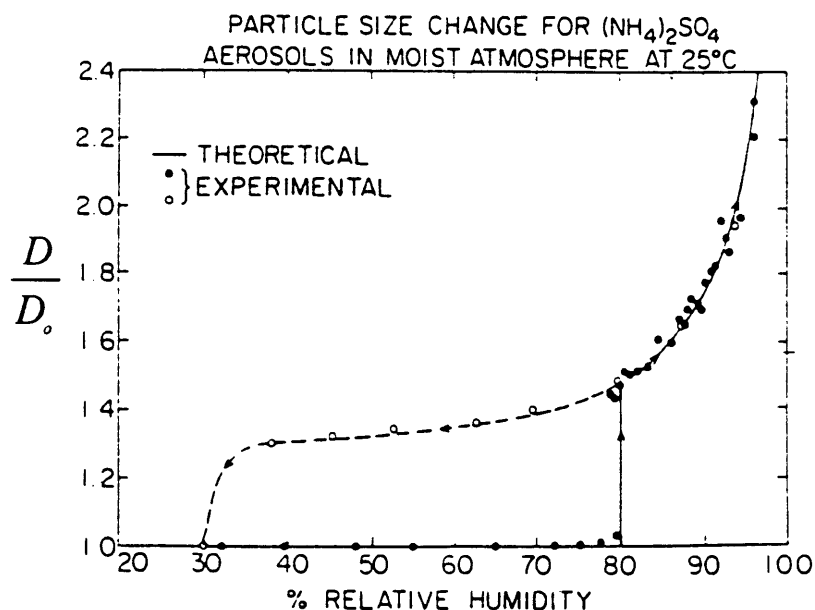


Figure 2.2.1. $\frac{D}{D_0}$ vs. RH for (NH₄)₂SO₄ (Tang *et al.*, 1981).

Experimental data that predict the mass and density of condensed phase as a function of A_w for pure solutes at 25° C are available in the literature (Tang and Munkelwitz, 1994). From experimental data, curves similar to Figure 2.2.1 can be reconstructed for the solute species of interest. D/D_o can be expressed in terms of $\chi(A_w)$, the weight percent of solute in a condensed particle, $\rho(A_w)$, the density of the condensed phase, and ρ_o , the density of the dry particle, as follows:

$$D/D_o = \left(\frac{100 \rho_o}{\chi \rho} \right)^{1/3} \quad 2.2.3$$

Equation 2.2.3 assumes that the particles are spherical, that all added water is absorbed into the solute matrix, and that volume is conserved on mixing. An advantage of using known water activity expressions is that they are applicable to the broader humidity range of the crystallization branch of particle size change. A disadvantage is that they are not readily extended to a variety of mixed solutes where water activity data is not available.

It is practical to estimate D/D_o for simple aerosol mixtures of constituents that exhibit different size change as a function of RH. In this work theoretical water uptake is estimated for the fraction of ionic species (ammonium and sulfate ions) present in the aerosol accumulation mode. The water uptake estimates assume the aerosol can be represented by a homogenous internal mixture of ionic species and organic carbon. Since it is desirable to estimate water uptake for accumulation mode aerosol (D_p approximately less than 1 μm), and currently available chemical data represent fine mass ($D_p < 2.5 \mu\text{m}$), only ionic, organic carbon and elemental carbon mass fractions are used to represent the mixed accumulation mode aerosol. Soil mass is excluded to large mode aerosol and therefore not included in theoretical estimates of water uptake. Water uptake estimates are calculated using the mixing rule for an ideal binary mixture from Malm and Kreidenweis (1996);

$$D/D_o = \left[\frac{\rho_{dry}}{\rho_{wet}} \left[z_1 \frac{\rho_{wet1}}{\rho_{dry1}} \left(\frac{D}{D_{o,1}} \right)^3 + z_2 \frac{\rho_{wet2}}{\rho_{dry2}} \left(\frac{D}{D_{o,2}} \right)^3 \right] \right]^{\frac{1}{3}} \quad 2.2.4$$

where ρ_{dry} and ρ_{wet} are the wet and dry mixed aerosol densities. Similarly, mass fraction, z , and wet and dry aerosol diameters are given by, D and D_o , respectively, where the subscripts 1 or 2 denote the respective pure phase. In Chapter 5 water uptake estimated by Equation 2.2.4 is compared to experimentally derived water uptake derived from OPC data from this work.

2.3 Optical Particle Counter

The optical counter used in this work measures aerosol size and number concentration by detecting scattered light from individual particles. The OPC operates on the premise that light scattered from a particle and collected by the instrument's optical system is a function of the particle's size. The OPC is designed to count individual particles as they traverse the instrument's optics. A discussion of the OPC used in this work, as well as potential corrections to the instrument's measurements in an experimental setting, follows.

The ASASP-X measures the intensity of scattered light from individual particles as they pass through the instrument's laser beam. A 632.8 nm He-Ne laser is the light source. A photodetector measures light intensity collected by a parabolic mirror over a 35° to 120° solid angle incident to the laser beam. Light collected in this geometry is assumed to be scattered from individual particles in the OPC sampling volume. A separate photodetector measures the intensity of the incident laser beam in order to calculate the relative intensity of light scattered from individual particles. A schematic of the ASASP-X optics is shown in Appendix B.1.

Individual particle scattering intensity is converted to an electrical current pulse by the photodetector. The current is then amplified by the programmable gain amplifier which has four settings on the ASASP-X. At each gain setting the amplified signal is fed into a 16 channel pulse height analyzer (PHA). The PHA separates particle pulse height (or voltage) into channels based on a comparison of actual pulse voltage to pre-set voltage thresholds in 15 comparators within the PHA. The comparator voltages are unique for each amplification range, giving the ASASP-X effectively 60 channels for all four amplification ranges. Immediately following a particle count, an electronic dead time is imposed to ensure that measured voltage pulse resulted from light scattered by an individual particle.

The ASASP-X uses particle free sheath air in the inlet flow system to hydrodynamically ‘focus’ the sample flow to a narrow stream, approximately 200 μm in diameter. The particle trajectories must pass through the center of the laser beam so that their scattering intensity, relative to the maximum beam intensity, is proportional to particle size in a reproducible manner. If the particle trajectory passes through the outer limits of the laser beam, a decrease in relative scattering intensity will cause the particle to be undersized by the OPC electronics. Monodisperse particles measured by the OPC when the sample stream is either out of ‘focus’ or not aligned through the center of the laser beam will appear as a broad distribution, with a tail towards smaller sized particles.

The OPC cannot differentiate between scattering intensity from a single particle and the coincident detection of multiple particles. Also, the OPC does not detect particles during sampling dead time. A correction to the measured concentration, which accounts for these two loss mechanisms, and is based on the probability of finding a particle close to a neighboring particle in the sample flow, is presented by Baumgardner (1995):

$$N_m = \frac{N_o (T - \tau) e^{-\lambda \tau}}{T} \quad 2.3.1$$

$$\tau = N_m Q \tau_d \quad 2.3.2$$

In Equation 2.3.1, N_a is the actual aerosol concentration, N_m is the concentration measured over a sampling time interval T , τ_t is the average particle transit time through the laser beam and λ is the wavelength of laser light. τ is the total dead time (Equation 2.3.2), where Q is sample flow rate and τ_d is the electronic dead time.

For measured particle concentrations less than 2000 cm⁻³ corrections given by 2.3.1 are small (Baumgardner, 1995). Since the ASASP-X sampling time period, given by T in Equation 2.3.2, includes only time spent in a given amplification range, the correction applies to the total concentration in that range. The maximum particle concentration in any given range for this work rarely exceeded 1000 cm⁻³ and losses due to coincidence are negligible.

2.4 Aerosol Size Distribution Statistics

Formulas for computing geometric mean size and geometric standard deviation for the aerosol distribution are taken from Knutson and Liou (1982). In the following equations, $D_{p,g}$ is the geometric mean of the aerosol distribution and σ_g is the geometric standard deviation.

$$D_{p,g} = \text{anti log} \left(\frac{\sum a_i \log \frac{x_i}{\sum N_i}}{\sum N_i} \right) \quad 2.4.1$$

$$\sigma_g = \text{anti log} \left(\frac{\sum N_i \log^2 (x_i / D_{p,g})}{\sum N_i} \right)^{\frac{1}{2}} \quad 2.4.2$$

$$x_i = (x_n x_{n+1})^{\frac{1}{2}} \quad 2.4.3$$

N_i is the number of counts in bin (i) and x_i the geometric mean diameter of bin (i). x_n is the lower particle diameter for the bin limit (n). These equations are independent of the shape of the distribution and can be applied to any distribution moment, such as number or volume.

In most cases the particle size range detected by the ASASP-X only partially resolves the entire number distribution, whereas the volume distribution, for the same aerosol, is well defined over the ASASP-X detection range. Transformation from a discrete number distribution to a discrete volume distribution is given by:

$$V_i = \frac{\pi N_i}{6} x_i^3 \quad 2.4.4$$

where V_i ($\mu\text{m}^3 \text{ cm}^{-3}$) is the aerosol volume in bin (i). Aerosol volume distribution parameters obtained from the statistical equations given above are used to represent experimental data from this work. The geometric mean diameter of the volume distribution, or geometric mass mean diameter (MMD) assuming the particles are characterized by a single density, is referred to throughout this work.

Number mean diameters can be inferred from the volume distribution statistics by assuming the particles are distributed lognormally. The transformation to number geometric mean size from volume parameters, assuming a lognormal aerosol distribution, is given by Seinfeld (1986) as:

$$D_{p,g,no.} = D_{p,g.vol} \exp\left(-1.5 \ln^2 \sigma_g\right) \quad 2.4.5$$

While Equation 2.4.5 represents a technique to derive aerosol number $D_{p,g}$ from size distributions measured in this work, it is not used in the analyses presented herein, as no assumptions about the size distribution functions that apply to ambient aerosol distributions are made in this thesis.

3. NPS/CSU SPECIAL STUDY

3.1 Objectives

The NPS/CSU special study was defined by three experiments. 1.) Collection of a comprehensive local meteorology data set, 2.) determination of RH dependent ambient light scattering using nephelometer measurements, and 3.) determination of RH dependent ambient aerosol size distribution parameters, (Total number concentration, total volume concentration, $D_{p,g}$, σ_g), from OPC measurements.

This report focuses on results from experiment (3) although summaries of experiments (1) and (2) are included since these data are relevant to interpretation of the ASASP-X experimental results. Specific objectives for the OPC experiment include estimation of water uptake in the optically significant aerosol size range and quantifying aerosol size distribution parameters for the southeastern U.S. A discussion of aerosol loading and size distribution parameters taking into account prevailing meteorology is included.

3.2 Local and Synoptic Meteorology During SEAVS

Sherman *et. al* (1996) have defined at least seven unique meteorological periods during SEAVS. These periods are summarized below in Table 3.2.1.

SEAVS Meteorological Period	Dates	Dates (JD)
Beginning of Study	7/14/95 - 7/23/95	195 - 203
Dust	7/24/95 - 7/26/95	204 - 207
Pre-Hurricane	7/27/95 - 8/1/95	208 - 213
Hurricane	8/2/95 - 8/5/95	214 - 217
Post-Hurricane	8/6/95 - 8/8/95	218 - 220
Transition	8/9/95 - 8/13/95	221 - 225
Polluted	8/14/95 - 8/18/95	226 - 230
Post-polluted	8/19/95 - 8/25/95	231 - 237

Table 3.2.1. Meteorological periods during SEAVS.

Unusually high hurricane activity along the southeastern seaboard and U.S. Gulf Coast was a prominent synoptic meteorological feature during the summer of 1995. On occasion, large scale tropical storm flow moved inland and influenced both the meteorology and air quality in the southeastern U.S. The most notable synoptic event during SEAVS was Hurricane Erin, which made landfall at Pensacola, Florida on August 3, 1995 (Figure A.4.1). When Erin dissipated over the southeastern states (Figure A.4.2) it carried with it an intrusion of clean maritime air to GRSM, providing exceptionally good visibility. The hurricane period is characterized by southeasterly flow and low particle concentrations. The chemical fingerprint of this maritime airmass is evident in the chloride fine mass record during SEAVS which peaks on JD 215 (Figure A.3.7).

Stagnation episodes, characterized by low wind speeds and slow moving high pressure systems, are common in the GRSM region during summer months (Southern Oxidants Study, 1995). The geography of the field site, at an elevation of 800 meters, overlooking the Tennessee Valley and Cumberland Plateau, created unique local air flow patterns. During stagnation episodes, daytime inversions often preceded afternoon upslope

flow that brought an air mass from the Tennessee Valley to GRSM. This low-level flow probably originated in industrialized regions that are abundant in secondary pollutant precursors. When stagnation episodes persisted during SEAVS, particle concentrations increased progressively, resulting in high aerosol mass loading and severely degraded visibility.

During SEAVS, the pre-hurricane period and the transition-polluted period represent two stagnation episodes of different magnitude. The pre-hurricane period was a relatively short stagnation episode, during which particle mass accumulated to $25 \mu\text{g m}^{-3}$ and visibility was good (b_{sp} of 0.05 to 0.2 km^{-1}). Synoptic flow from Hurricane Erin then brought clean air into the area and visibility conditions were exceptional ($b_{\text{sp}} < 0.05 \text{ km}^{-1}$). The next stagnation episode occurred during the transition and polluted periods which saw an essentially undisturbed particle buildup that culminated in aerosol high mass loading (60 to $80 \mu\text{g m}^{-3}$) and severe visibility impairment (b_{sp} as high as 0.9 km^{-1}). Often during SEAVS, stagnation episodes ended with brief periods of thunderstorm activity that would 'wash out' airborne particulate mass.

What is interesting about the two stagnation episodes discussed above is their differences in aerosol chemistry. During the pre-hurricane period sulfates and organic carbon were present at average mass fractions of 62 and 38%, respectively, relative to each other. During the transition and polluted periods the sulfate and organic carbon relative mass fraction were 81 to 19%, respectively. These chemical fractions, taken from IMPROVE data, have implications for aerosol properties, particularly hygroscopicity, during each period.

3.3 RH Controlled Experimental Design

3.3.1 Aerosol Inlet

The CSU/NPS study used an inlet that allowed RH control of ambient aerosol. The inlet consisted of a bank of 23 Permapure driers that lead to a sampling plenum. The inlet could sample at flow rates to 23 liters per minute without compromising drier efficiency, based on evaluations of single units (Dick *et al.*, 1995). RH was set by mixing filtered air from saturated and dry air sources in the Permapure sheath flow to achieve the desired RH in the plenum. RH could typically be adjusted from 5 to 90%. A Campbell temperature and dew point sensor was fit inside the plenum to record temperature and RH. Sample residence time in the RH conditioned plenum was approximately 30 seconds, and approximately 0.8 second inside the Permapure driers, based on a typical flow rate of 22 liters per minute.

The inlet for the ASASP-X tapped into the RH conditioned inlet at the plenum. The ASASP-X inlet was 1 meter in total length and made of $\frac{3}{4}$ inch outer diameter stainless steel tubing. Two Swagelock three way valves allowed for inline sample flowrate checks. Based on typical ASASP-X inlet flow rates of $60 \text{ cm}^3 \text{ min}^{-1}$, the sample residence time in this inlet was approximately 16 seconds. The residence time in the plenum and ASASP-X inlet provided sufficient time for the sampled aerosol to equilibrate with the conditioned RH. The only disadvantage of the sample residence time in the ASASP-X inlet was potential loss of particles due to gravitational settling. Losses due to particle diffusion to the tubing walls are assumed insignificant for particle sizes greater than $0.1 \text{ }\mu\text{m}$ (Willeke and Baron, 1995) and are ignored here.

Depositional losses in the ASASP-X sample inlet due to gravitational settling can be calculated based on sample flow and inlet geometry. In calculations for gravitational loss

due to particle settling vertical sections of tubing can be ignored, provided sample flow is oriented downward. This was the case for the Permapure driers in the RH conditioned inlet, and therefore gravitational losses are ignored in the driers and in the plenum. The classic solution by Fuchs, (1964) for sampling efficiency in circular tubing with laminar flow is given in Equation 3.3.1.1 following the development in Willeke and Baron, (1993):

$$\eta = 1 - \frac{2}{\pi} \left[2\kappa \sqrt{1 - \kappa^{2/3}} - \kappa^{1/3} \sqrt{1 - \kappa^{2/3}} + \arcsin(\kappa^{1/3}) \right] \quad 3.3.1.1$$

where η is the fractional penetration of a given size particle population through the tubing, or the inlet efficiency. In Equation 3.3.1.1 κ is given by:

$$\kappa = \frac{3LV_{ts}}{4dU} \cos(\theta) \quad 3.3.1.2$$

In Equation 3.3.1.2, L is the length of tubing (cm), d is the tubing inner diameter (cm), V_{ts} (cm s⁻¹) is the particle terminal settling velocity, U (cm s⁻¹) is the average sampling velocity in the tubing, and θ is the inclination of the tubing from horizontal in degrees. Equation 3.3.1.2 reduces to 0 for $\theta = 90^\circ$. The particle terminal settling velocity is given by:

$$V_{ts} = \tau g \quad 3.3.1.3$$

where τ is the particle relaxation time (s) and g is gravitational acceleration (cm s⁻²). τ is given by:

$$\tau = \frac{\rho_p D_p^2 C_c}{18n} \quad 3.3.1.4$$

where ρ_p is the particle density, D_p is the particle diameter, C_c is the Cunningham slip correction, and n is the gas viscosity constant of air ($n = 1.827 \times 10^{-4} \frac{\text{dyne cm}}{\text{s}}$) at 25^o C.

The slip correction in Equation 3.3.1.4 is given by:

$$C_c = 1 + Kn \left[\alpha + \beta \exp\left(-\gamma / Kn\right) \right] \quad 3.3.1.5$$

where Kn is the particle Knudsen number and is given by:

$$Kn = \frac{2\lambda}{D_p} \quad 3.3.1.6$$

In Equation 3.3.1.6, λ is the gas molecular mean free path, and the value used is for a pressure of 1 atmosphere and temperature of 25° C ($\lambda = 6.65 \times 10^{-10}$ cm). The constants in Equation 3.3.1.5 are chosen to represent a solid particle in the slip correction term and have the values of $\alpha = 1.142$, $\beta = 0.558$, and $\gamma = 0.999$. In this experiment, particles sampled at high humidities may not be entirely solid, however by assuming solid particles in the inlet efficiency corrections an upper limit in particle loss based on density variations is estimated.

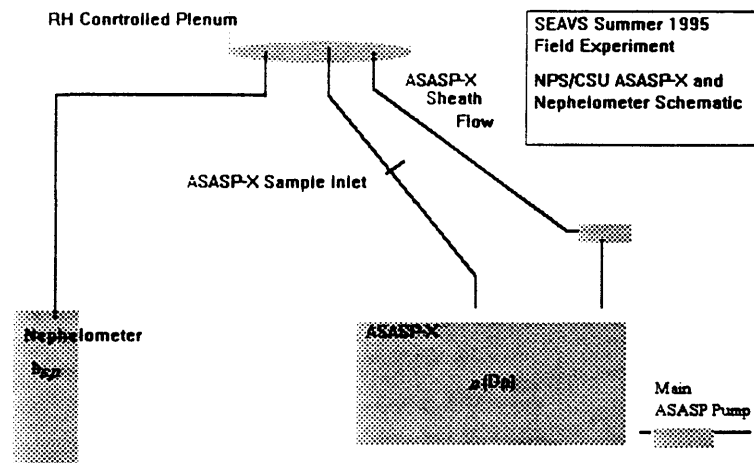


Figure 3.3.1.1. Configuration of the ASASP-X sample inlet during SEAVS.

The schematic in Figure 3.3.1.1 shows the geometry of the ASASP-X inlet. The inlet is oriented at 45° from the vertical for the first 40 cm of length following a 45° bend

from a vertical attachment to the plenum attachment. Another 45° bend leads to a vertical section followed by a wide 90° bend to a 10 cm horizontal section. This final horizontal section was attached to the ASASP-X itself with a 2.5 cm length of flexible conductive tubing. Thus, the ASASP-X inlet efficiency is calculated for two tubing sections, one of 40 cm at 45° to horizontal and another 10 cm horizontal section. The total inlet efficiency is given by:

$$\eta_{tot} = \eta_1 \eta_2 \quad 3.3.1.7$$

Aerosol concentration, N , representative of the actual ambient particle concentration in a given bin is related to the measured concentration in that bin by:

$$N_{actual} = N_{measured} / \eta_{tot} \quad 3.3.1.8$$

The ASASP-X sample inlet efficiency as a function of particle size is shown in Figure 3.3.1.2. Inlet loss corrections are applied to particle counts in each ASASP-X bin assuming the geometric midpoint diameter represents the particle size in that bin. Losses from particle impaction in tubing bends are ignored due to the very low particle Stokes numbers in the ASASP-X inlet for sampling conditions in this experiment.

Characterization of inlet efficiency in the field was not performed in any systematic manner. On JD 199 - 200 the ASASP-X was operated with an ambient inlet that bypassed the RH conditioned inlet, however the bypass made use of most of the OPC inlet for which the above efficiency calculations apply. OPC data from these days may be used as an indication of sampling efficiency in the RH conditioning portion of the inlet, provided fluctuations in ambient aerosol number concentrations were minimal for times that bracket use of the ambient RH inlet. Since the ambient particle number concentration was not constant over any two or three day period during SEAVS, no experimental determinations of sampling efficiency in the RH conditioned inlet were made.

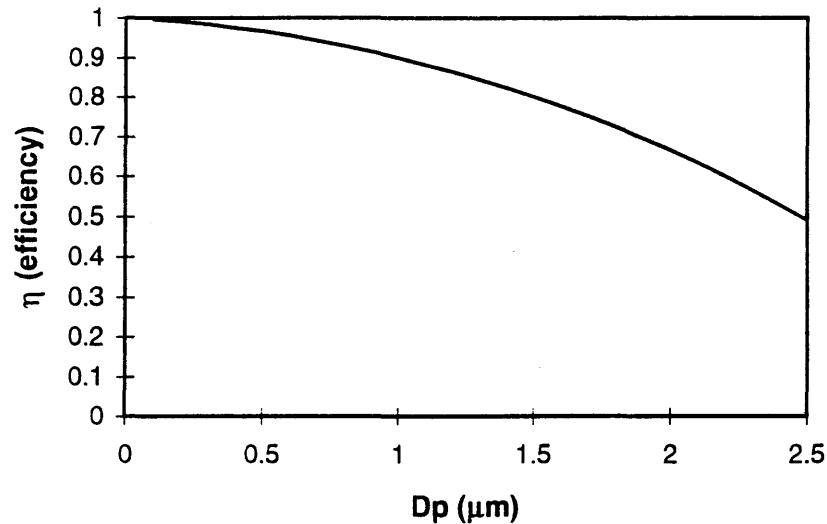


Figure 3.3.1.2. Theoretical efficiency for the ASASP-X sample inlet as a function of particle diameter. Only particle losses due to gravitational settling are considered.

3.3.2 PMS ASASP-X

Specific modifications to the ASASP-X (Serial No. 805-0978-10) air flow configuration for the SEAVS field experiment are explained in this section. The ASASP-X optics and electronics were described in Section 2.3.

For this field experiment, the ASASP-X was reconfigured to draw both its sample and sheath flows from the RH conditioned inlet plenum. The flow configuration for the ASASP-X during SEAVS is shown in Figure 3.3.1.1. Since the particle free sheath air that focuses the sample stream in the optical cavity exceeds the sample flow by volume ratios of approximately 20:1 it was important that the sheath air have the same temperature and RH as

the sample flow to ensure the water content of the RH conditioned aerosol was not altered upon sampling by the OPC. The flow system in this experiment differs from the manufactures' design in that filtered sample air was used as sheath flow rather than recirculating sheath air. Air temperature and RH for the ASASP-X were recorded immediately downstream of the laser cavity by a Campbell temperature and dew point sensor.

A comparison of plenum and ASASP-X temperature and RH is shown in Figure 3.4.1. Occasionally the temperature in the ASASP-X was slightly higher than in the plenum following prolonged operation of the OPC. This temperature differential caused the ASASP-X to operate at slightly lower humidities than those achieved in the plenum. Heating of the OPC air flow likely resulted from heat generated by the instrument's electronics. It is unlikely that heating from the laser itself affected characteristics of individual particles.

The ASASP-X sample flow rate was measured before and after acquiring data for a given aerosol distribution. At least three individual readings were taken for each flow measurement prior to and subsequent to sampling. Sample inlet flow rate for the ASASP-X was measured directly and in line using a Gilibrator primary calibration flow meter fitted with a 250 cm³ cell. Typical variance in the inlet flow rate was less than 5% of the total inlet flow. The ASASP-X sample flow rate was typically 60 cm³ min⁻¹. Sample flow rate was set by differencing the total flow and sheath flow. A total flow rate of 1200 cm³ min⁻¹ and sheath flow rate of 1140 cm³ min⁻¹ were common although the sample flow rate was the only routinely measured quantity.

3.3.3 Associated Instrumentation

A Radiance Research nephelometer tapped into the RH controlled inlet to measure the aerosol light scattering coefficient, b_{sp} . Ambient aerosol concentration [CN] was measured with a Condensation Nuclei Counter (TSI-3010 CNC) that was not connected to the RH controlled inlet. Aerosol number concentrations for $D_p > 0.01 \mu\text{m}$, (the 50% efficiency diameter for the 3010) were recorded during SEAVS (Appendix A.1.2).

3.4 Sampling Protocol

The RH controlled inlet conditioned aerosol from ambient RH to a given experimental RH. Thus, if the experimental RH was greater than ambient the aerosol were humidified, and if the experimental RH was less than ambient the aerosol were dried. The experimentally conditioned RH was cycled between low and high RH. The experimental RH and temperature are important to the interpretation of results from this experiment and were measured at different points in the inlet and instrumentation. Figure 3.4.1 shows plenum and ASASP-X temperature and RH for JD 207 and illustrates the manner in which the sample RH was controlled during the experiment. Aerosol distributions were collected by the OPC while RH was stable. A collection time of at least 15 minutes was allowed for the ASASP-X to gather statistically significant data (Section 4.4). Data collected while the RH ramped was not used to construct aerosol distributions. Sequential scans of dry and humidified aerosol size distributions were ultimately adopted as a sampling protocol in the field.

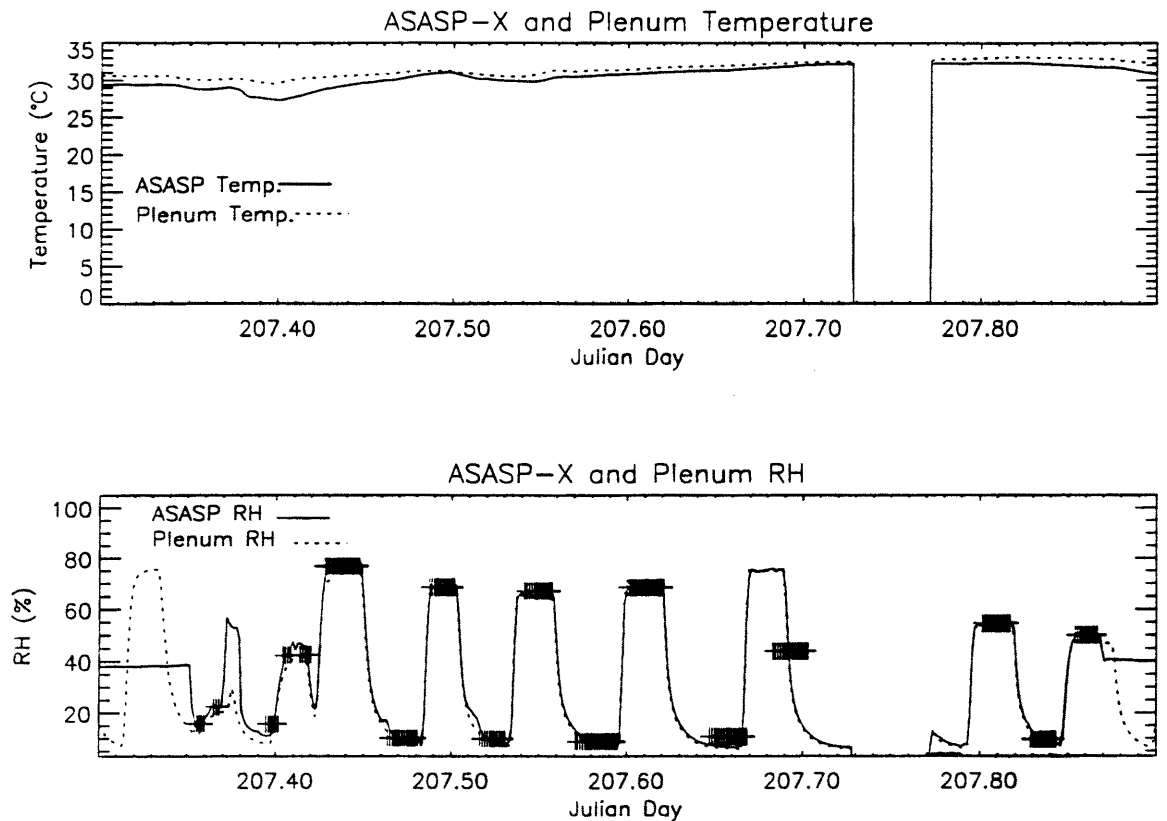


Figure 3.4.1. RH and temperature in the ASASP-X and RH controlled sample plenum. Hash marks indicate times when the OPC was collecting size distribution data. The RH in the OPC tracked closely with the plenum RH, the latter an indication of the nephelometer RH. Missing data indicates the data logging system was turned off. Initial ASASP-X scans, indicated by their relatively short time intervals, were PSL instrument performance checks (Appendix B.1).

4. RESULTS

This section focuses on experimental results from the ASASP-X data set.

Timelines are shown for the entire study, in the form of daily averages, for aerosol number and volume concentration size distribution parameters. Water uptake results for ambient aerosol in GRSM are also presented. Examples of sequential dry and humidified aerosol size distributions are included to demonstrate the increase in aerosol volume following humidification. The majority of water uptake results are presented as wet to dry particle diameter ratios, or D/D_o (Section 4.3).

The interpretation of raw OPC data can be an arduous process. Data inversion techniques, explained in Appendix C, have been applied to the raw data prior to its presentation in this chapter. Dry aerosol distributions were processed using refractive indices based on ambient aerosol chemical composition (Appendix D). Water uptake determinations used RH dependent refractive indices explained in Appendix C.

4.1 ASASP-X Dry Aerosol Characterization During SEAVS

A time line of daily averaged dry (RH < 15%) aerosol number concentration (cm^{-3}), obtained by integrating aerosol number concentration over the $0.1 < D_p < 2.5 \mu\text{m}$ size range, is presented in Figure 4.1.1. The SEAVS meteorological periods are superimposed on this figure to illustrate that these periods bracket trends of build up and depletion in the ambient aerosol number concentration.

Daily averages for the volume distribution parameters, volume concentration ($\mu\text{g cm}^{-3}$), MMD (μm) and σ_g , are shown in Figures 4.1.2 to 4.1.4, respectively. These parameters of the aerosol volume distribution represent accumulation mode aerosol,

typically in the $0.1 < D_p < 0.9 \mu\text{m}$ size range, although the upper diameter limit was adjusted with a floating cutoff parameter (Appendix C.3).

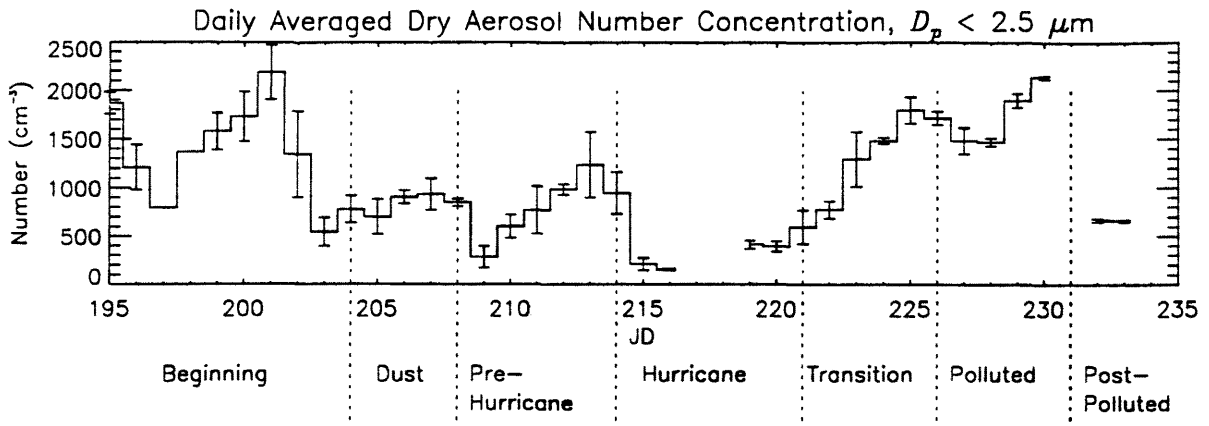


Figure 4.1.1. Total number concentration from the ASASP-X for aerosols in the size range $0.1 < D_p < 2.5 \mu\text{m}$. Vertical dashed lines demarcate SEAVS meteorological periods.

As pointed out earlier, the dry aerosol time lines display trends that correspond to SEAVS meteorological periods, described in Section 3.2. For example, during the pre-hurricane period aerosol number and volume accumulated until the onset of synoptic flow from Hurricane Erin on JD 215. Throughout the hurricane period, particle number and volume concentrations were low. Following the hurricane period, aerosol accumulation was essentially undisturbed during the two weeks of the transition and polluted periods. During this time the distribution MMD increased from 0.28 to $0.38 \mu\text{m}$ (Figure 4.1.3). Physical mechanisms that explain this size change are coagulation of small particles ($D_p < 0.1 \mu\text{m}$) with larger accumulation mode particles and/or condensational growth on the surface of accumulation mode particles (Seinfeld, 1986; Willeke and Baron, 1993). Figure 4.1.4 shows

that the shape of the aerosol distribution, described by σ_g , was stable during the pollution period (JD 226-230), while aerosol mean size and volume concentration increased. An increase in aerosol mean diameter will increase the mass (or volume) light scattering efficiency of ambient aerosols if the resulting distribution grows into a size regime where light scattering is more efficient relative to smaller mean diameters.

Daily Averaged Dry Aerosol
Figure 4.1.2. Accumulation Mode Volume Concentration

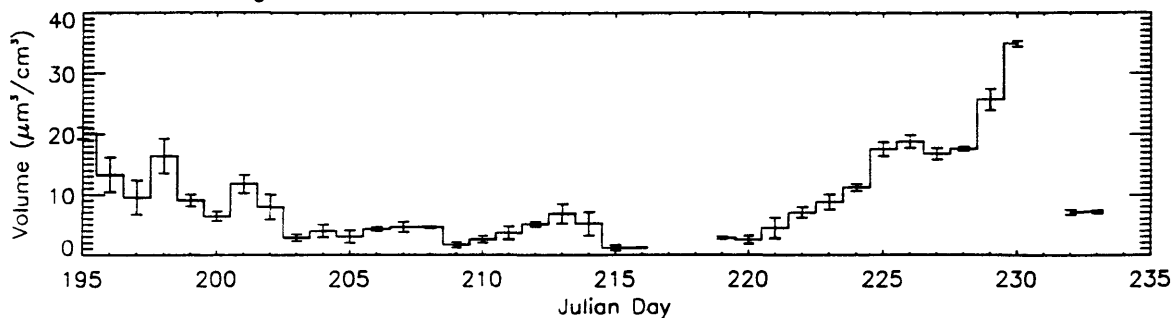


Figure 4.1.3. Accumulation Mode MMD

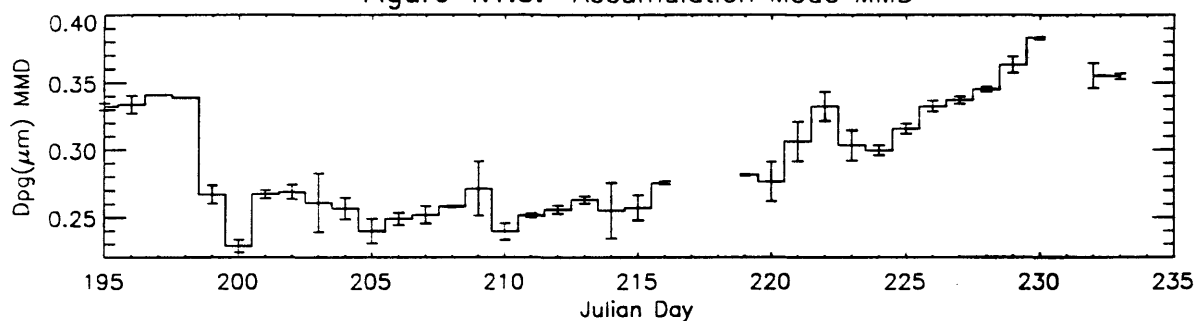
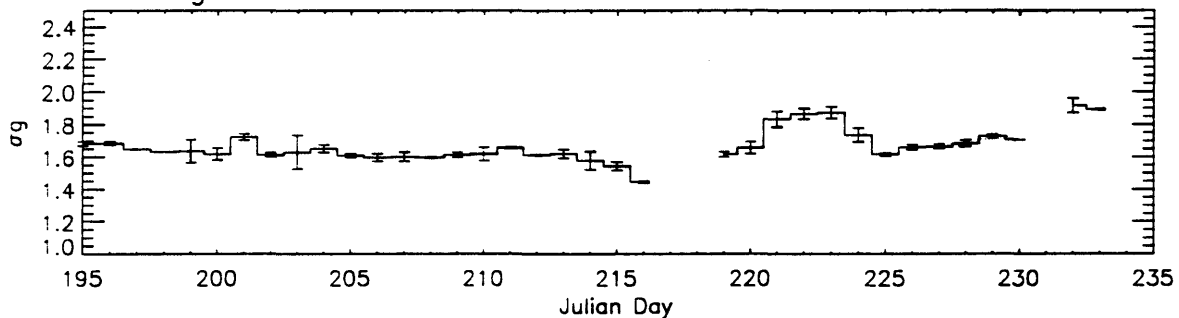


Figure 4.1.4. Accumulation Mode Geometric Standard Deviation



Figures 4.1.2 to 4.1.4. Dry aerosol volume distribution statistics measured by the ASASP-X for accumulation mode aerosol. Size distribution data was processed with a refractive index of 1.520 for JD 195 to 221 and 1.501 for JD 221 to 223.

Dry aerosol size distribution parameters from this study are given in Table 4.1.1. The figures shown previously (Figures 4.1.1 to 4.1.4) reflect data processed with a dry refractive index of 1.520-0i for JD 195 to 221 and 1.501-0i for JD 222 to 233, based on reconstruction of ambient aerosol refractive index for those time periods during SEAVS (Appendix D). Distributions statistics for the entire study for data processed with a refractive index of 1.530-0i, as well as the two refractive indices that represent a best estimate of the ambient dry accumulation mode aerosol refractive index during SEAVS (the refractive indices used to create graphs in this section), are included below to illustrate the sensitivity of distribution parameters derived from OPC data to the refractive index inversion.

<i>n</i>	Median	Max.	Min.	Median	Max.	Min.	Median
	Volume ($\mu\text{m}^3 \text{ cm}^{-3}$)			MMD (μm)			
1.530-0i	5.4	27.6	1.10	0.273	.344	.235	1.602
1.520-0i	6.1	34.9	1.14	0.279	.383	.239	1.640
1.501-0i							

Table 4.1.1. Dry aerosol volume distribution parameter study median and maximum and minimum values during SEAVS for two separate refractive index (*n*) inversions of the ASASP-X data from this work. Values reflect accumulation mode aerosol recorded under dry RH conditions. Note that lower refractive indices result in larger aerosol volumes and increased distribution MMD.

Accurate field measurements of ambient aerosol size distribution parameters are important in the reliable implementation of visibility and climate models (Boucher and Anderson, 1995; Pilinis *et al*, 1995). Aerosol size distribution parameter time lines, such as those in Figures 4.1.1 to 4.1.4 can also be used to estimate rates of change in particle

concentration during SEAVS stagnation episodes. For example, Figure 4.1.2 suggests that aerosol volume concentration increased at a maximum rate of $1.0 \mu\text{m}^3 \text{cm}^{-3} \text{day}^{-1}$ during the pre-hurricane period, while aerosol volume increased at over twice this rate, or $2.4 \mu\text{m}^3 \text{cm}^{-3} \text{day}^{-1}$, during the transition period. The aerosol MMD and number concentration also increased during the stagnation episodes. Aerosol volume (or mass) accumulation rates are potentially useful in the prediction of visibility degradation and acidic deposition for specific regions, meteorological conditions, and pollutant mass emission rates. In principle, the accumulation rate of ambient particulate mass should be related to emissions provided meteorological variables and removal terms can be constrained.

The experimental RH of dry aerosol size distributions represented by plots in this section was less than 10%, as shown by the grand average of daily averaged dry RH given in Table 4.1.1. On Julian Days 199-201 and 233 the ASASP-X sampled aerosol only at ambient RH. The size distribution parameters shown in Figures 4.1.1 to 4.1.4 for these days represent aerosol at RHs listed in Table 4.1.1, often the lowest available ambient RH distributions recorded on that day. Ambient RH size distribution data are included to make more continuous time lines, although data from these days are not used in derived quantities presented in this work. Julian days 117, 118 and 231 have no ASASP-X data and are therefore not included in the plots in this section. Error bars in Figures 4.1.1 to 4.1.4 represent \pm one standard deviation in the daily averaged quantity. Deviation in the daily averages is largely due to temporal fluctuations in the measured quantity. For example, aerosol volume was often observed to increase over a sampling day during a stagnation episode. A lack of error bars indicates the reported value for that day is based on one size distribution.

JD	Average RH	Average Standard Deviation	n
195-198, 202-232	8.7*	1.92	130
199-201	44*	2.13	16
233	52*	4.1	2

* Represents a grand average

Table 4.1.2. RH statistics for dry aerosol timeline. During JD 199 - 201 and 233 the RH values shown are averages of ambient values in the ASASP-X sampling chamber. Exceptions to the RH < 15% criterion occur only during the beginning and post-polluted periods. n is the number of distributions the averaged quantities represent.

4.2 Aerosol Water Uptake

Figures 4.2.1 to 4.2.6 are examples of sequential dry and humidified aerosol size distributions measured by the ASASP-X during SEAVS. The first column of plots in any of these figures show aerosol number distributions, and the second column in the same row shows the number distributions converted to volume. Moving from top to bottom in any of these figures portrays a series of sequential dry-humidified-dry distributions. The initial dry distribution is superimposed on the subsequent plots as a dotted line to indicate size shifts due to associated water. The ordinate units in these plots are explained in Appendix C3. The refractive index against which the OPC data was processed is included, as is RH to which the inversion refractive index specifically applies. These plots include the distribution run number, experimental RH, integrated distribution number or volume concentration, and distribution statistics, which apply to accumulation mode aerosol.

Figure 4.2.1 shows sequential dry and humidified aerosol distributions from JD 206, during the 'dust episode' meteorological period. An obvious large aerosol mode is present in these volume distribution plots. The large mode probably contains most of the crustal material associated with the particle fine mass during this period. The accumulation mode (demarcated by the dot-dash line) is defined here as aerosol with diameters less than the cutoff parameter shown on the volume plots. The first and last distributions in Figure 4.2.1 are for 'dry aerosol' (runs 4 and 8). Both the shape (indicated by the dotted line) and integrated volume of the accumulation mode are preserved from initial to final dry size distributions (e.g., volumes of 3.8 and 4.1 $\mu\text{m}^3 \text{cm}^{-3}$, respectively. The accumulation mode volume at 73 and 64% RH are 7.3 and 6.8 $\mu\text{m}^3 \text{cm}^{-3}$, respectively. Note that the large mode aerosol volume appears to increase from run 4 to run 8, possibly due to ambient fluctuations in the large aerosol mode.

Analogous examples of sequential dry and humidified aerosol number and volume distributions for JD 207 to 229 are included in Figures 4.2.2 to 4.2.6. On JD 207 a large aerosol mode indicative of crustal material is still evident. Subsequent plots correspond to the transition and polluted periods when the large aerosol mode is noticeably absent. Figure 4.2.3, for JD 223, shows that over the period of one RH cycle the dry aerosol volume increased by approximately 25%. These distributions were taken during an afternoon upslope flow event which coincided with variable ambient [CN]. In the example shown in Figure 4.2.3 the best estimate of dry aerosol volume for a water uptake derivation based on the humidified run is the average of the two adjacent dry aerosol volumes. During the polluted period, the mean size of the accumulation mode increased. Figure 4.2.4 indicates a well defined accumulation mode in the number distribution plots that was not present during some earlier periods of the study. This feature is observed throughout the polluted period.

All dry and humidified aerosol distributions statistics measured during this work, as well as some derived quantities explained later in this chapter, are included in Table 4.2.1.

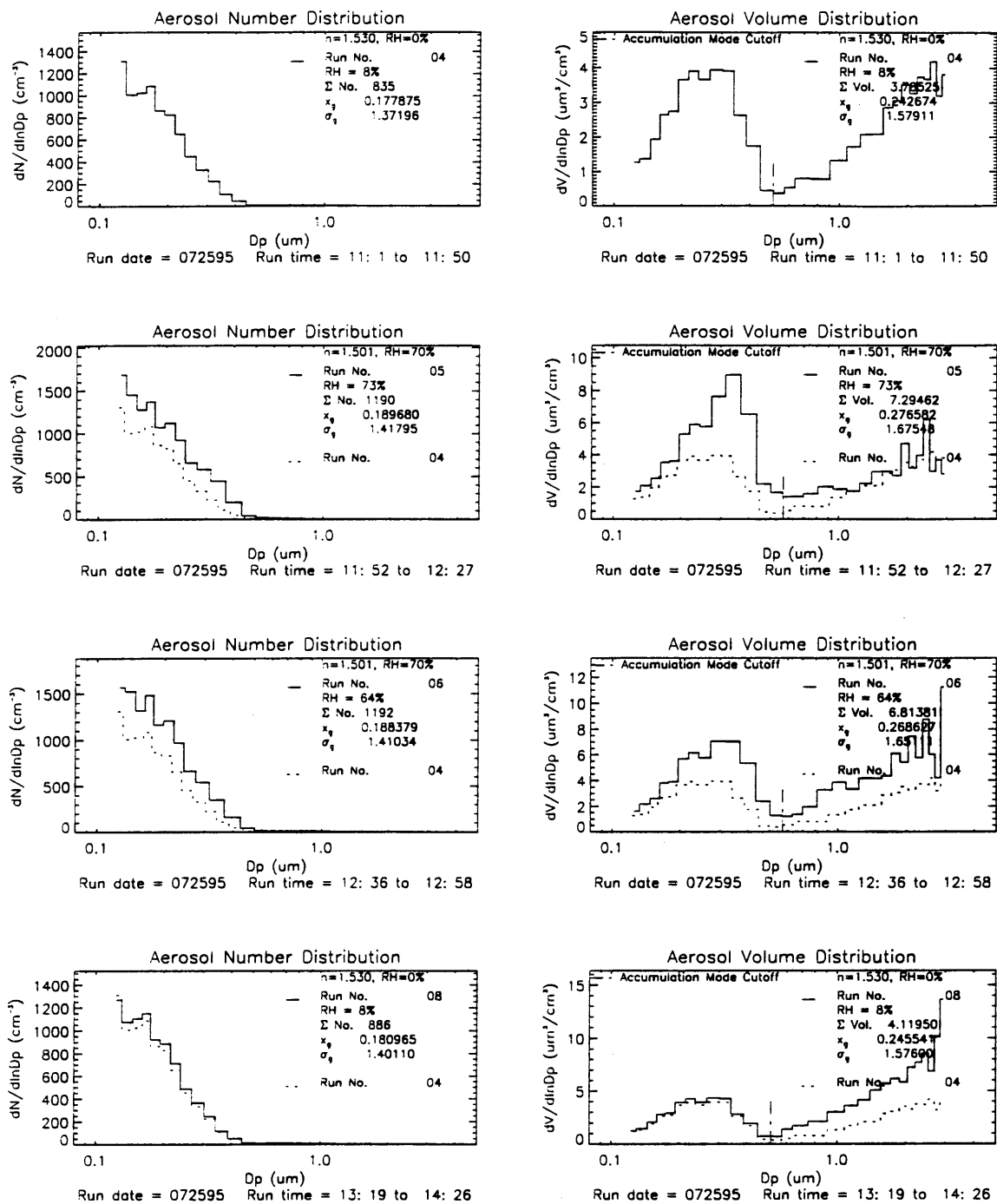


Figure 4.2.1. Sequential dry-humidified-humidified-dry aerosol distributions from JD 206 are shown in the right hand column with their corresponding volume distributions in the left hand column. Size shifts are indicated by deviations from the dotted 'dry distribution' line.

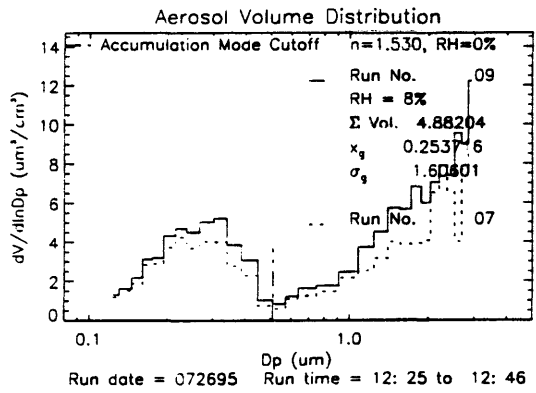
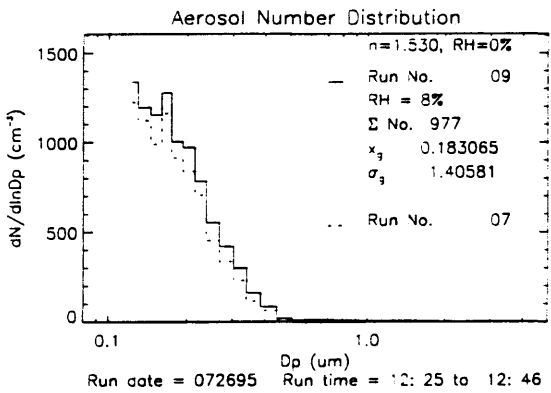
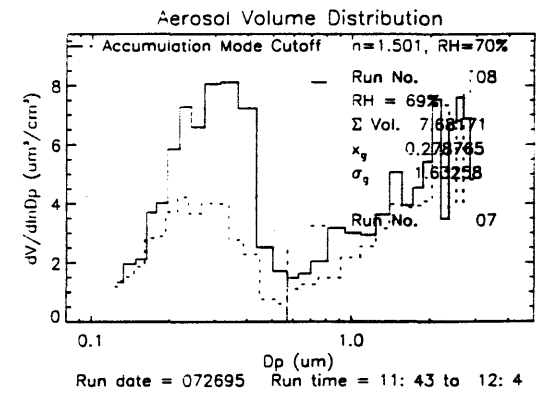
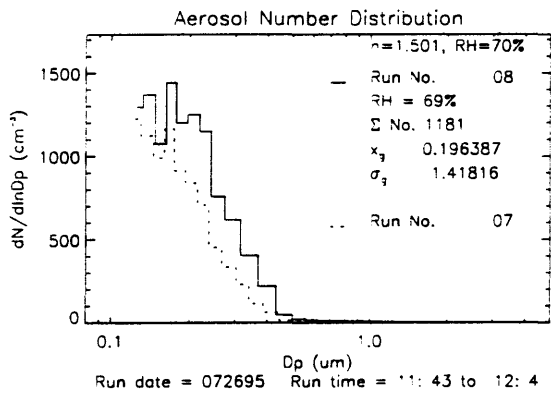
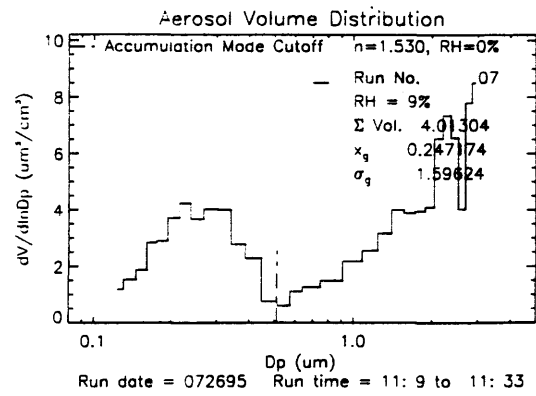
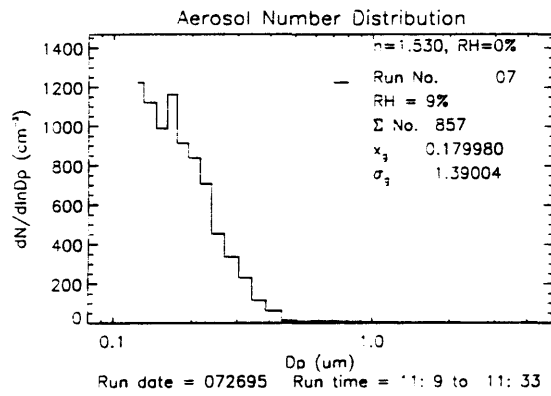


Figure 4.2.2. Sequential dry-humidified-dry aerosol distributions from JD 207, during the SEAVS dust period. Presence of the large aerosol mode seen here corresponds to crustal elements detected in the chemical fine mass during SEAVS.

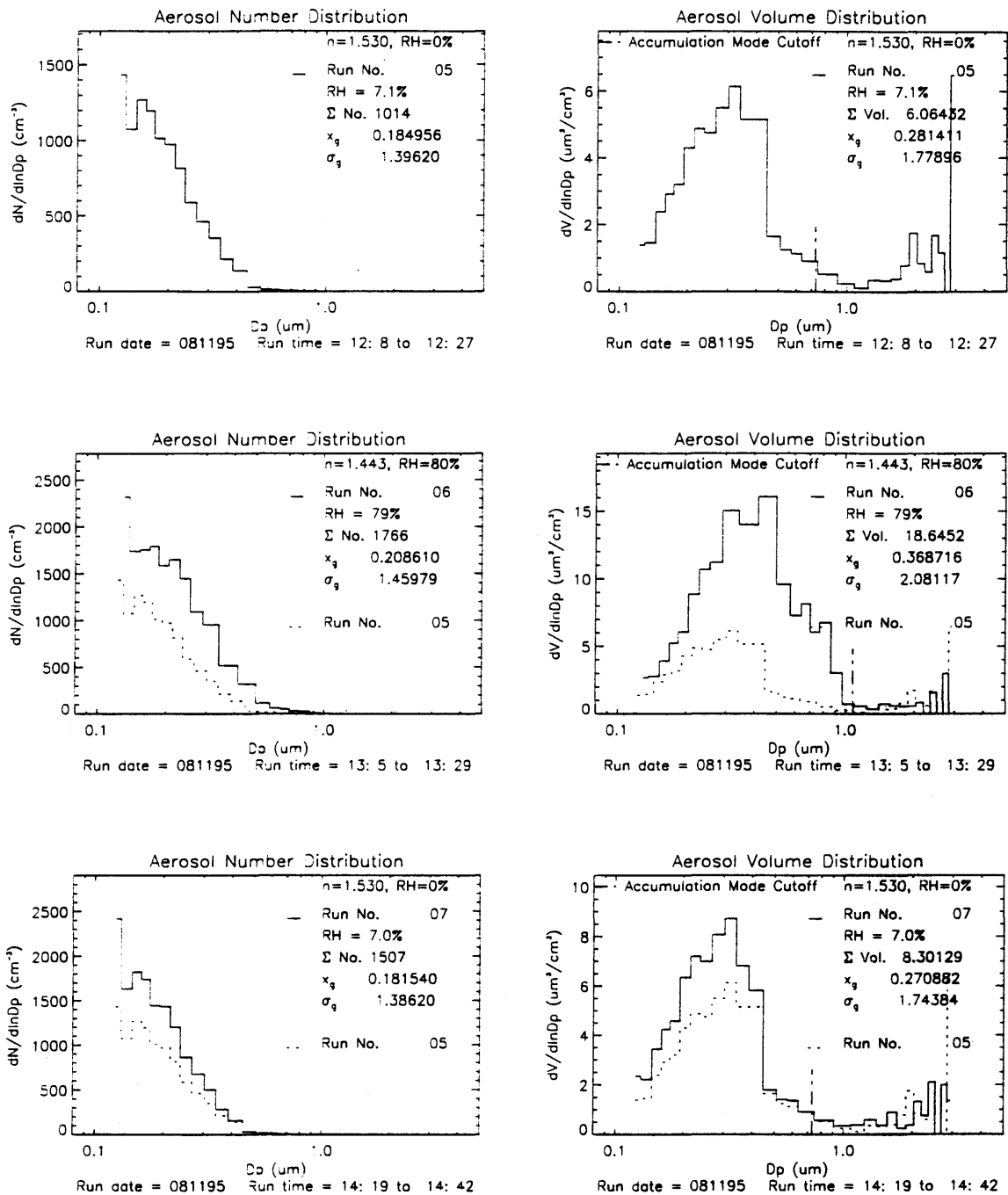


Figure 4.2.3. Sequential dry-humidified-dry distributions from JD 223, during the SEAVS transition period. Note the increase in dry aerosol volume from run 5 to run 7, typifying the temporal fluctuations in [CN] observed during this period.

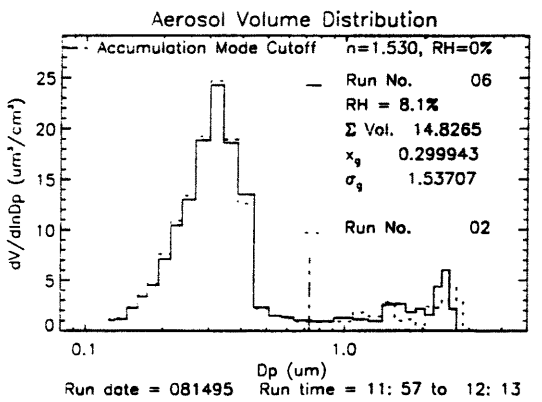
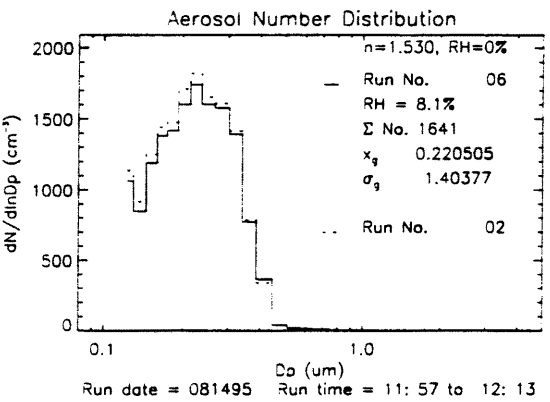
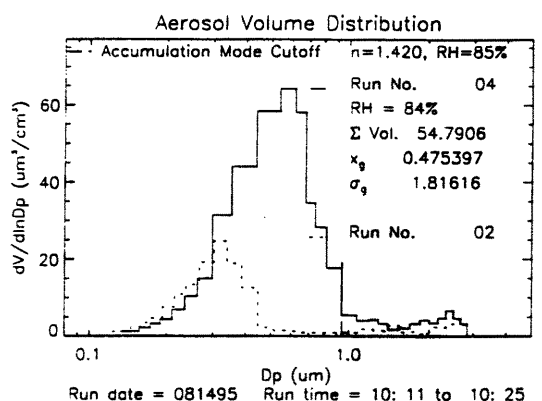
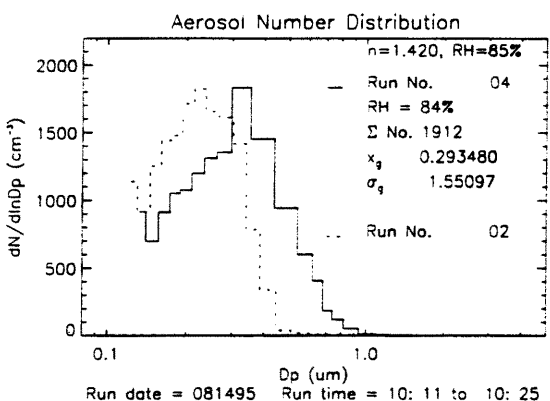
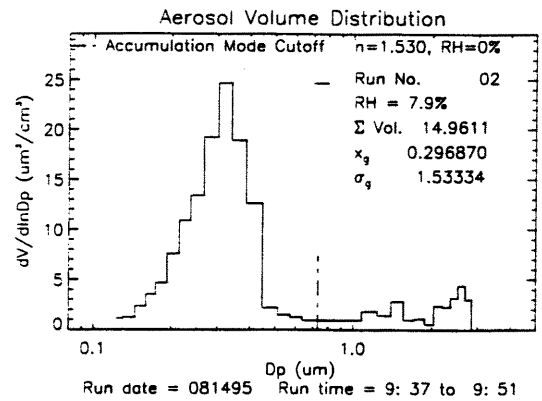
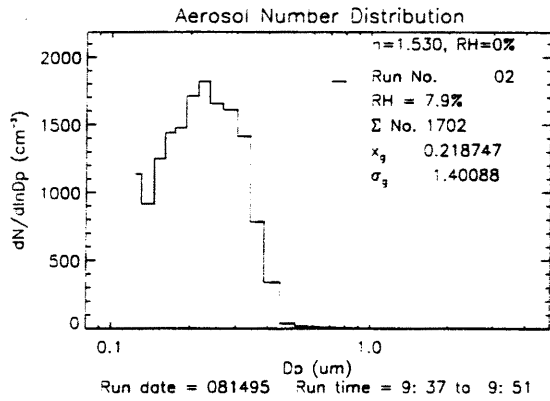


Figure 4.2.4. Sequential dry-humidified-dry distributions from JD 226, during the SEAVS polluted period. Note the well defined accumulation mode in the number distribution, an indication that the aerosol mean size has increased relative to earlier periods during SEAVS.

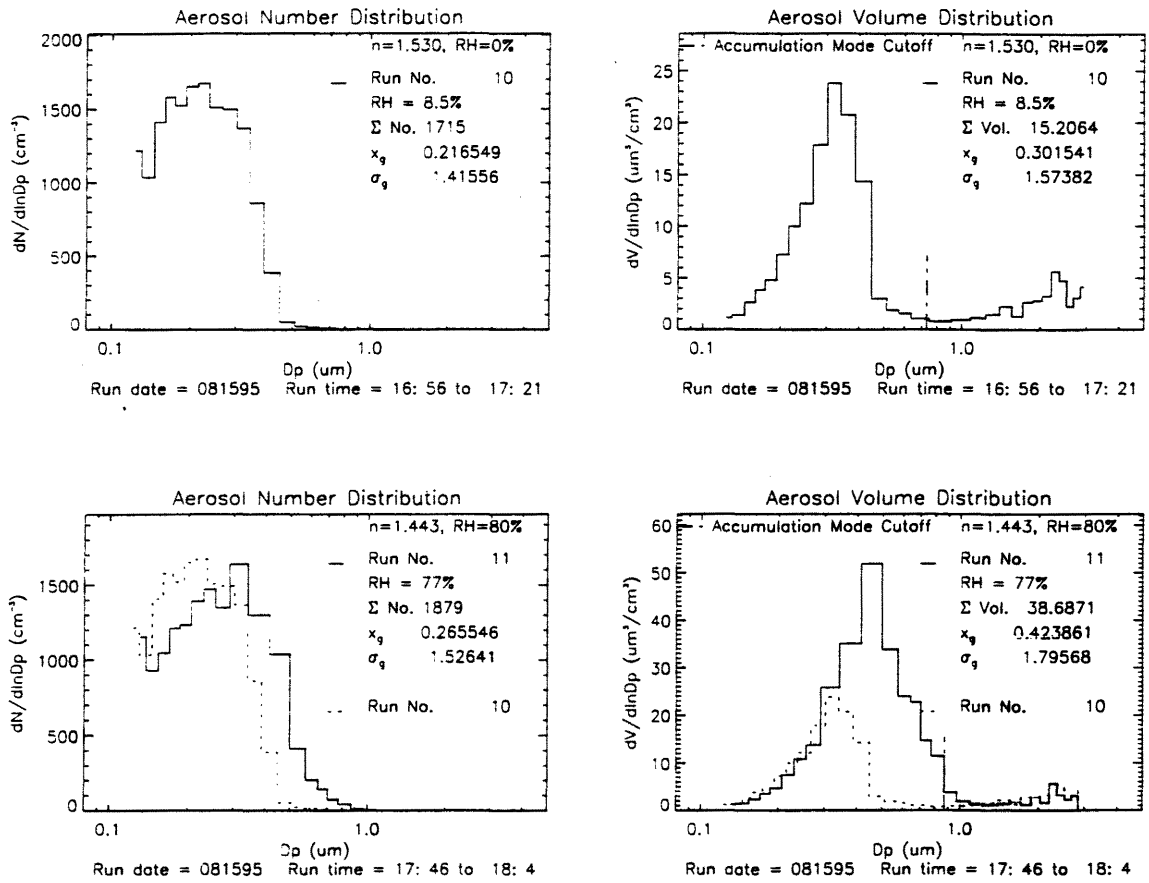


Figure 4.2.5. Sequential dry-humidified distributions from JD 227. In some cases dry distribution data were available only before or after a humidified run.

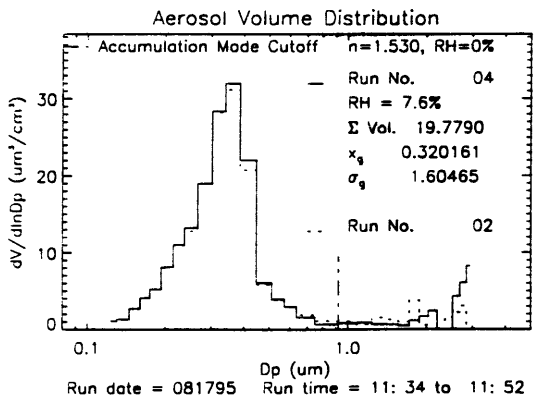
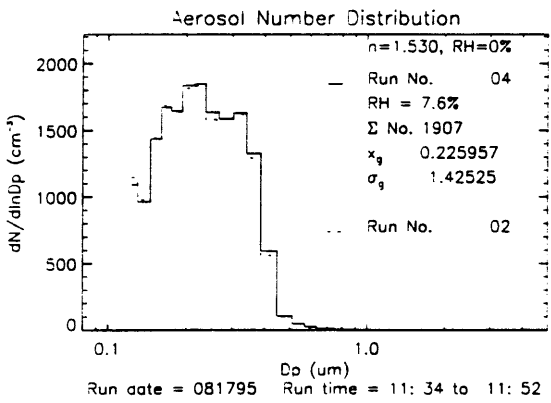
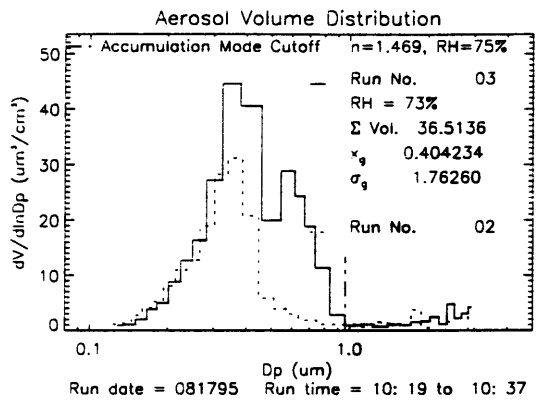
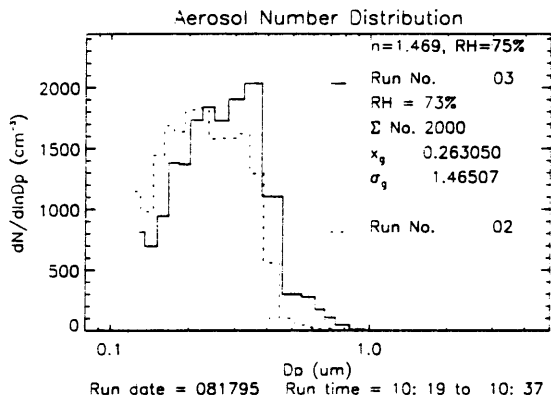
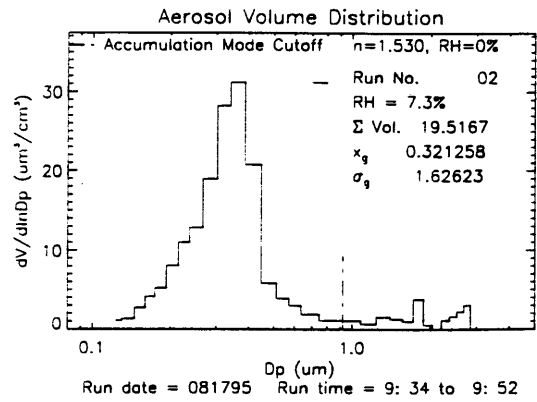
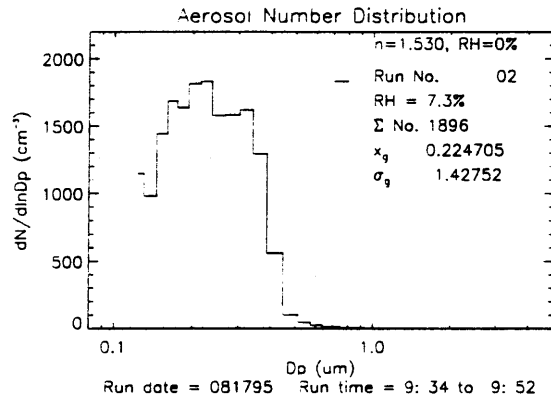


Figure 4.2.6. Sequential dry-humidified-dry distributions from JD 229. The sharp drop in the distribution near $0.5 \mu\text{m}$ D_p is indicative of skew often observed in OPC aerosol size distributions.

4.3 Derived Wet-to-Dry Aerosol Diameter Ratios

Particle size change as a function of RH can be expressed as a wet to dry particle diameter ratio,

$$\frac{D}{D_o} = \left(\frac{V}{V_o} \right)^{\frac{1}{3}} \quad 4.3.1$$

where D is the particle diameter at a given RH and D_o is the dry particle diameter. In this expression for D/D_o , hereinafter referred to as R , V and V_o are wet and dry integrated aerosol volume concentrations, respectively, from sequential dry and humidified size distributions. Alternatively, R can be expressed as the volume geometric mean diameter, $D_{p,g}$ (MMD), ratio of the humidified and dry aerosol volume distributions, provided that water uptake across the aerosol size distribution is homogenous.

$$\frac{D}{D_o} = \frac{D_{p,g}(WET)}{D_{p,g}(DRY)} \quad 4.3.2$$

McMurry *et al.*, (1996) reported size classified particles measured during SEAVS exhibited similar hygroscopic growth characteristics between diameters of 0.1 and 0.4 μm , suggesting particle hygroscopicity across the aerosol accumulation mode is homogenous. Table 4.2.1 includes values of R for accumulation mode aerosol calculated by Equation 4.3.1 and Equation 4.3.2. Values of R for aerosol in the entire ASASP-X detection range calculated by Equation 4.3.1 are also included in Table 4.2.1. Generally, R calculated by Equation 4.3.1 for the accumulation mode, and R calculated for the entire ASASP-X size range, are consistent. However, during periods with significant large mode aerosol, R calculated for accumulation mode aerosol alone typically exceeds R calculated by including the large mode aerosol into the integrated volumes used in Equation 4.3.1. This apparent preferential water

uptake by accumulation mode aerosol may be an artifact of the manner in which RH dependent refractive index was applied to particles larger than 1 μm (see Appendix C), although it may also reflect preferential aerosol hygroscopicity, and therefore differences in chemical composition, between the accumulation and large mode particles.

Figure 4.3.1 shows values of R from this work calculated by the volume ratio method (Equation 4.3.1). Figure 4.3.2 shows R calculated as the MMD ratio for the same sets of dry and humidified aerosol distributions as shown in Figure 4.3.1. Comparison of the two figures suggests that calculating R from the distribution MMD produces less scatter in the data when R is plotted as a function of RH for the whole study. This is reasonable since R as calculated by Equation 4.3.1 can change if the dry ambient aerosol volume is not constant over a experimental RH cycle. The aerosol distribution MMD, on the other hand, is probably less sensitive to ambient fluctuations in aerosol volume, provided the actual aerosol accumulation mode MMD does not change during a given RH cycle. The additional scatter in the R values in Figure 4.3.1 relative to Figure 4.3.2 may reflect additional uncertainty in R when aerosol size change is derived by the integrated volume method.

Examples of R for some of the SEAVS meteorological periods are shown in Figures 4.3.3 and 4.3.4. Figure 4.3.3 shows values of R measured during the pre-hurricane period and Figure 4.3.4 shows R for the transition and polluted periods. Superimposed on the experimental R values are empirical growth curves, expressed as R , for ammonium sulfate and ammonium bisulfate crystallization (Tang and Munkelwitz, 1994), as discussed in Section 2.3.

The aerosol chemical composition, particularly the sulfate, organic carbon and soil mass fractions, varied during SEAVS. Comparison of Figures 4.3.3 and 4.3.4 suggests increased aerosol hygroscopicity from a period that averaged 62% sulfate (pre-hurricane) to a

period that averaged 81% sulfate by mass (transition and polluted). The relative increase in R may be attributed to the higher sulfate mass fraction if sulfate species are more hygroscopic than ambient particulate organic carbon during SEAVS. Curves showing size change as a function of RH for internal mixtures of sulfate compounds with mass percents corresponding to the respective periods are also included in Figures 4.3.3 and 4.4.4.

Figure 4.35 is a correlation of R by the two methods (Equation 4.3.1 vs. Equation 4.3.2) and indicates that the latter technique results in lower overall experimental water uptake based on dry and humidified size distribution data from this work.

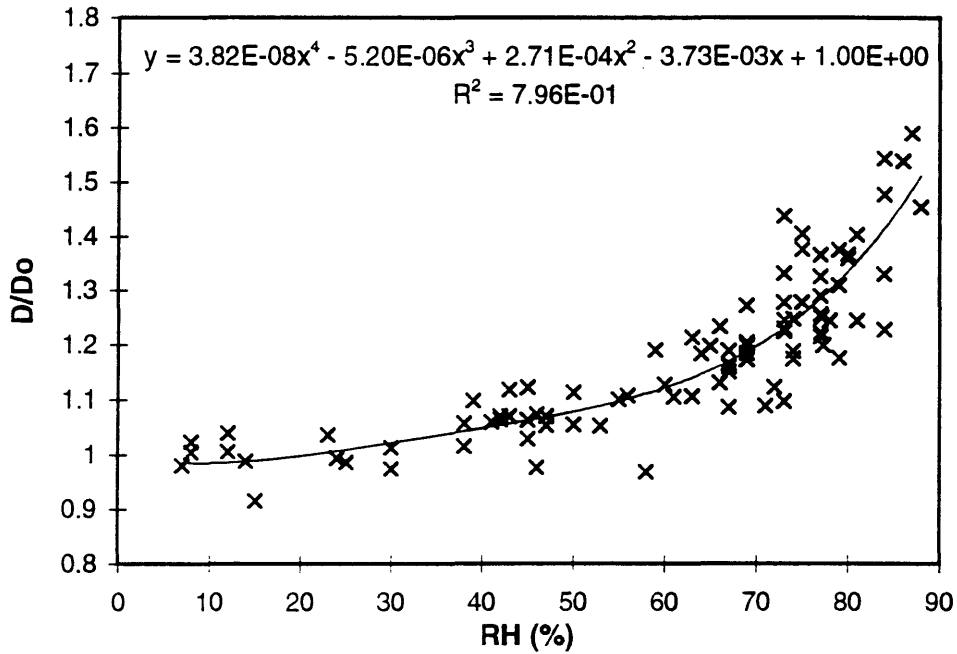


Figure 4.3.1. Aerosol size change, D/D_o , as a function of RH calculated from sequential dry and humidified integrated aerosol volume distributions.

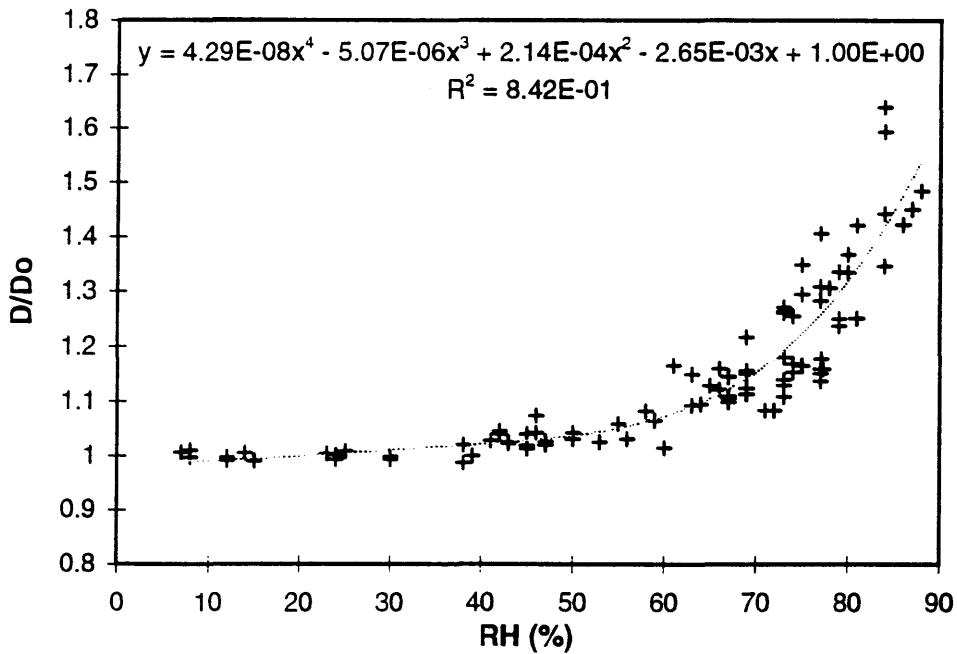


Figure 4.3.2. D/D_o for the same aerosol distributions as Figure 4.3.1 but calculated as the wet to dry MMD ratio.

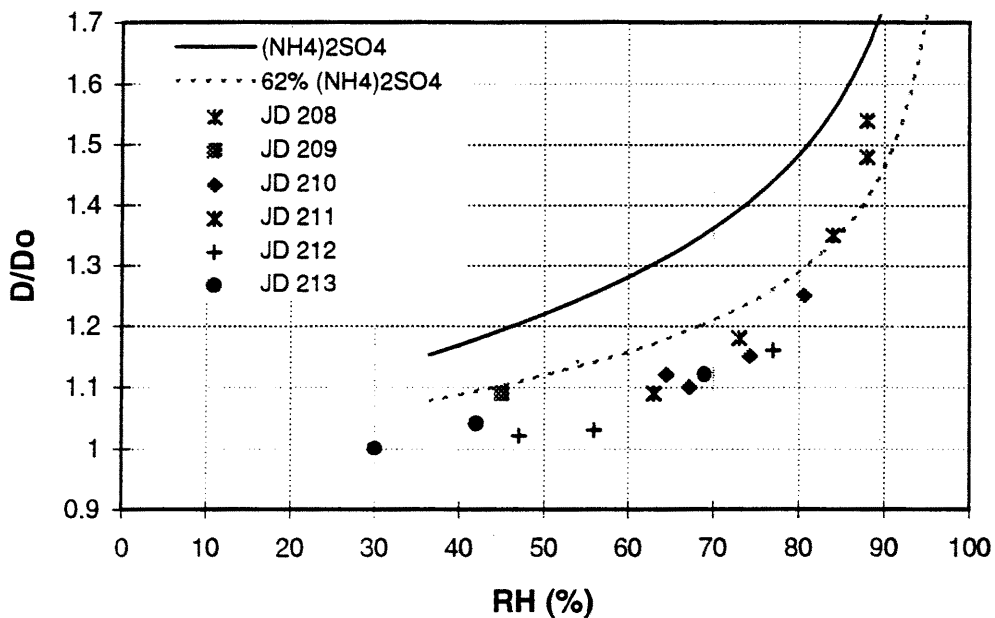


Figure 4.3.3. D/D_o for the pre-hurricane period calculated as the wet to dry MMD ratio. Estimated R for pure and 62% ammonium sulfate particles are superimposed.

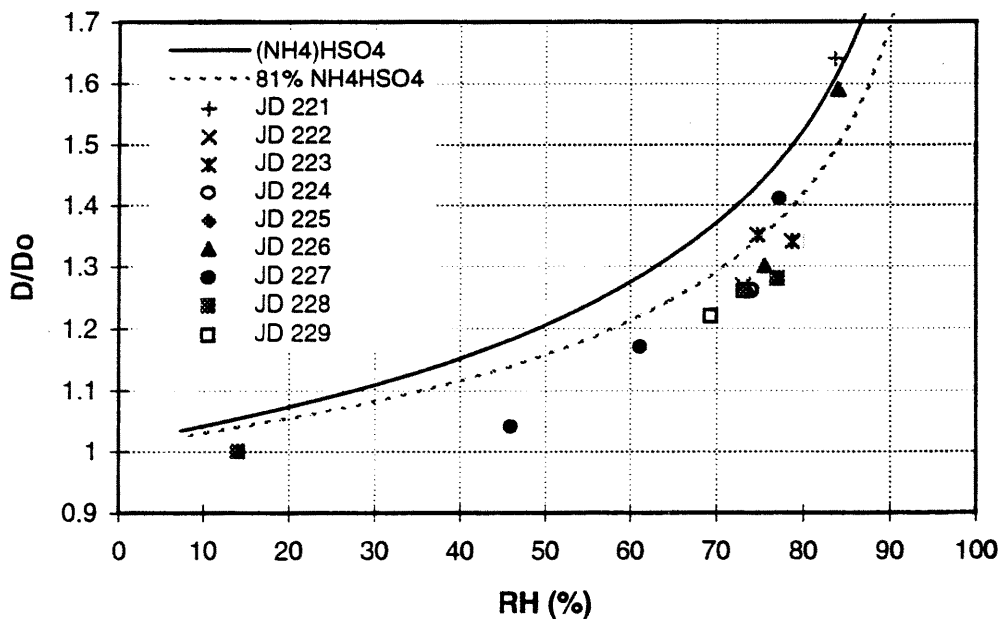


Figure 4.3.4. D/D_o for the transition and polluted periods calculated as the wet to dry MMD ratio. Estimated R for pure and 62% ammonium sulfate particles are superimposed

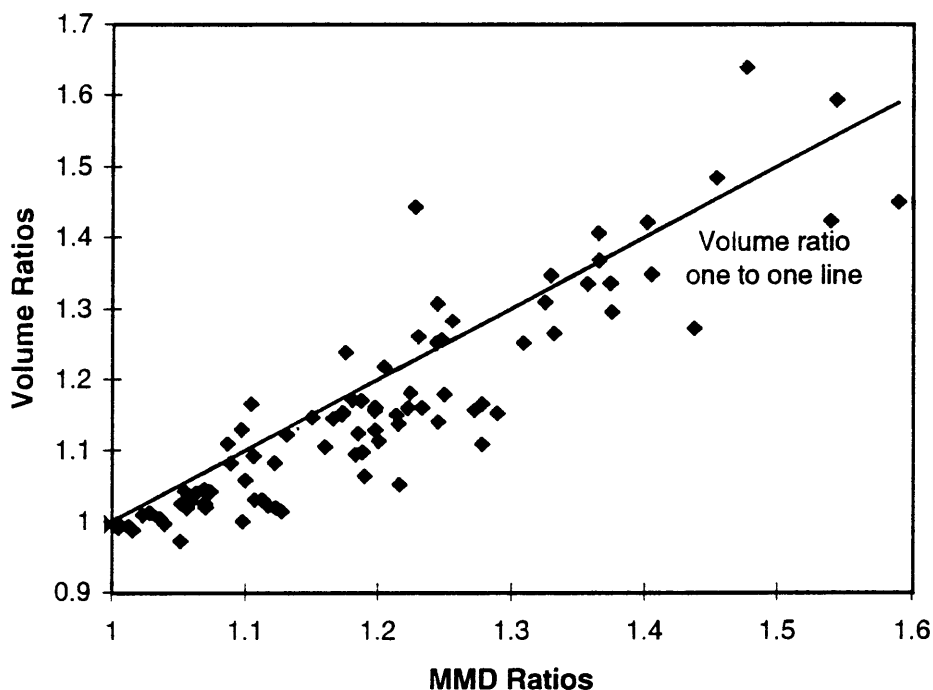


Figure 4.3.5. R for the volume ratios versus R for the MMD ratio methods using respective values plotted in Figures 4.3.1 and 4.3.2.

4.4 Uncertainty Analysis

A variety of factors can contribute to uncertainty in derived water content and ambient aerosol hygroscopic growth factors when these quantities are measured by an OPC in the field. Uncertainties inherent to the experimental design, such as flow rate, ambient aerosol number and volume stability, and in this experiment, the accuracy of RH control, can potentially propagate to the derived growth factors. The OPC itself has uncertainty in its particle sizing, a result of experimental limitations in the width of the OPC response channels (Herring and McMurry 1991; Garvey and Pinnick, 1983). Further uncertainty in derived water uptake results from correcting the OPC data for changes in aerosol index of refraction at high humidities. Table 4.4.1 summarizes sources of uncertainty and their

approximate magnitude for experimental data and theoretical corrections applied in this work.

Sources of Uncertainty	Estimated % Uncertainty
RH control	1 to 5%
Ambient Volume Stability	1 to 5%
Flow Rate	< 5%
Particle Concentration	$\propto \frac{1}{\sqrt{c}}$
Instrument uncertainty in OPC, σ_{exp}	0.02 μm in D_p
Refractive Index Correction, σ_m	0 to 0.08 μm , depending on RH

Table 4.4.1. Sources of uncertainty in derived quantities from ASASP-X data. The variable c equals the accumulated counts in a given size channel.

As a first step in calculating uncertainty in R , the uncertainty in the particle number concentration is calculated. The approach used to propagation uncertainty, up to Equation 4.4.2 in this section, is adopted from Willeke and Baron, (1993). Uncertainty in the number concentration in each OPC bin can be expressed in terms of the ASASP-X sample flow rate, Q , and flow rate standard deviation, δQ , taken from experimental measurements. The particle count in each bin, c_i , and the count standard deviation, δc_i , are related by Poisson statistics by:

$$\delta c = \sqrt{c} \tag{4.4.1}$$

The propagated uncertainty in number concentration, N , where $N = c/Qt$ and t is the sampling time period in bin i , is obtained by taking the partial derivative of N with respect its independent variables. The variance in N is assumed to be equal to the sum of the of the variances in the individual independent variables multiplied by the square of their respective

partial derivatives. The resulting standard deviation in N is given by Equation 4.4.2 where the variance in t has been neglected:

$$\delta N_i = \left[\left(\frac{1}{Qt} \right)^2 (\delta c_i)^2 + \left(\left(\frac{-c_i}{Q^2 t} \right)^2 (\delta Q^2) \right) \right]^{\frac{1}{2}} \quad 4.4.2$$

The standard deviation in aerosol volume concentration for a given OPC bin is obtained in a similar manner to the number concentration standard deviation, where the aerosol number has been converted to volume based on the midpoint diameter of bin i , $D_{pm,i}$. Uncertainties in $D_{pm,i}$ and N_i are propagated through Equation 2.4.4 in a manner analogous to that used for the uncertainty calculations in N_i , resulting in:

$$\delta V_i = \left[\left(\frac{\pi}{2} D_{pm,i}^2 N_i \right)^2 (\delta D_{pm,i})^2 + \left(\frac{\pi}{6} (D_{pm,i}^3) (\delta N_i)^2 \right) \right]^{\frac{1}{2}} \quad 4.4.3$$

In Equation 4.4.3 the uncertainty in particle diameter, $\delta D_{pm,i}$, is given by the uncertainty in experimental measurements of particle diameter, σ_{exp} , and the uncertainty in particle diameter due to applied refractive index correction, σ_m .

$$\delta D_{pm,i} = \left(\sigma_{exp}^2 + \sigma_m^2 \right)^{\frac{1}{2}} \quad 4.4.4$$

Since refractive index corrections are greater at higher humidities, σ_m becomes greater as refractive index decreases. For this work, σ_{exp} is assumed to be 0.02 μm . σ_m is assumed to vary with the inversion refractive index as indicated in Table 4.4.2.

n	1.530	1.520	1.501	1.469	1.443	1.420
σ_m	0	0.01 μm	0.03 μm	0.05 μm	0.07 μm	0.08 μm

Table 4.4.2. σ_m as a function of the OPC data inversion refractive index.

The uncertainties in the integrated number and volume concentrations can be expressed in terms of the respective individual bin uncertainties:

$$\delta N = \left(\sum_{i=1} \delta N_i \right)^{1/2} \quad 4.4.5$$

$$\delta V = \left(\sum_{i=1} \delta V_i \right)^{1/2} \quad 4.4.6$$

The expression for the total number and volume concentration uncertainties would be true if all the bin uncertainties are independent and therefore additive, although this is not necessarily true for OPC data (Stolzenburg, personal communication).

The propagation of the uncertainties in aerosol wet to dry volume concentrations ratios can be expressed by taking the natural log of Equation 4.3.1, to give:

$$\ln R = \frac{1}{3} (\ln V_W - \ln V_D) \quad 4.4.7$$

If we assume the uncertainty in the wet and dry volumes can both add to uncertainty in R , and express uncertainty as a percent, the following expression results:

$$\frac{\delta R}{R} = \frac{1}{3} \left(\frac{\delta V_W}{V_W} + \frac{\delta V_D}{V_D} \right) \quad 4.4.8$$

where the integrated volume concentration uncertainty is given by Equation 4.4.6.

Using this approach the uncertainty in derived RH dependent aerosol size change (R) for accumulation mode aerosol measured in this work ranged from 6%, when aerosol number concentrations were high, to approximately 25%, when the aerosol number concentrations were low. Uncertainties in R for high experimental RH were somewhat greater than the uncertainties in R for lower RH.

4.5 Uncertainty Propagation in a Light Scattering Model

Estimates of uncertainty in experimental R were used for a sensitivity analysis in an optical aerosol model (Tsay and Stephens, 1990). The RH dependent aerosol growth parameters in the light scattering model were perturbed by fixed amounts. The resulting change in the wet to dry light scattering ratio for the perturbed case, expressed as a percent of the initial unperturbed scattering ratio, is shown in Table 4.5.1. A lognormal particle distribution with MMD of 0.3 μm and σ_g of 1.6 was used in the simulations. RH dependent size change along the solute crystallization branch of ammonium sulfate (Tang and Munkelwitz, 1994) was parameterized in the model prior to the sensitivity test. Table 4.5.1 summarizes the results from the sensitivity study, and indicates that modeled estimates of light scattering are not unduly susceptible to uncertainties in experimentally derived R parameterizations, provided the experimental aerosol size change uncertainty does not exceed 10%.

Positive R Perturbation	% Change in $\frac{b_{sp}(wet)}{b_{sp}(dry)}$
5%	3%
10%	18%
20%	50%
30%	220%

Table 4.5.1. Uncertainty propagation in the aerosol visibility model. The change in wet-to-dry scattering ratios shown are averages over all RH values above the solute RHC.

5. DISCUSSION

In this Chapter the ASASP-X data is compared with other data sets from SEAVS to determine if they are consistent. One comparison is that of daily averaged dry aerosol volume (Section 4.1) to chemical fine mass (particles below 2.5 μm in diameter) measured by the IMPROVE samplers. This discussion leads to estimates of dry aerosol density during SEAVS. Second, experimentally derived aerosol hygroscopicity is compared to theoretical estimates of RH dependent aerosol size change based on daily fine mass chemical composition from IMPROVE samplers.

5.1 Dry Aerosol Volume and Density

Figure 5.1.1 shows aerosol mass concentration from the IMPROVE samplers and aerosol volume concentration from the ASASP-X. Chemical fine mass is represented as sulfate, organic and elemental carbon, and soil, the significant constituents of fine mass during SEAVS (Appendix A.3). Similar trends in particle loading are seen with the ASASP-X volume concentration time line ($D_p < 2.5 \mu\text{m}$) and a time line of 12 hour averaged daytime fine mass ($D_p < 2.5 \mu\text{m}$) from IMPROVE samplers. The similar trends in aerosol loading indicate the ASASP-X size range can account for most of the ambient dry aerosol volume. However, the OPC measurements provide much greater time resolution than chemical sampling techniques.

Figure 5.1.2 shows a time line of sulfate, ammonium, organic carbon, elemental carbon, and soil mass (12 hour daytime averages, except for organic carbon, elemental carbon and soil which are taken from 24 hour averages) as a percent of the total mass, defined as the sum of the mass concentrations of sulfate, organic plus elemental carbon, and soil. These are the chemical mass fractions used to reconstruct fine mass concentration in Figure 5.1.1. The predominance of sulfates and organics in GRSM is evident from Figure 5.1.2, with sulfate comprising nearly 80%

of the fine mass during the transition and polluted periods and approximately 60% during periods of low total mass if the contribution from soil is ignored. Soil episodes are evident from the dashed line in Figure 5.1.2, the sum of sulfate, ammonium, organic and elemental carbon fine mass, which is essentially the inverse of the soil mass time line (see Figure A.3.4).

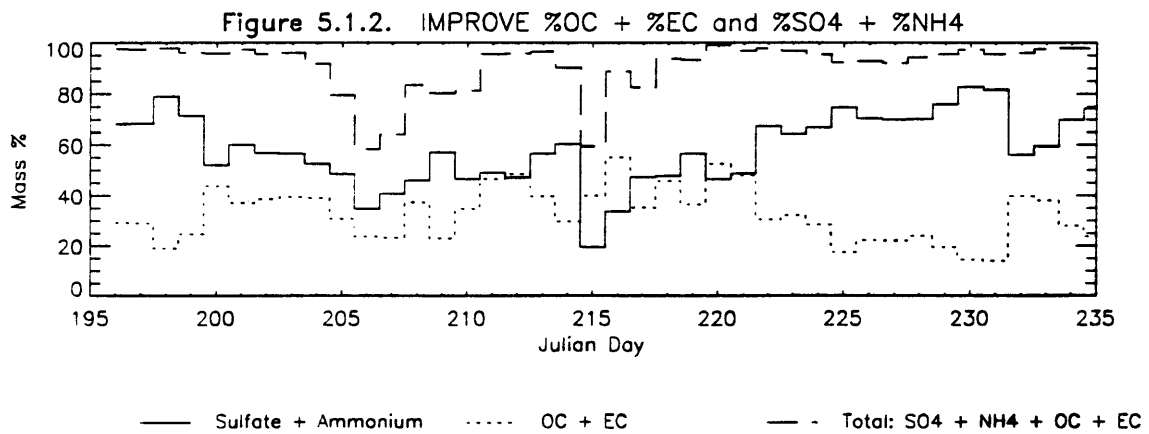
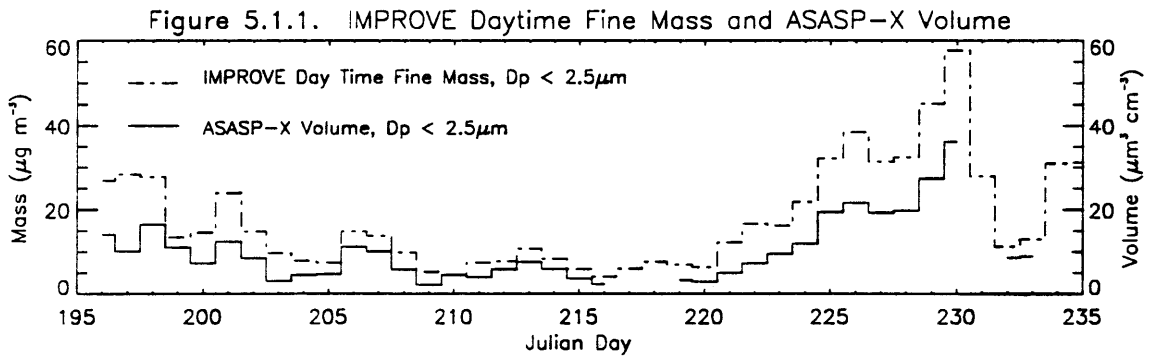


Figure 5.1.1. Daytime averages of ASASP-X dry aerosol volume vs. daytime averages of IMPROVE fine mass for sulfates, organic plus elemental carbon, and soil mass.

Figure 5.1.2. Daytime averages of sulfate + ammonium and organic + elemental carbon mass percent as a percent of total mass (sulfate + ammonium + organic and elemental carbon + soil).

The chemical mass and aerosol volume concentrations shown in Figure 5.1.1 do not include contributions from water, and therefore can be used to estimate dry aerosol density. The aerosol density (g cm^{-3}) is simply the ratio of the mass to volume concentrations.

Figure 5.1.3 is a scatter plot of daytime IMPROVE mass concentration versus ASASP-X volume concentration ($0.1 < D_p < 2.5$) for JD 196 to 233, and includes only aerosol volume concentrations measured by the ASASP-X under dry conditions when both ASASP-X and daily IMPROVE data were available. The dry aerosol volumes result from processing the OPC data at two separate refractive indices, 1.520 and 1.501 (See Section 4.1 and Appendix D). A statistical T-test to determine outlying data points was used on the set of available density values and data from JD 197 and 203 were rejected this basis.

A least squares linear regression to these data has a slope of 1.63, which is close to the median density (1.67 g cm^{-3}), calculated from the final set of 30 mass to volume ratios shown in Figure 5.1.3. It should be pointed out that the regressions shown in Figures 5.1.3 and 5.1.4 assume there is no error in the independent variable, which is not true. More appropriate techniques that consider uncertainty in aerosol volume could be applied to estimate error in the regression slope and correlation coefficient. However, the regression equation is not used to derive aerosol density in this analysis, but merely applied as a first approximation of data correlation.

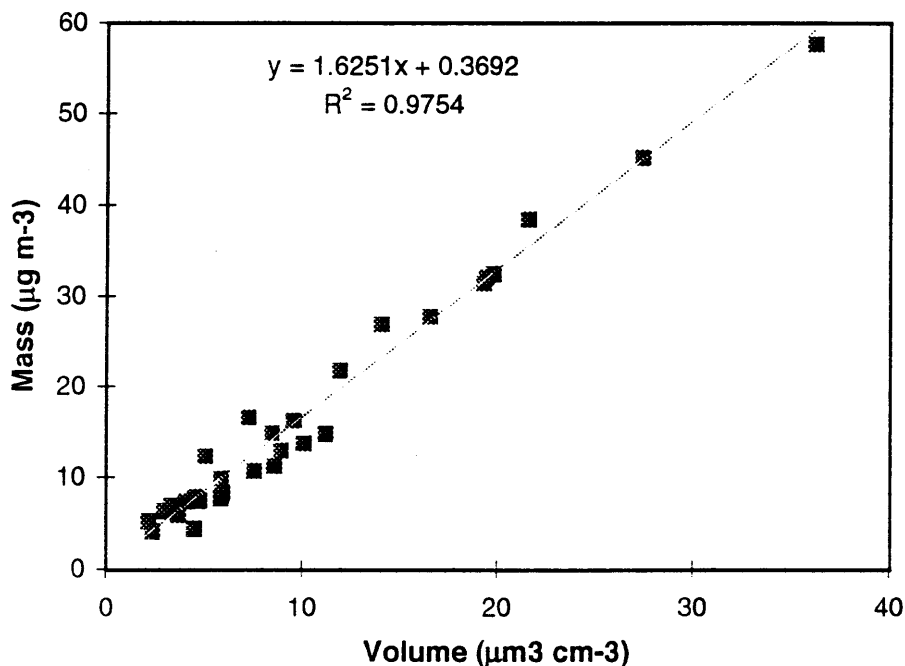


Figure 5.1.3. Correlation of IMPROVE daytime fine mass vs. ASASP-X fine volume for JD 196 to 233. Fine mass includes sulfate, ammonium, organic carbon, elemental carbon and soil. The median aerosol density, calculated as the mass to volume concentration ratio, is 1.67 g cm^{-3} . The dotted line is the least squares best fit to the data.

Dry aerosol density was next calculated for two time periods corresponding to low and high aerosol mass concentration. The low mass period, JD 204 to 221, had an average mass concentration of $8.1 \text{ } \mu\text{g m}^{-3}$, and the high mass period, JD 222 to 230, had an average mass concentration of $30.4 \text{ } \mu\text{g m}^{-3}$. These data are correlated in Figure 5.1.4. For the high mass days the median aerosol density is 1.65 g cm^{-3} , and for the low mass days the median density is also 1.65 g cm^{-3} . The y intercepts of the linear best fits shown in Figure 5.1.4 have been forced through zero. The slope of the low mass period suggests somewhat lower dry aerosol density during the low mass period, although the significance of this observation has not been determined.

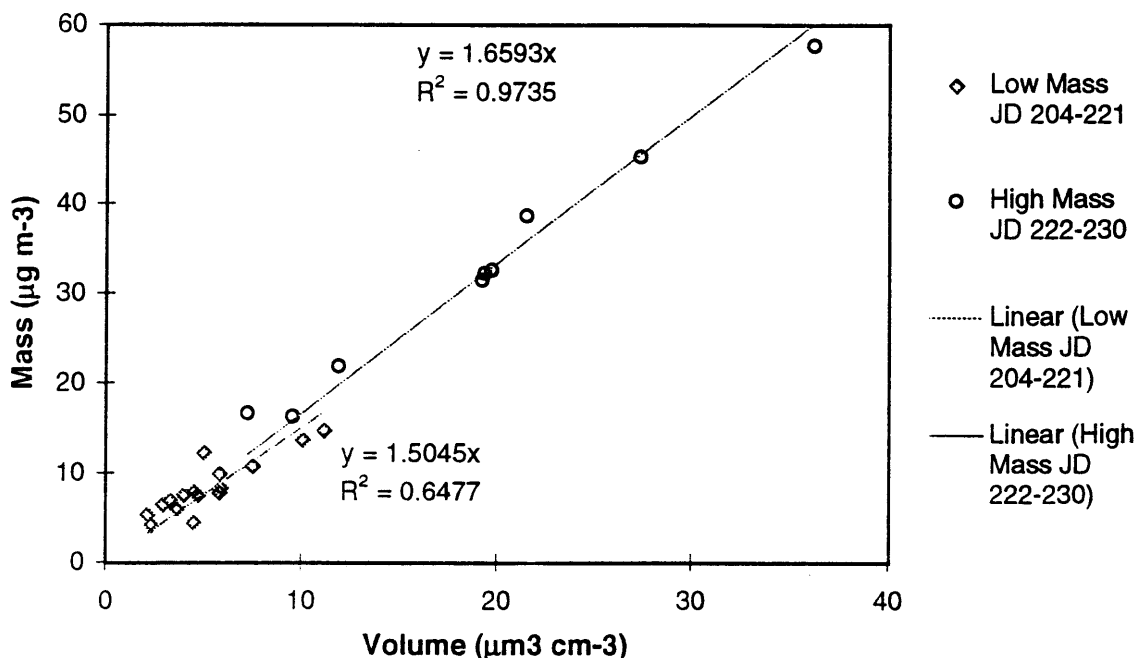


Figure 5.1.4. Correlation of IMPROVE daytime fine mass vs. ASASP-X fine volume for a low mass period (JD 204 - 221) and a high mass period (JD 222-230). Median aerosol densities are 1.65 g cm^{-3} for both periods. The dotted lines are least squares fits to the two data sets.

Quantities derived from OPC data, such as aerosol density, depend on the inversion refractive index applied to the dry aerosol. The dependence of density on the data inversion is examined here. The reconstructed dry aerosol refractive index shown in Appendix D suggests appropriate values that may be applied to SEAVS data. In order to simplify data processing, two refractive indices were applied to the OPC as a best estimate of ambient values. Results from this data inversion, and three other refractive index inversions, are shown in Table 5.1.1, and show a strong dependence of density on the assumed dry refractive index. The ambient aerosol composition during SEAVS varied and it is therefore reasonable

to conclude that the dry aerosol density was not entirely constant over time. This is reflected in the rather high standard deviations in derived densities shown below.

	ρ g cm ⁻³		ρ_L g cm ⁻³		ρ_H g cm ⁻³	
	median	s	median	s	median	s
$n1=1.520$ $n2=1.501$	1.67	.337	1.65	.420	1.65	.215
$n=1.530$	1.87	.385	1.69	.441	2.00	.264
$n=1.520$	1.81	.363	1.65	.420	1.91	.251
$n=1.501$	1.61	.303	1.53	.356	1.65	.215

Table 5.1.1. Dry aerosol densities derived from OPC data in this report and IMPROVE chemical data. n is the inversion refractive index applied to SEAVS data for JD 196 to 233 except for $n1$, which applies to JD 196 to 221, and $n2$, which applies to JD 222 to 233. ρ are median density values for the entire study. ρ_L are median densities for the low mass period JD 204 to 221. ρ_H are median densities for the high mass period, JD 222 to 230. s is the standard deviation in the respective density value to its left.

Some estimates of dry solute densities are listed in Table 5.1.2 for comparison to the experimentally derived aerosol densities. Mixed phase densities were computed assuming volume conservation of the respective pure phases (see Equation D.1.6). The mixtures of organic carbon and sulfate compounds are intended to represent the mass fraction range for these compounds observed during SEAVS. Since the OPC data used in this analysis is for $D_p < 2.5 \mu\text{m}$, soil mass, with density perhaps greater than that of compounds in Table 5.1.2, may contribute to the aerosol density derived from experiment. Since the soil mass over the whole study period is small, the contribution of soil to aerosol

density over the entire SEAVS period should also be small. Choices of refractive index for the data inversion that are based on the changing aerosol composition bring the derived densities into better agreement with those expected for a mixture of sulfates and organics.

Compound	Density (g cm ⁻³)	
Ambient Dry Aerosol	1.67	<i>n</i> = 1.520
Study median, this work		<i>n</i> = 1.501
Ammonium sulfate	1.769	a
Ammonium bisulfate	1.78	a
Sulfuric acid (98%)	1.841	a
Organic carbon	1.40	b
85% ammonium bisulfate, 15% organics, by mass	1.67	c
60% ammonium sulfate, 40% organics, by mass	1.63	c

n = Refractive indices used to process dry aerosol size distributions.

a CRC, 46th edition.

b Stelson (1990).

c Calculated by volume conservation.

Table 5.1.2. Dry aerosol density averaged for the entire SEAVS period assuming dry aerosol refractive index, *n*. Also shown are dry densities of common atmospheric aerosols and the calculated densities for some mixtures of these compounds.

5.2 Derived Aerosol Hygroscopicity

Aerosol water uptake derived from experimental measurements in this work is compared to estimated aerosol water uptake based on the ambient ionic chemical mass fraction determined from IMPROVE data. Aerosol hygroscopicity is estimated by adding water to the ionic mass according to empirical formulas that express pure solute water uptake. This comparison allows determination of the presence or lack of excess water in the ambient aerosol beyond the contribution from ionic compounds. Since organic carbon is the other predominant mass fraction in the accumulation mode, deviations from the estimated water uptake can be attributed to organics species.

The method used to estimate water uptake in this work assumes that all particles follow the crystallization branch of aerosol size change as a function of RH. Owing to the experimental design this may not necessarily be a valid assumption if the ambient aerosol were not deliquesced prior to humidification. Also, the theoretical aerosol hygroscopicity estimates assume all particles have the same internally mixed composition.

The mixing rule from Malm and Kreidenweis (1996), Equation 2.3.4, is used to estimate aerosol hygroscopicity based on daytime chemical mass fractions. Sulfate and ammonium ions and organic and elemental carbon are assumed to be the only components in the accumulation mode aerosol. Respective mass fractions of these species are taken from daytime IMPROVE data. In the mixing equation (Equation 2.3.4), sulfate and ammonium ionic mass are treated as the only hygroscopic fractions and are characterized as ammonium bisulfate with RH dependent water content, expressed as R , adopted from Tang and Munkelwitz (1994). Representing water uptake with ammonium bisulfate is justified by the fact that the average ammonium to sulfate molar ratio during SEAVS was approximately equal that of ammonium bisulfate (see Figure A.3.8). Also, for particle sulfate acidity

between that of ammonium bisulfate and ammonium sulfate, there is little difference in the RH dependent size change over the range of humidities applied in this experiment.

Correlations of experimental to estimated R are shown in Figure 5.2.1 and Figure 5.2.2.

Experimental R values in Figure 5.2.1 are derived from the volume ratio method and those in Figure 5.2.2 are derived from shifts in the aerosol MMD, as discussed in Section 4.3. Only experimental data points measured at RH above 36 % are included. Values representing RH > 80% are denoted by open circles.

The data shown in Figures 5.2.1 and 5.2.2 suggest the estimated water uptake by ionic species overpredicts actual measured aerosol water uptake. For all derived R values above 36% RH, the estimated water uptake overpredicts R calculated by the volume ratio method (Equation 4.3.1) by an average of 9%, while estimates overpredict water uptake calculated by MMD ratio method (Equation 4.3.2) by an average of 11%. Since the theoretical estimates of R correspond to the crystallization branch of particle size change, the assumption that all soluble aerosol have deliquesced is inherent. If, for example, only some fraction of the particles in the size distribution have deliquesced at a given RH then estimates of R would overpredict water uptake at that RH. The theoretical estimates of ionic species hygroscopicity represents an upper limit in R below the solute RHD, provided particle acidity does not exceed that of ammonium bisulfate.

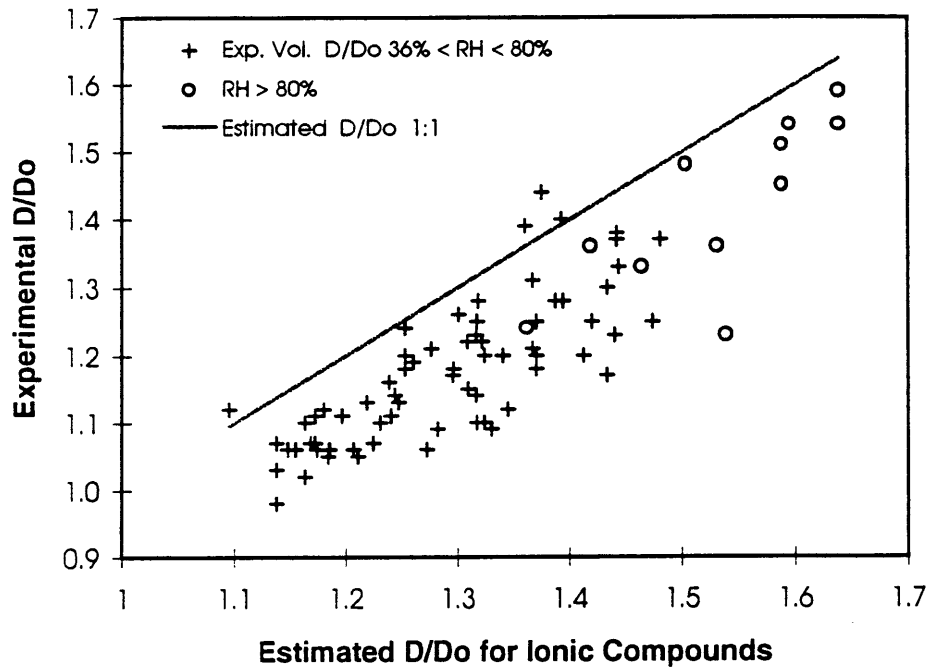


Figure 5.2.1. Experimentally derived R , based on wet-to-dry accumulation mode volume ratios from the ASASP-X, versus R estimated for daytime ionic mass.

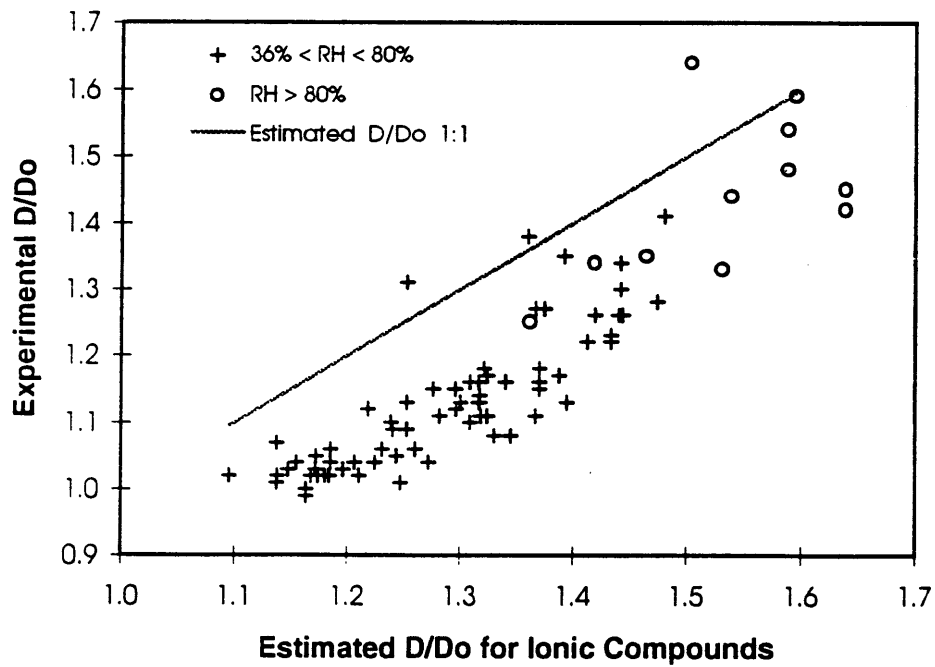


Figure 5.2.2. Experimentally derived R , based on wet-to-dry accumulation mode ratios from the ASASP-X, versus R estimated for daytime ionic mass.

A more reliable comparison is to see if the experimental R values above 80% RH are significantly different than the estimated water uptake. Above 80% RH all sulfate and most organics that exhibit deliquescence should have associated water and estimated water uptake should be comparable to experimental values. With this criterion applied, estimated water uptake overpredicts experimental water uptake by 7% and 6% for the volume and MMD ratio methods, respectively. Since the uncertainty in experimentally derived R from this work is shown to be at least 6%, these experimental data cannot be concluded as significantly different than the estimates of water uptake for ionic species alone. However, these results suggest ambient sulfate complexes can explain measured aerosol water uptake above the ammonium sulfate RHD.

A shortcoming of the theoretical R estimates is the lack of detailed chemical information for accumulation mode aerosol. If some fraction of the accumulation mode particulate mass is soil, or other insoluble species, then the estimated water uptake would decrease in an amount proportional to the soil mass fraction in that size range. Another shortcoming in the aerosol water uptake estimates used above is that they were based on experimental observations at 25° C, whereas most of the experimental water uptake measurements in this work were made near 30° C. However, water activity is not expected to change significantly for this small of a temperature change.

An alternative approach to estimating particle growth, rather than using the crystallization branch of particle size change, is to use an approximation of R at humidities below the solute RHD. Malm *et al.* (1994) used a growth curve that smoothed through the ammonium sulfate hysteresis region to reconstruct ambient light extinction. This type of water uptake parameterization would decrease the water uptake estimated for ionic species below the solute RHD. However, there is no compelling theoretical basis for making such an

approximation to theory and then using this approximation in comparison to experimental data. On the other hand, the aerosol size change parameters obtained in this work may very well reflect the hygroscopic behavior of ambient aerosol in a natural setting since all experimental RH values are direct shifts from ambient RH. Indeed, the RH dependent aerosol size change, such as those shown in Figures 4.3.1 and 4.3.2, may serve as useful water uptake parameterizations in light scattering models when these models are applied to low level atmosphere typical of the rural southeastern U.S.

6. CONCLUSION

This study indicates the ASASP-X provided a reliable measurement of ambient dry aerosol size distribution parameters during SEAVS. A median accumulation mode volume concentration of $6.1 \mu\text{m}^3 \text{cm}^{-3}$, with a median MMD of $0.28 \mu\text{m}$ and median volume distribution σ_g of 1.64 are reported for the aerosol distributions measured during SEAVS in this work.

When the OPC volume concentrations ($D_p < 2.5 \mu\text{m}$) are compared to chemical fine mass concentration from IMPROVE samplers, reasonable estimates of dry aerosol density for the aerosol during SEAVS are obtained, although the results are sensitive to the choice of refractive index. Aerosol mass concentrations can be derived from OPC data with additional measurements of aerosol chemistry, although a less rigorous chemical sampling protocol than was used with the IMPROVE samplers during SEAVS would suffice. Current visibility and climate models can benefit from accurate ambient aerosol size distribution parameters that are both regionally specific and provide detailed temporal resolution.

The results from the hygroscopicity study indicate that the ASASP-X, coupled with a RH controlled sample inlet, was able to resolve trends in water uptake by accumulation mode aerosol, and that those trends were consistent with theory. This work suggests that the upper limit of experimentally derived aerosol water uptake as a function of RH is bounded by estimates of aerosol size change for a deliquesced mixed phase of ammonium bisulfate weighted to the ionic mass fraction observed during SEAVS. The experimental wet to dry diameter ratio about 10% less than that estimated by theory for ionic sulfate compounds present in the aerosol during SEAVS. Since the uncertainty in derived water uptake from this work was found to average approximately 14%, it cannot firmly be concluded that organic carbon in SEAVS aerosol either inhibit or enhance ambient aerosol water uptake.

There is obvious scatter in the experimentally derived aerosol size change as a function of RH. Some possible sources of this scatter, which may not contribute to uncertainty in R directly, though may add to scatter in the comparisons of experimental versus estimated water uptake presented in Figures 5.2.1 and 5.2.2, are considered as follows. More detailed chemical data for the accumulation mode aerosol would help to improve the water uptake estimates. It is likely, for example, that some soil mass, which would decrease estimated water uptake since crustal material is typically water insoluble, was present in the accumulation mode aerosol during SEAVS. Temporal changes in organic carbon composition, and perhaps water solubility, could cause variability in the modification of ambient aerosol hygroscopic behavior by organic carbon. These effects also contribute to uncertainty in the choice of refractive index, to which the derived results are shown to be sensitive. Finally, the fact that this experiment was not designed to resolve particle size change hysteresis could contribute to scatter in the experimentally derived water uptake results below 80% RH, as well as the observation that experimentally derived water uptake were less than theoretical estimates of water uptake below 80% RH.

Some uncertainty results from variations in ambient aerosol population over the time required for RH cycling. The experimental set up required a time delay between sampling under dry and humidified conditions while the inlet equilibrated to new RH settings. Efforts were made to cycle RH as quickly as possible and to choose sequential dry and humidified aerosol distributions during times when changes in the ambient particle concentration were small. Both the [CN] time line and ambient b_{sp} time line were used in a qualitative manner to determine stability in the aerosol size range of interest to the ASASP-X. However, the variability in ambient dry aerosol volume concentration could not be avoided entirely in derivations of water uptake results. It appears that, of the two

parameters used to determine total water uptake in this work (See Equations 4.3.1 and 4.3.2), the aerosol distribution geometric MMD is least sensitive to ambient fluctuations in the dry aerosol volume concentration. In terms of quantifying total accumulation mode water uptake, the MMD ratio method may be applicable to this study since the accumulation mode aerosol during SEAVS appeared to be internally mixed with homogenous chemistry. In a urban setting, where the aerosol chemistry tends to be more heterogeneous, estimating total water uptake by Equation 4.3.1 may prove to be more reliable.

This work suggests that propagation of uncertainty in experimentally derived R to b_{sp} in a light scattering model is less than 18% for an uncertainty in R less than 10%. However, it is important to recall that uncertainty propagation is a function of the initial aerosol distribution parameters, σ_g and $D_{p,g}$. Thus, the reported propagation of uncertainty in R to simulated b_{sp} may be influenced by the initial aerosol size distribution parameters used in this sensitivity study. The application of RH dependent aerosol size change parameters from this work to light scattering models requires an awareness of the experimental uncertainty in these derived quantities and the degree to which this uncertainty may influence model results.

7. FUTURE WORK

With hindsight, some of aspects of this project's experimental design could be modified to improve results in future field studies of this kind. The time required to properly operate the OPC and RH controlled plenum system were limiting factors in amount of data collected in this experiment. The nephelometer, for example, collected data on a time scale much shorter than the ASASP-X. Therefore the nephelometer was limited in its data acquisition by the relatively slow OPC and plenum RH equilibration time. A solution would be to have two inlet systems, one continuously running at dry RH and the other adjustable to intermediate RH values below water vapor saturation. The OPC and nephelometer could sample alternatively from the two inlets, thereby obtaining better time resolution, while sampling more sequential dry and humidified aerosol, yet still maintaining single instrument integrity in the experiment. This type of inlet would also allow the aerosol to be dried prior to humidification (or vice versa), for a more consistent measurement approach.

Both dry and humidified aerosol volumes reported in this work depend on the initial choices of refractive index used to process the data. Preliminary estimates of dry aerosol refractive indices during SEAVS range from 1.51 to 1.47 (McMurry, personal communication). The partial molar refractive index reconstruction in this work indicates a range of dry aerosol refractive indices during SEAVS of 1.53 to 1.47. Two mean refractive index values for SEAVS were applied to the dry OPC aerosol size distributions in this work, although daily fluctuations in refractive index could be applied to the data.

Preliminary estimates of refractive indices for humidified aerosol during SEAVS were found to be somewhat lower than those used to process humidified aerosol distributions from the ASASP-X data. However, since water uptake is reported here as a ratio of wet to dry diameter, and both wet and dry aerosol sizes would be adjusted upwards upon

reprocessing the distribution data at lower humidities, the actual affect on derived R in this work could be small. Water uptake estimates from this work can be revised based on inversion refractive indices that match temporal variations in the ambient aerosol RH dependent refractive index when a final version of these data become available. An efficient approach to reprocessing the OPC data may be to apply scaling factors to the derived quantities, such as particle diameter or integrated distribution volume, as a function of aerosol refractive index.

In terms of calculating aerosol size distribution statistics, the OPC data could be fit with a distribution function using an appropriate curve fitting algorithm. Size parameters of lognormal distributions, for example, could be used to present both the dry aerosol distribution statistics and water uptake parameterizations. In this report discrete bin data is used to calculate aerosol size distribution parameters.

A main goal of the NPS/CSU special study is to initialize a light scattering model with size distribution data from the ASASP-X and with aerosol chemistry measured during SEAVS. Estimating b_{sp} in this way will allow for a direct comparison of modeled light scattering to experimentally measured RH dependent light scattering from the nephelometer, and will serve as a means to optimize RH dependent model parameterizations that determine light scattering. It is anticipated that aerosol RH dependent size distribution parameters derived from this study can be used to improve the reliability of models currently used to predict optical properties, such as visibility, in the rural southeastern U.S.

REFERENCES

- Active Scattering Aerosol Spectrometer Probe PMS Model ASASP-X Operating Manual, Serial No. 805-0978-10, Particle Measuring Systems, 1977.
- Andrews, E. and Larson S. M., 1993, Effect of surfactant layers on the size changes of aerosol particles as a function of relative humidity, *Environmental Science and Technology*, Vol. 27, No. 5, 857-865.
- Baumgardner, D., 1995, Data processing techniques for the passive cavity aerosol spectrometer probe, US Forest Service/Droplet Measurement Technologies.
- Boucher, O. and Anderson T. L., 1995, General circulation model assessment of the sensitivity of direct climate forcing by anthropogenic sulfate aerosols to aerosol size and chemistry, *Journal of Geophysical Research*, Vol. 100, No. D12, 26117-26134.
- Dick, W., Huang P.-F. and McMurry P. H., 1995, Characterization of 0.02 μm to 1.0 μm particle losses in Permapure dryers: Dependence on size, charge, and relative humidity. Particle Technology Laboratory, Department of Mechanical Engineering, University of Minnesota.
- Fuchs, N. A., 1964, The Mechanics of Aerosols, Pergamon, Oxford.
- Garvey, D. M. and Pinnick R. G., 1983, Response characteristics of the Particle Measuring Systems Active Scattering Aerosol Spectrometer Probe (ASASP-X), *Aerosol Science and Technology*, Vol. 2, 477-488.
- Hand, J. L. and Kreidenweis S. M., 1996, Size corrections based on refractive index for Particle Measuring Systems Active Scattering Aerosol Spectrometer Probe, CIRA report, ISSN.0737-5352-31, Colorado State University.
- Handbook of Chemistry and Physics, 46th Edition, 1965, Editor, Weast R.C., The Chemical Rubber Company, Cleveland, Ohio.

- Hering, S. V. and McMurry P. H., 1991, Optical counter response to monodisperse atmospheric aerosols, *Atmospheric Environment*, Vol. 25A, No. 2, 463-468.
- Hinds, W. C., 1982, Aerosol Technology: Properties, Behavior, and Measurement of Airborne Particles, John Wiley & Sons, New York.
- Kim, Y. J., and Boatman J. F., 1990, Size calibration corrections for the active scattering aerosol spectrometer probe (ASASP-100X), *Aerosol Science and Technology*, Vol. 12, 665-672
- Kreisburg, N., Stolzenburg M. and Hering S., 1996, Differential mobility optical particle size spectrometry measurements of dried and humidified particle size distributions during the Southeastern Aerosol and Visibility Study, Final Report, EPRI Report, Contract No. WO9116-01
- Knutson, E. O. and Liroy P.J., 1982, Measurement and presentation of aerosol size distributions, In Air Sampling Instruments for Evaluation of Atmospheric Contaminants, 7th edition, American Conference of Governmental and Industrial Hygienists, Cincinnati, Ohio
- Malm, W. C. and Kreidenweis S. M., 1996, The effects of aerosol hygroscopicity on the apportionment of extinction, submitted for publication in *Atmospheric Environment*
- Malm, W. C., Sisler J. F., Huffman D., Eldred R. A. and Cahill T. A., 1994, Spatial and seasonal trends in particle concentration and optical extinction in the United States, *Journal of Geophysical Research*, Vol. 99, No. D1, 1347-1370
- Malm, W. C., Golestani Y., Gebhart, K. A., Cahill T. A., Eldred R. A. and Poirot R., 1991, Estimation of the aerosol acidity in the eastern United States, Paper No. 91-89.3, prepared for presentation at the 84th AWMA Meeting, Vancouver, British Columbia, June 16 - 21.
- McMurry, P. H., 1996, Measurements of haze and visual effects, TDMA data report for the Southeastern Aerosol and Visibility Study, Electric Power Research Institute (EPRI).

- Mueller, P. K., Fung K. K., Heisler D., Grosejean D., and Hidy G. M., 1982, Atmospheric particulate carbon observations in urban and rural areas of the United States, in Particulate Carbon-Atmospheric Life Cycle, Plenum, New York.
- Pilinis, C., Pandis S. N. and Seinfeld J. H., 1995, Sensitivity of direct climate forcing by atmospheric aerosols to aerosol size and composition, *Journal of Geophysical Research*, Vol. 100, No. D9, 18739-18754.
- Renfrow, J. R., 1995, Air quality monitoring and research program at Great Smoky National Park: an overview of results and findings, USDI-NPS, GRSM Division of Resource Management and Science.
- Southern Oxidants Study, 1995, Policy-relevant findings in ozone pollution research, 1988-1994, prepared by Chameides W. L. and Cowling E. B., Public outreach document.
- Saxena, P., Hildeman L. M., McMurry P. H. and Seinfeld J. H., 1995, Organics alter hygroscopic behavior of atmospheric particles, *Journal of Geophysical Research*, Vol. 100, No. D9, 18755-18770.
- Saxena, P., and McMurry P. H., 1995, Study Plan: Southeastern Aerosol and Visibility Study, EPRI.
- Seinfeld, J. H., 1986, Atmospheric Chemistry and Physics of Air Pollution. John Wiley & Sons, New York.
- Sherman, D. E., Ames R. B., and Kreidenweis S. M., 1996, Influence of synoptic and local meteorological conditions on ambient total particle concentrations during SEAVS, Paper No. 188, presented at the 13th ACS Rocky Mountain Regional Meeting, Denver Colorado, June 9-12.
- Shettle, E. P. and Fenn R. W., 1979, Models for the Aerosols of the lower atmosphere and the effects of humidity variations on their optical properties, *Environmental Research Paper*, No. 676, AFGL-TR-79-0214.

- Sisler, J. F., Huffman D. and Latimer D. A., 1993, Spatial and Temporal Patterns and the chemical composition of the haze in the United States: an analysis of data from the IMPROVE network, 1988-1991, CIRA report, ISSN.0737-5352-26, Colorado State University.
- Southern Oxidants Study, 1991, University Corporation for Atmospheric Research, Georgia Tech. University, GA, 30303.
- Stelson, A. W., 1990, Urban aerosol refractive index prediction by partial molar approach, Environmental Science and Technology, Vol. 24, No. 11, 1676-1679.
- Tang, I. N. and Munkelwitz H. R., 1994, Water activities, densities and refractive indices of aqueous sulfates and sodium nitrate droplets of atmospheric importance, Journal of Geophysical Research, Vol. 99, No. D9, 18801-18808.
- Tang, I. N. and Munkelwitz H. R., 1991, Simultaneous determination of refractive index and density of an evaporated aqueous solution droplet, Aerosol Science and Technology, Vol. 15, 201-207.
- Tang, I. N., Wong W. T. and Munkelwitz H. R., 1981, The relative importance of atmospheric sulfates and nitrates in visibility reduction, Atmospheric Environment, Vol. 15, No. 12, 2463-2471.
- Tsay, S.-C. and Stephens G. L., 1990, A physical and optical model for atmospheric aerosols with applications to visibility problems, CIRA report, ISSN.0737-5352-16, Colorado State University.
- Willeke, K. and Baron P. A., 1993, Aerosol Measurement: Principles, Techniques and Applications, Van Nostrand Reinhold, New York.

APPENDIX A

Summary of Meteorological and Condensation Nuclei Concentration [CN] Data.

A.1 [CN] Data

Figure A.1.1 is a time line of [CN] data from the CSU operated TSI 3010 CN Counter (Section 3.3.3). The raw data were recorded as instantaneous readings every 40 seconds. The data as plotted are 10 minute averages of the raw data. Note the diurnal patterns in [CN] present in the pre-hurricane period (JD 208 - 213). The diurnal [CN] pattern is interrupted by Hurricane Erin, evident on JD 215. A well defined diurnal [CN] pattern is reestablished during the polluted period (JD 226 - 230).

A.2 Selected Meteorological Data

Figure A.2.1 is a time line of wind direction during SEAVS. The raw meteorological data are 2 minute averages of continuous data and are plotted as 2 minute averages. Notice the diurnal shifts in wind direction during certain meteorological periods. Often, wind is from the south west during the evening and early morning hours, indicating down slope or drainage flow from the Smoky Mountains. In the early afternoon the wind direction often shifts abruptly and is directed from the north, indicative of upslope flow from the Tennessee Valley. Comparison of Figures A.1.1 and A.2.1 show the diurnal [CN] peak is correlated to the upslope flow. The diurnal patterns in both [CN] and wind direction occur when high pressure systems persist over the GRSM area (Sherman *et al.*, 1996). During the hurricane period winds are constant from the southwest and the local meteorology is influenced by large scale synoptic flow. Figure A.2.2 is the ambient RH during SEAVS.

These data are important to the hygroscopicity experiment in this work as it indicates the initial RH of aerosol prior to conditioning in the RH controlled inlet.

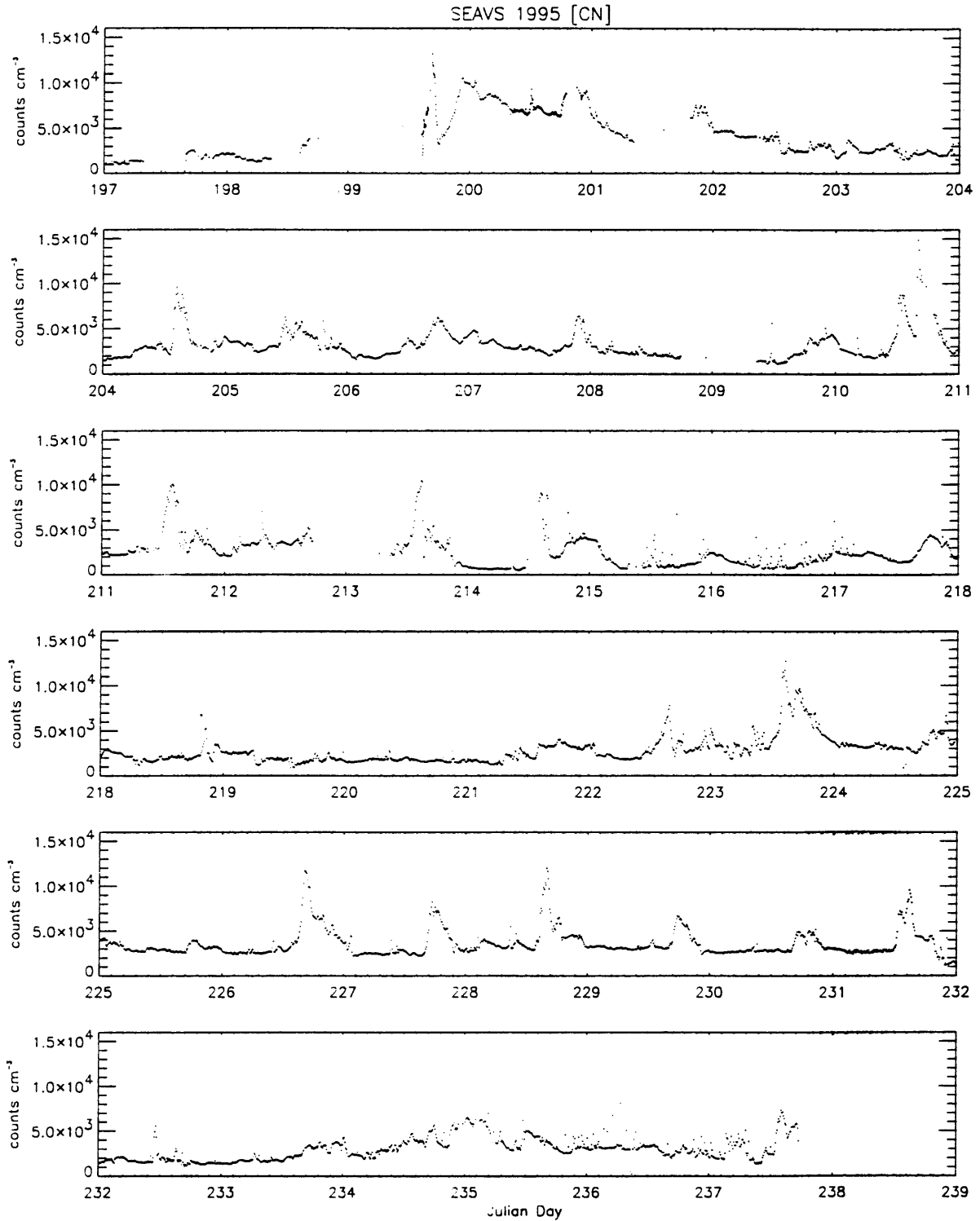


Figure A.1.1. [CN] time line during SEAVS with each point representing a 10 minute average of the raw data.

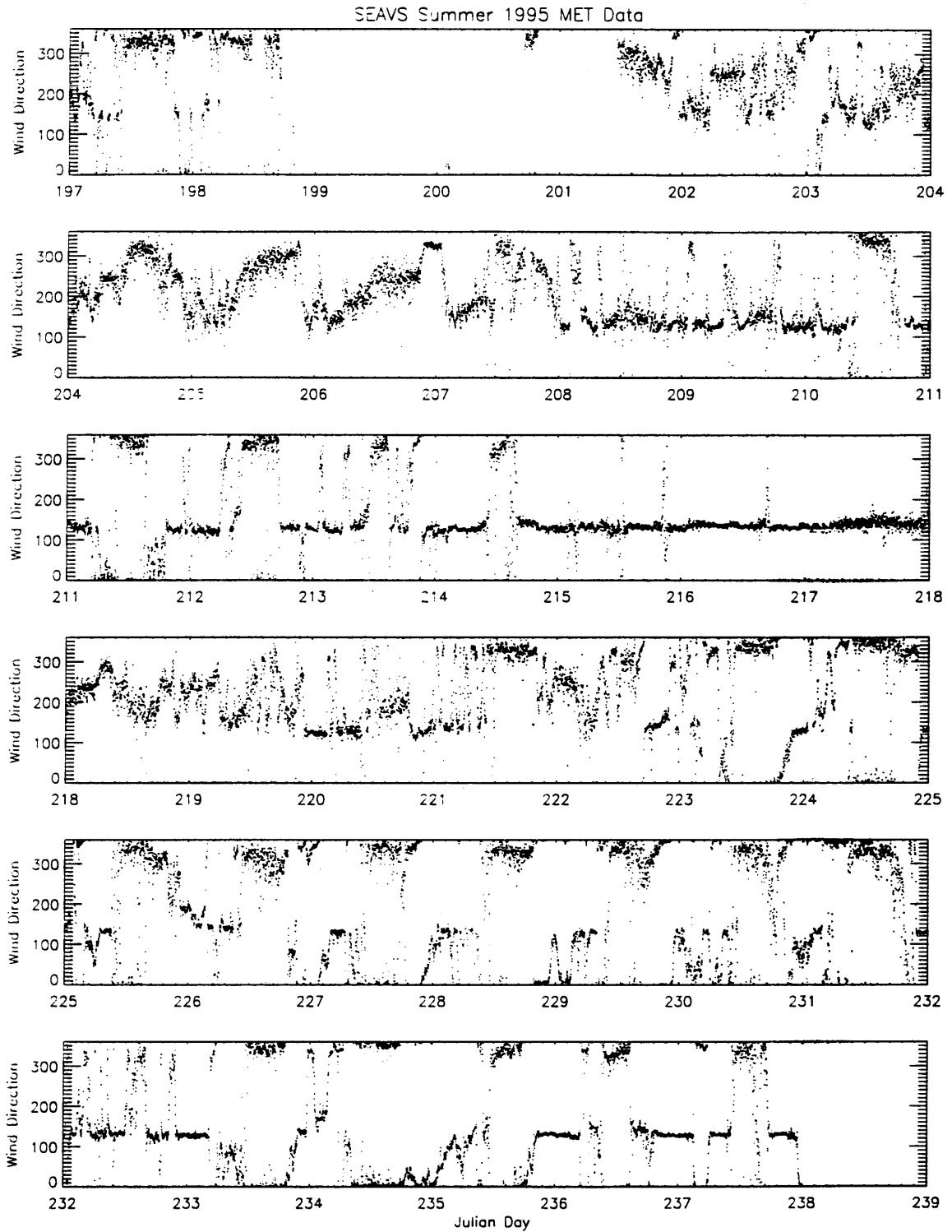


Figure A.2.1. Wind direction time line during SEAVS. The readings were taken from the same instrument shed as the [CN] data and are shown as two minute averages.

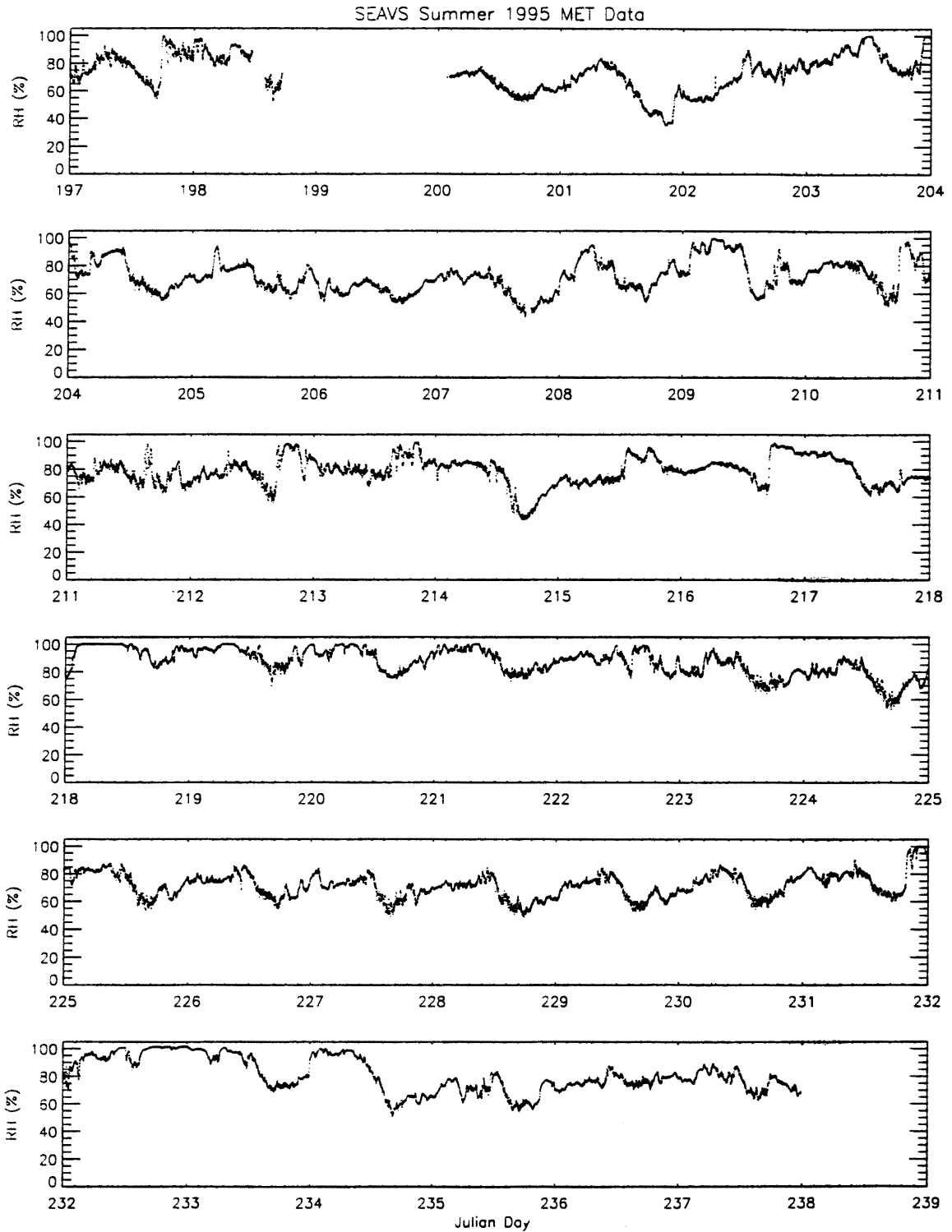


Figure A.2.2. Ambient RH time line during SEAVS. Measurements were taken at three locations at the sampling site and are shown as an average of the three readings with two minute resolution.

A.3 Selected Chemical Data

Plots shown in section A.3 show 12 hour averaged data from the IMPROVE filter samplers during SEAVS. Details on the respective analytical methods mentioned in this Section are available in Sisler *et al.* (1993) and Malm *et al.*, (1994).

Figure A.3.1 is the gravimetric fine mass concentration measured during SEAVS. Superimposed on this figure is the sum of sulfate, organic and soil fine mass, the predominant chemical fractions observed during SEAVS, measured by chemical techniques described below. The excess gravimetric mass over chemical mass is presumed to be associated water, since the gravimetric measurements were made in a laboratory with ambient RH near 50%.

Figure A.3.2 shows the combined airborne mass concentration ($\mu\text{g m}^{-3}$ air) of sulfate and ammonium ions as measured by ion chromatography (IC). The sum of the 12 hour average mass concentrations of sulfate and ammonium ions during SEAVS is $913 \mu\text{g m}^{-3}$, which is comparable to the mass of reconstructed ammonium bisulfate, or $\text{SO}_4 \times 1.19$, which gives a similar sum of 12 hour averaged mass concentration of $915 \mu\text{g m}^{-3}$.

Figure A.3.3 shows organic carbon fine mass concentration as measured by thermal optical reflectance (TOR). The reported mass concentration is the sum of five thermal gradient CO_2 evolution steps and is expressed in terms of equivalent hydrocarbon mass by applying the mass conversion factor shown in Table A.3.1. A blank correction of $0.597 \mu\text{g m}^{-3}$ has been added to the organic carbon mass concentrations (Day, personal communication).

Figure A.3.4 shows the airborne mass concentration of selected lithophilic compounds, or the soil mass fraction. Soil is represented here as the combined mass of Al, Si, Fe, Ca, and Mg converted to their common oxides. Elemental concentrations are from

particle-induced x-ray emissions spectroscopy (PIXE). The soil components, their representative oxides, and equivalent mass conversion factors are given in Table A.3.1.

Measured Compound	Representative Complex	Equivalent Mass Factor
SO ₄ ²⁻	SO ₄ ²⁻	1
NH ₄ ⁺	NH ₄ ⁺	1
Al	Al ₂ O ₃	1.90
Si	SiO ₂	2.14
Fe	Fe ₃ O ₄	1.38
Ca	CaO	1.40
Mg	MgO	1.60
O ₁ +O ₂ +O ₃ +O ₄ +O _p	average organic hydrocarbon	1.40
EC	elemental carbon	1

Table A.3.1. Chemical compounds and equivalent mass conversion factors used to calculate dry chemical mass and chemical mass fractions for this work. Chemical data is from the IMPROVE samplers.

Figure A.3.5 is the elemental carbon measured by TOR. This figure is included to illustrate that while the contribution of light absorbing species to the particle mass concentration during SEAVS small, it cannot be neglected. However, the small amount of elemental carbon serves to justify in part the omission of the imaginary component of refractive index in the data analysis used in this work. It should be pointed out that soils can contribute to light absorption, although to a lesser degree than elemental carbon.

Figure A.3.6 shows the combined mass of nitrate and nitrite anions measured by IC. Nitrate complexes, such as ammonium nitrate, are commonly observed in atmospheric aerosols, although more typically in urban settings. The unimportance of nitrate compounds during SEAVS is clearly illustrated by their low mass concentrations, as compared with those in Figures A.3.2 through A.3.4.

Figure A.3.7 shows the chloride anion mass concentration, the likely chemical signature of a maritime air mass. The chloride peak near JD 215 is associated with synoptic flow from Hurricane Erin which began to influence the SEAVS site at that time. The contribution of chloride to total mass concentration during SEAVS is insignificant.

Figure A.3.8 is the molar ratio of ammonium to sulfate ions. This figure can be interpreted as sulfate aerosol acidity, provided available sulfate anions are associated only with ammonium or hydrogen, which is a good assumption for rural southeastern aerosol where sulfate dominates the ionic mass fraction. Figure A.3.8 indicates an average particle acidity corresponding to ammonium bisulfate, or a 1:1 ammonium to sulfate molar ratio. During the polluted period the aerosol appears more acidic, with sulfate acidity between that of ammonium bisulfate and sulfuric acid. However, if chemical species other than sulfate and ammonium dominate the aerosol chemistry, interpreting Figure A.3.8 as particle acidity is not necessarily correct. For example, on JD 215 particle acidity appears to increase abruptly. This trend is coincident with the onset of an air mass strongly influenced by Hurricane Erin. If ammonia was limited during the hurricane flow, available sulfate ions may have combined with maritime cations, resulting in an ion balance that may have been not acidic.

Figure A.3.1. SEAVS IMPROVE Gravimetric Fine Mass

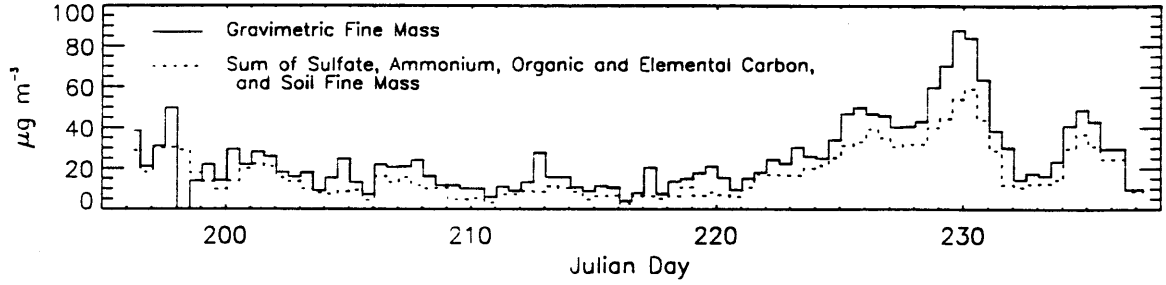


Figure A.3.2. SEAVS IMPROVE Sulfate plus Ammonium Fine Mass

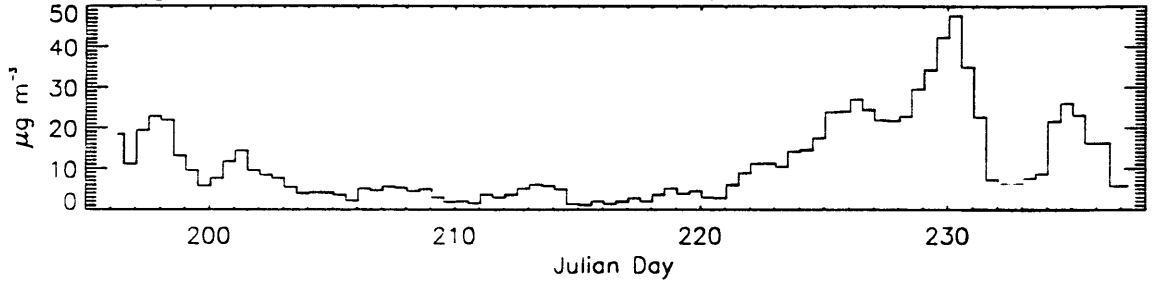


Figure A.3.3. SEAVS IMPROVE Organic Carbon Fine Mass

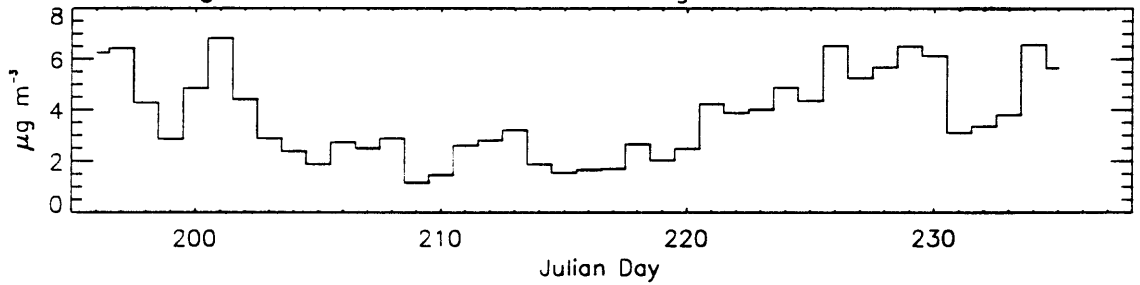
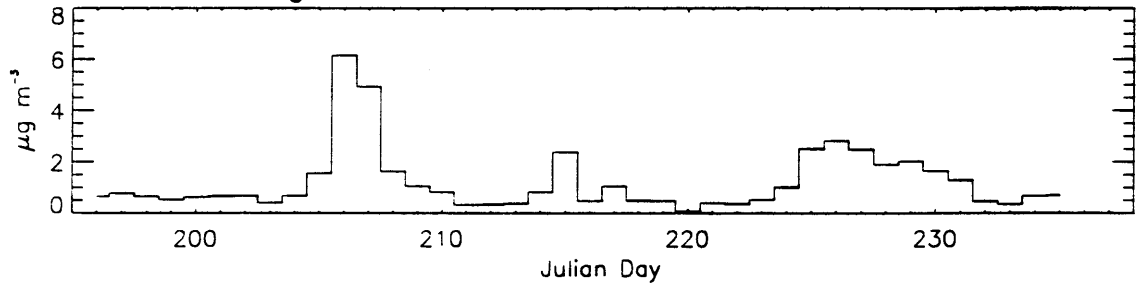


Figure A.3.4. SEAVS IMPROVE Soil Fine Mass



Figures A.3.1 to A.3.4. Data from the IMPROVE samplers during SEAVS for gravimetric fine mass, and combined sulfate and ammonium fine mass averaged over 12 hour intervals. Organic carbon and soil fine mass are shown as 24 hour averages.

Figure A.3.5. SEAVS IMPROVE Elemental Carbon

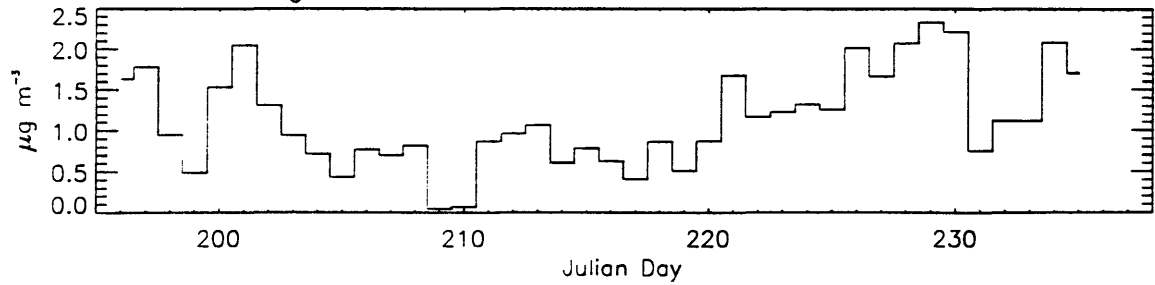


Figure A.3.6. SEAVS IMPROVE Nitrate + Nitrite

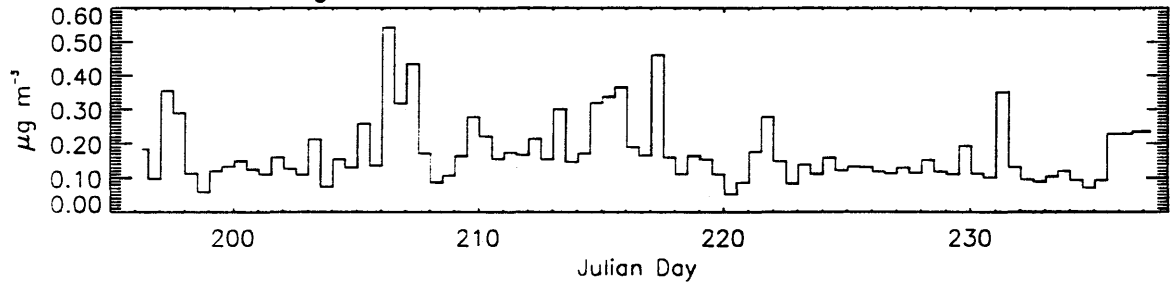


Figure A.3.7. SEAVS IMPROVE [Cl⁻]

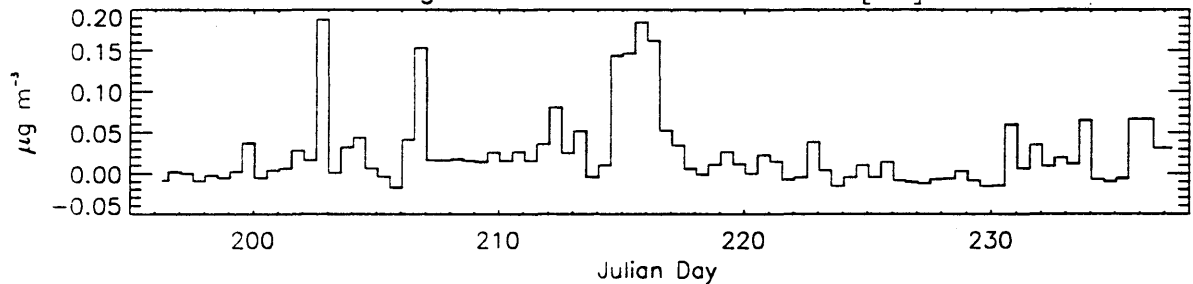
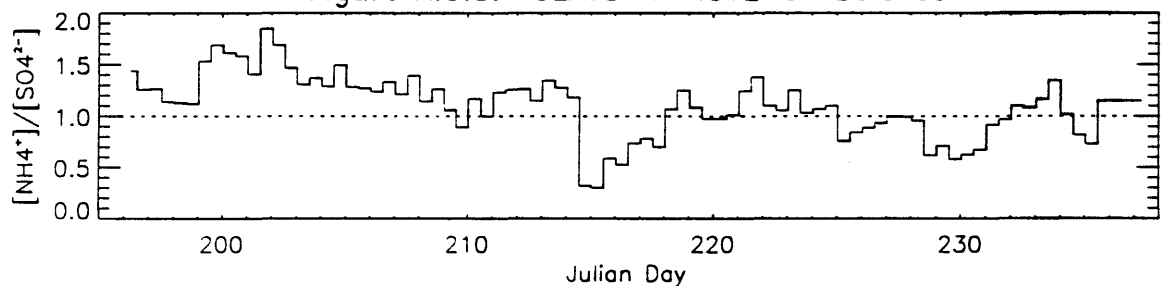


Figure A.3.8. SEAVS IMPROVE Ion Balance



Figures A.3.5 to A.3.8. Data from the IMPROVE samplers during SEAVS for elemental carbon fine mass as 24 hour averages. Combined nitrate and nitrite, and chloride ion fine mass are shown as 12 hour averages. Molar ratios of ammonium to sulfate ions are shown as an index of particle acidity with the one to one dotted line corresponding to ammonium bisulfate.

A.4 Hurricane Erin Images

Figures in Section A.4 are satellite images of Hurricane Erin in visible spectral bands. These figures show storm bands and high level cumulus associated with this large scale synoptic feature. The first image, Figure A.4.1, is from JD 215, the first day that Hurricane Erin strongly influenced meteorology during SEAVS. The second image, Figure A.4.2, from JD 216, shows Hurricane Erin dissipating over the southeastern U.S., although still having a strong influencing on the region's meteorology.

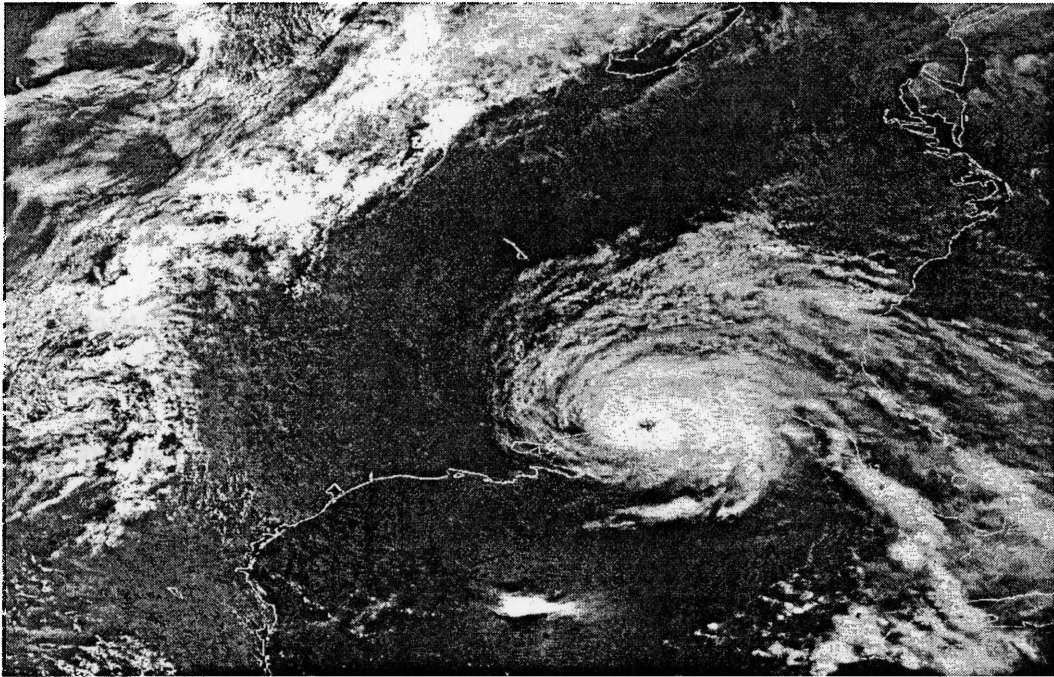


Figure A.4.1. Land fall of Hurricane Erin at Pensacola Florida, 08/03/95, JD 215. This and the following figure illustrate the influence of this large scale synoptic system on the southeast U.S. during SEAVS.

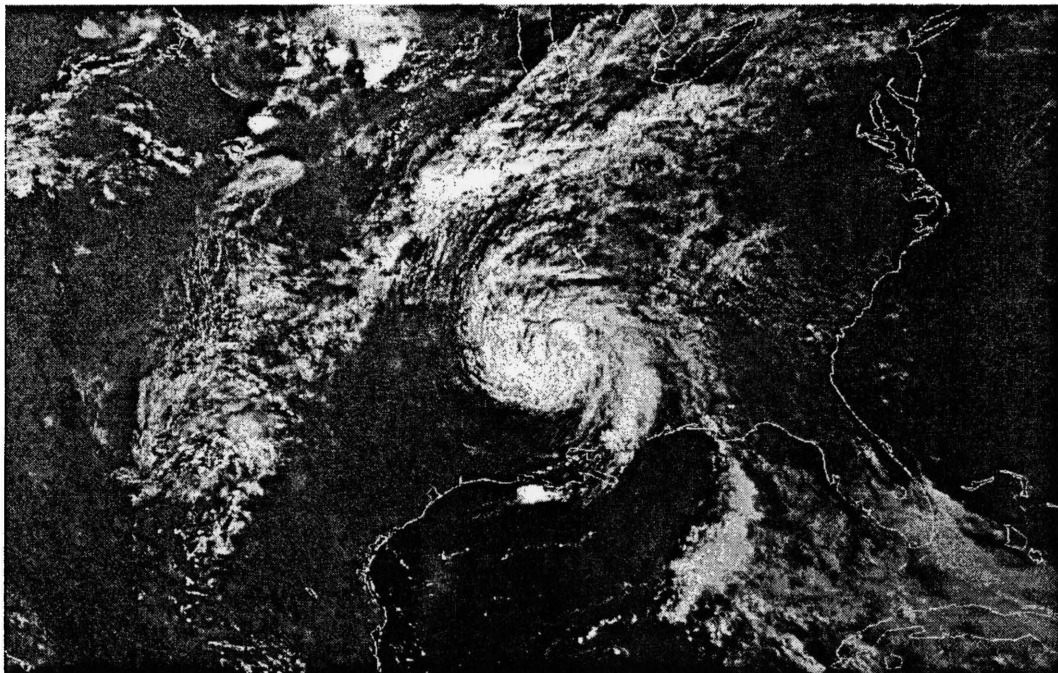


Figure A.4.2. Dissipation of Hurricane Erin over the Southeastern US, 08/04/95, JD 216.

APPENDIX B

Optical Particle Counter Calibration

B1. Field Calibration

Monodisperse polystyrene latex (PSL) spheres were sampled daily to check OPC sizing performance and to ensure proper aerodynamic focusing and alignment of the sample stream in the OPC laser cavity. Generally, PSL spheres with D_p of 0.41 μm were measured and size distributions for these calibration particles recorded. PSL spheres with D_p of 0.19 and 0.25 μm were also measured in the field.

Figure B.1.1 is a schematic of the ASASP-X optics and sample inlet flow across the laser beam. Proper alignment of the sample stream is fundamental to particle sizing performance of the OPC. The sample inlet on the ASASP-X that connects to the laser cavity is fitted with spring loaded horizontal and axial adjustment screws which allow the sample stream to be positioned in the center of the laser beam to optimize the intensity of scattered light from sampled particles. Since the nature of the experiment required the ASASP-X inlet to be attached to a plenum, particular care was taken to set up an inlet for the OPC that could be easily adjusted yet remain undisturbed while switching flows from calibration particles to the aerosol inlet.

Sample flow was focused by setting an initial sheath to sample flow ratio of approximately 20:1. Further refinement of the sample to sheath flow balance was made while sampling PSL spheres by adjusting the respective flows until a sharp peak was observed. Some representative field calibration PSL size distributions and their distribution statistics are included in Figure B.1.1 Table B.1 gives grand averages of the field PSL distribution statistics.

PSL Diameter	D_{pg} (μm)	std. deviation (μm)	δD_{pg}	n
0.41	0.423	0.0223	5%	27
0.25	0.222	0.0074	3%	3
0.19	0.203	0.0063	3%	4

Table B.1.1. Averaged field PSL number distribution statistics measured by the ASASP-X during SEAVS. δD_{pg} represents the percent uncertainty in the measured PSL size based on one standard deviation.

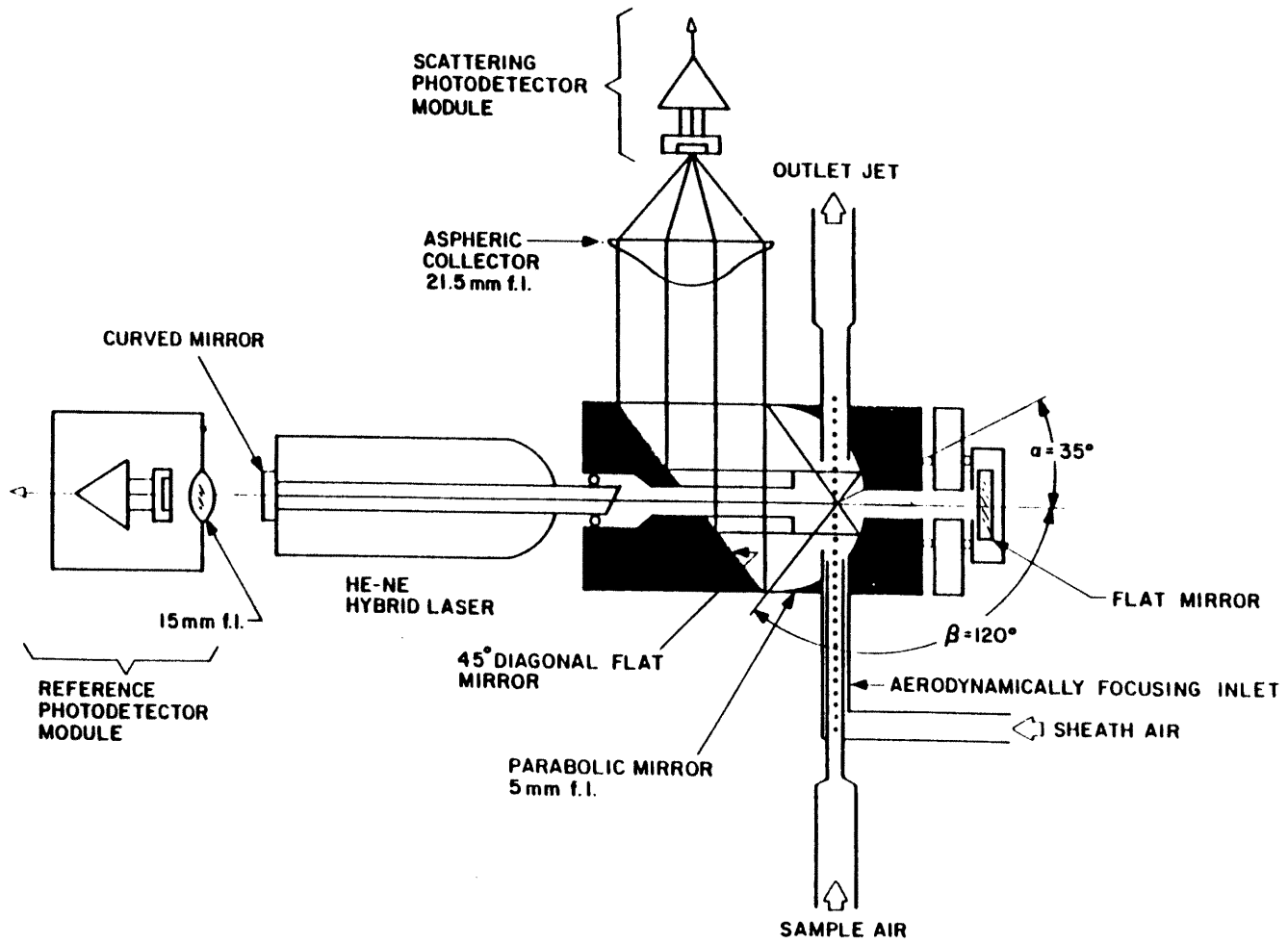


Figure B.1.1. Schematic of the ASASP-X optics and sample inlet flow.

B.2. ASASP-X Post Experiment Calibration

The electronics which the instrument uses to classify particles into size channels were tested in the lab after the SEAVS experiment. Instrument response curves were determined in terms of voltage versus channel number, and experimentally determined response values were compared to calibrations given by the manufacturer. Two methods of determining instrument response were investigated, and results from these experiments are presented in this section.

In the first method (Experiment I) the PHA voltages were measured directly on the channel voltage comparators with an applied -10V reference voltage. In the second method (Experiment II) an AC square wave was fed into the OPC after the photodiode module. In this experiment, 'mock counts' were generated by regulating current frequency, and particles of different sizes were simulated by varying the amplitude of the input square wave. Channel voltages obtained from Experiment II were ultimately used in the ASASP-X calibration. In both experiments voltages were normalized relative to an instrument reference voltage of -10V.

I. Pulse Height Analyzer (PHA) Boards PMS-402 Voltage Measurement (10/04/95).

The ASASP-X has four PMS-402 boards corresponding to channels 1-4, 5-8, 9-12, and 13-16, respectively. In this test, an external -10V DC reference voltage was supplied with all four PHA boards in place. Voltage input and measuring devices were grounded to the ASASP-X common at pin 22 on slot 1 (PMS-415). The instrument reference voltage was bypassed. Individual PHA boards were placed on an extender card and the voltage across the resistor bank for each PHA channel was read at pin 2A of the MC14066 voltage comparator for each channel, A1 to A4, on the respective PMS-402 boards. Channel voltages corresponding to the four amplification ranges were measured, giving 16 voltage readings per board, or 64 discrete voltage thresholds overall. The PHA board for channels 13 to 16

has no range selector for bin 16 and the voltage measured at this channel comparator is the reference voltage.

PHA threshold voltages obtained from this experiment agreed closely those determined by the manufacturer. The only significant deviation was a +13% discrepancy in the upper voltage threshold for channel 8 in range 3.

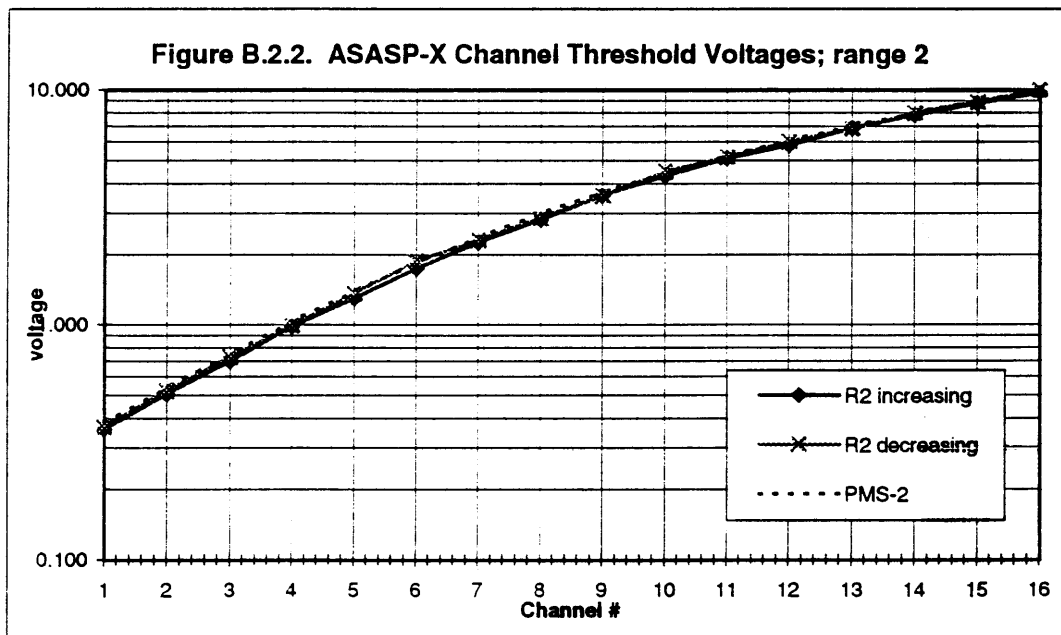
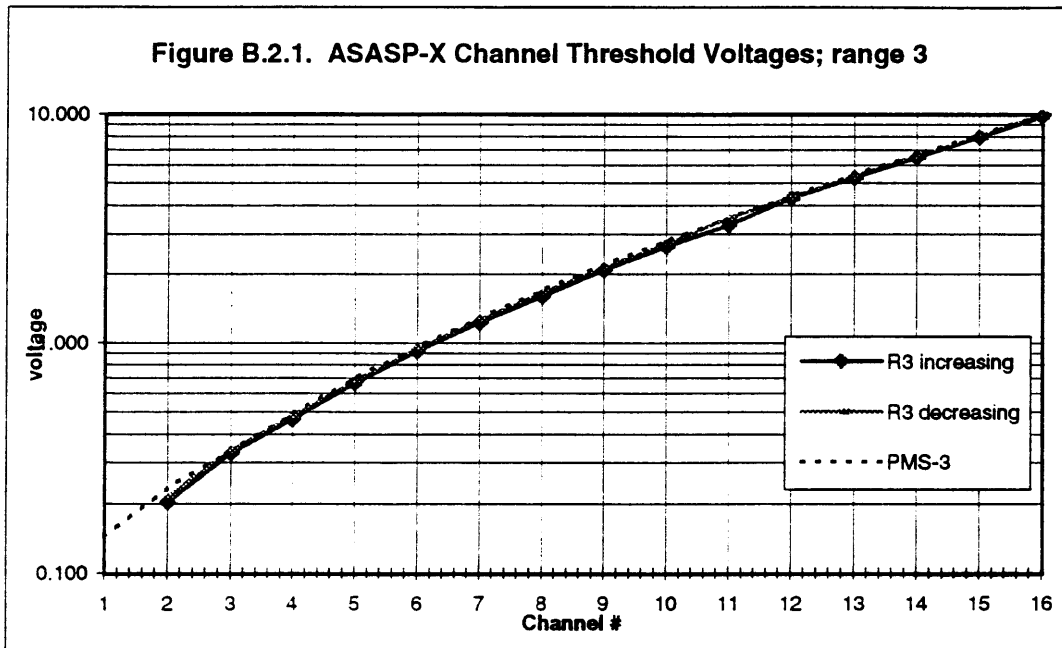
II. Mock Photo Detector Input to PHA Boards (12/18/95)

Output from the ASASP-X photodetector module feeds into board PMS-415 at pin 6. With the baseline restoration module removed, a 100 Hz square wave from a HP 3300A Function Generator was substituted for the photodetector input. A potentiometer in line allowed fine tuning of the square wave amplitude, although was set at its maximum opening (least resistance) except while measuring the lower channel voltages in amplification range 3. Input voltage was determined by measuring the negative peak amplitude from the function generator at pin 6 on slot 1 (PMS-415) with a referencing oscilloscope. The ASASP-X optics were cleaned prior to this experiment and the instrument reference voltage was -7.6V, as measured at pin 19 on board PMS-430. Input and measuring devices were grounded to the ASASP-X common at pin 22 on slot 1 (PMS-415).

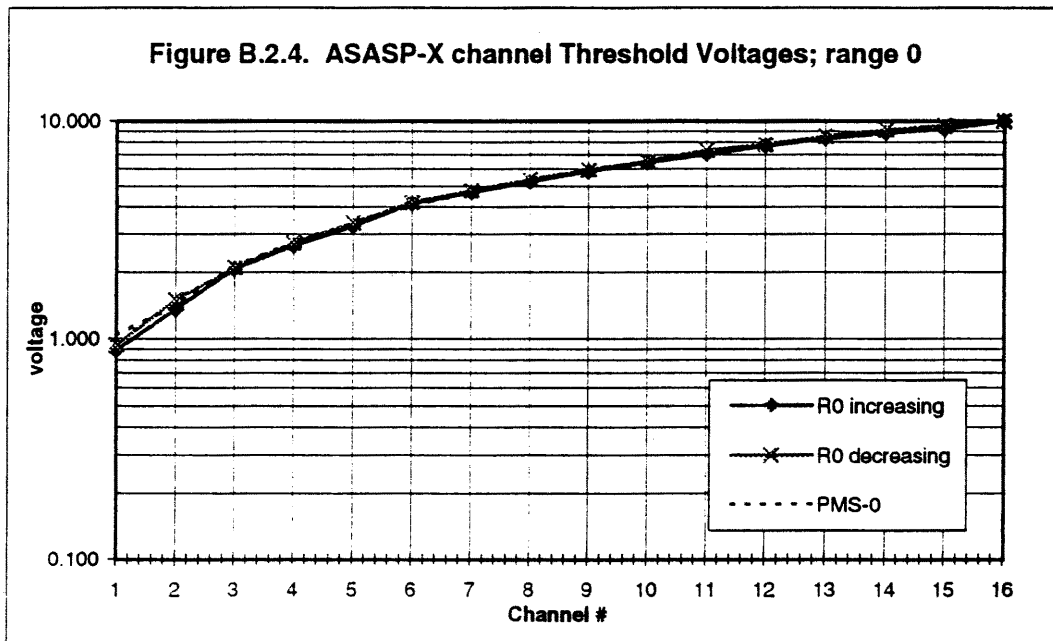
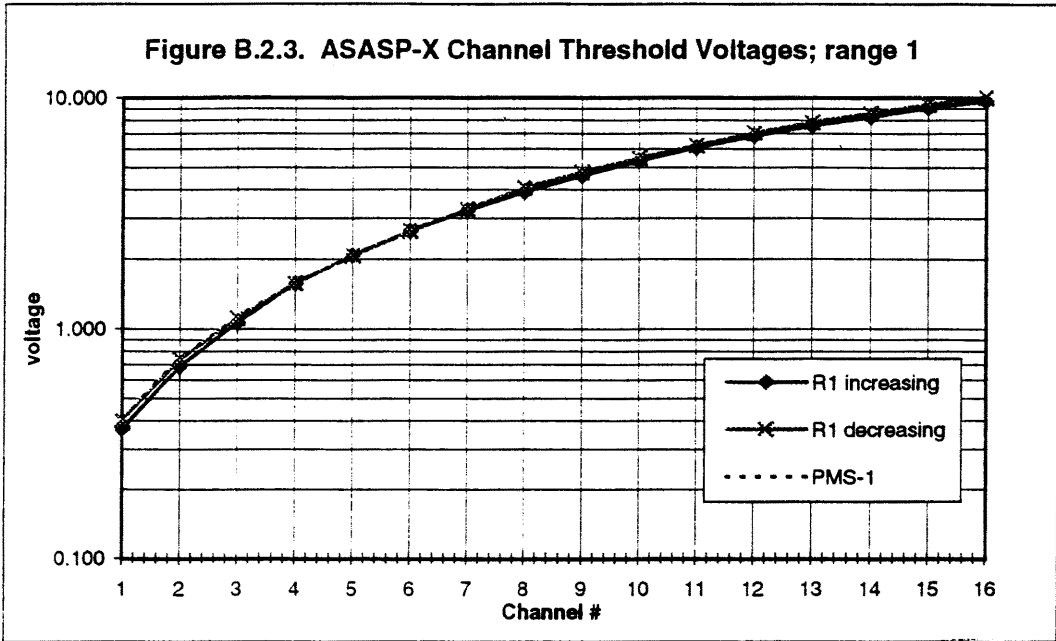
Channel threshold voltages were recorded by gradually increasing peak amplitude on the function generator until the mock counts displayed by the Spec 1D interface appeared in the adjacent channel. For example, with the ASASP-X set to amplification range 3, with an input peak amplitude of 1.4 V, counts appeared in channel 7. As peak amplitude was increased, counts remained in channel 7 until a peak amplitude of 1.77 V, at which point counts appeared in channel 8. Therefore, 1.77 V is the lower threshold voltage for channel 8. All measured voltages were normalized to the instrument reference voltage, measured continuously throughout the experiment by a Fluke volt meter (and periodically on a separate oscilloscope channel) to ensure the instrument reference voltage did not drift during the experiment. Threshold voltages were also measured by gradually decreasing the input

voltage to ensure reproducibility of the experiment. PHA curves from experiment II are included as Figures B.2.1 to B.2.4. Voltage thresholds obtained while increasing the input voltage are shown as the increasing voltage curve, whereas threshold voltages obtained while decreasing the input voltage are shown as the decreasing voltage curve. Channel threshold voltages given in the instrument manual are shown as the dotted line.

Generally, this experiment reproduced the manufacturer's channel threshold voltages closely and the experimentally determined channel voltages themselves were reproducible. Some discrepancies from the manufacturer's values were observed, however. Most notably, channel 1 threshold voltages in range 3 could not be measured at all due to significant electronic noise. Often, data from the ASASP-X had anomalously high counts in this high amplification channel. Based on the post calibration results, channels 1 and 2 in amplification range 3 were discarded from the data. Also observed in this experiment, the upper threshold voltage for channel 10 in amplification range 3 was 9% lower than the manufacturer's reported voltage when the channel transition was approached from lower voltages, although when the channel transition was approached from higher voltages, the threshold voltage was within 2% of the manufacturer's reported voltage. A similar effect was observed for the upper threshold voltage of channel 5 in amplification range 2. This 'mush' in two of the threshold voltage readings may have been related to apparently high counts observed in channel 10 of amplification range 3 in the data. In the final analysis of the data, channels in ranges 3 and 2 were lumped together in groups of two or three channels to accommodate experimental uncertainty in the true threshold voltages. The lumping scheme is described in detail in Appendix C. ASASP-X channel transition voltages obtained from this experiment, while increasing from lower to higher input peak amplitude, were used for the channel threshold voltages and subsequent determinations of channel threshold response in the final instrument calibration.



Figures B.2.1 and B.2.2. ASASP-X Channel threshold voltages for PHA amplification ranges 3 and 2. Experimental values obtained while increasing the input voltage and while decreasing input voltage are shown with the voltages listed in the instrument operating manual.



Figures B.2.3 and B.2.4. ASASP-X Channel threshold voltages for PHA amplification ranges 1 and 0. Experimental values obtained while increasing the input voltage and while decreasing input voltage are shown with the voltages listed in the instrument operating manual.

B.3 Establishing Unique Instrument Calibration Constants

With the relationship between channel and voltage established, the next step was to determine the relationship between particle scattering intensity and channel threshold voltage. This is the same as the particle size and voltage relationship if the particle refractive index is known. Therefore, calibration of an OPC requires a source of nearly monodisperse particles of known size and refractive index.

Six different PSL sphere sizes, 0.19 μm , 0.25 μm , 0.30 μm , 0.41 μm , 0.47 μm and 0.87 μm , supplied by Interfacial Dynamics Corporation, were used to calibrate the ASASP-X in this work. PSL spheres were atomized from a dilute aqueous suspension and were passed through a drier and Differential Mobility Analyzer (DMA) prior to sampling by the ASASP-X. PSL spheres passed through a DMA were found to have a sharper peak than spheres directly from the atomizer, although the ASASP-X channel with maximum counts did not change provided the DMA was set to the appropriate mobility corresponding to PSL size.

By observing the channel in which the maximum counts for a given PSL size occurred, a relationship between particle diameter and channel threshold voltages was obtained. Since an upper and lower threshold voltage span a given PHA channel, the relationship between channel voltage and PSL size channel is the range from lower to upper channel threshold voltages. Figure B.3.1 shows data from the ASASP-X for some calibration PSLs and the channel with maximum counts is apparent.

Calibration constants derived for each of the four amplification ranges are shown in Table B.3.1 with corresponding constants from Garvey and Pinnick (1983) derived for a similar OPC. Our calibration constants were obtained by dividing respective bin threshold voltages by the Mie scattering cross section, obtained from Mie scattering calculations for

the respective PSL sphere diameter and refractive index of 1.580 - 0i. Since more than one calibration constant was derived for each amplification range, the values shown in Table B.3.1 represent averages of all experimentally derived constants for a given range.

The calibration constants in Table B.3.1 allow the ASASP-X channels to be defined in terms of theoretical scattering response (TR) rather than voltage. In order to determine the particle size that corresponds to each channel threshold TR one need only generate a Mie scattering curve for the component refractive index of interest and match TR to particle diameter.

ASASP-X Range	Calibration Constants (V cm ⁻²)	Garvey and Pinnick, 1983 (V cm ⁻²)
0	1.65×10^8	1.9×10^8
1	6.63×10^8	1.2×10^9
2	8.45×10^9	1.3×10^{10}
3	5.64×10^{10}	8.4×10^{10}

Table B.3.1 A comparison of ASASP-X calibration constants from this study to similar constants based on the calibration constant and relative gains from Garvey and Pinnick (1983).

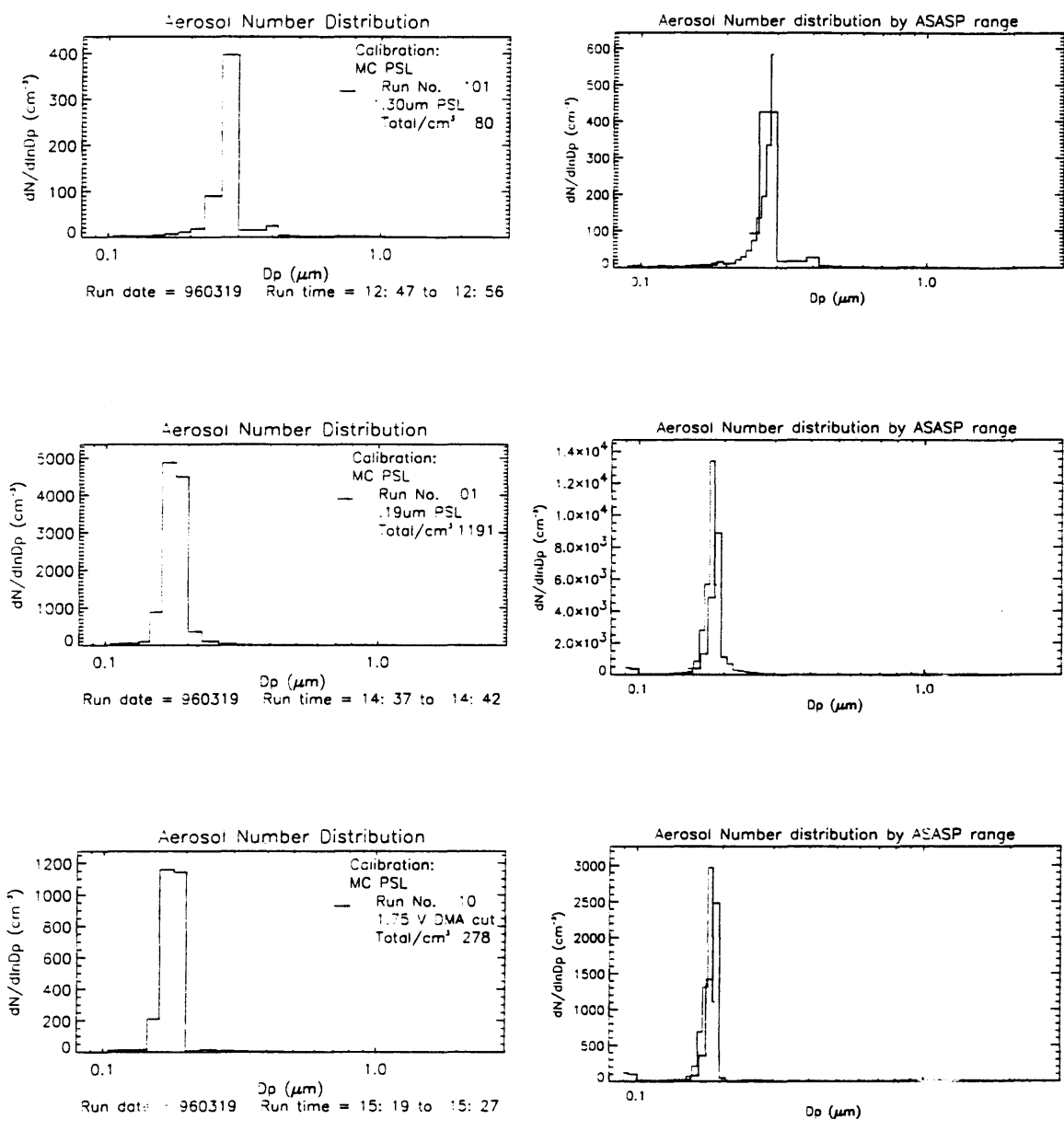


Figure B.3.1 a-c. Number distributions for some PSL calibrations used in this work. The left hand column is plotted as bins described in Table C.1.2. The right hand column shows distributions using the PHA channels. Note the separate lines corresponding to adjacent amplification ranges in the right hand column. The first row (a) shows 0.3 μm PSLs. The second row (b) shows 0.19 μm PSLs. The third row (c) are 0.19 μm PSL which have been passed through a DMA.

APPENDIX C

Optical Particle Counter Data Reduction

C.1 ASASP-X Data Inversion Using Scattering Response Functions from Mie Theory

The ASASP-X channels were defined in terms of theoretical scattering cross section by the method explained in Appendix B. At this point it is possible to define the ASASP-X channels in terms of particle size for aerosol with refractive indices different than the calibration PSLs. It is important to apply size corrections to the ASASP-X data since the refractive index of ambient aerosols is generally different than the refractive index used in the calibration. Furthermore, the refractive indices of a hygroscopic aerosol will approach a limit of $n = 1.33$, the refractive index of water, as saturation ambient RH is approached. Since the nature of this experiment was to determine the RH dependence of ambient aerosol size distribution parameters, RH dependent refractive index corrections are applied to the data.

The ambient aerosol indices of refraction used to process the ASASP-X data set are shown in Table C.1.1. These values are adopted from light scattering model parameterizations for rural aerosol with chemical composition similar to that encountered during SEAVS (Shettle and Fenn, 1979). For the purposes of this work only the real component of the complex index of refraction is considered. The imaginary component, which accounts for light absorption, is ignored based on the relatively low amounts of light absorbing compounds measured during SEAVS (See Appendix A.1). Refractive index values denoted with asterisks in Table C.1.1 were derived from a linear interpolation of real refractive index values from Shettle and Fenn rural aerosol model for particle refractive indices corresponding to 70, 80, 90, and 99% RH.

Relative Humidity	n Rural Aerosol Model	n (Re) This Study	Application of n to experimental data as $f(\text{RH})$
Dry	1.530-.00660i	1.530	40% > RH
RH = 50 %	1.520-.00626i	1.520	40% < RH < 60%
RH = 70 %	1.501-.00560i	1.501	60% < RH < 73%
RH = 75 %		1.469 *	73% < RH < 77%
RH = 80 %	1.443-.00370i	1.443	77% < RH < 83%
RH = 85 %		1.420 *	83% < RH

Table C.1.1 RH dependent refractive index, n , from the Rural Aerosol Model (Shettle and Fenn, 1979) and real component of refractive indices used to process ASASP-X data in this study. Asterisks indicate interpolated values. Also shown are the criteria used for applying a given refractive index to experimental data as a function of RH.

Figure C.1.1 shows the ASASP-X calibrated channels for two refractive indices, corresponding to ‘dry’ and RH of 85%. Note that the theoretical Mie scattering intensity generally increases with particle diameter. As was mentioned in Section 2.3, the dependence of scattering intensity on particle size represents the basic theory for OPC operation. However, as can be seen from Figure C.1.1, the Mie scattering curves becomes a multi-valued function of particle diameter above D_p of approximately 0.4 μm .

There are several approaches to calibrate an OPC in the multi-valued region of the Mie curve. A common method is to fit the Mie curve corresponding to a given index of refraction with a polynomial function, thereby obtaining a relation that gives D_p as function of instrument response (Kim and Boatman, 1990). Alternatively, channel diameter limits can be taken directly from the Mie curve where the calibrated channel threshold response matches the theoretical response, or a Mie to Mie curve fit. (Hand and Kreidenweis, 1996).

of instrument response (Kim and Boatman, 1990). Alternatively, channel diameter limits can be taken directly from the Mie curve where the calibrated channel threshold response matches the theoretical response, or a Mie to Mie curve fit. (Hand and Kreidenweis, 1996). However, the latter approach cannot be applied rigorously in multi-valued regions of the Mie curve. The index of refraction corrections in this work use a Mie to Mie curve fit in the linear portion of the scattering curve (below approximately $0.4 \mu\text{m}$) and smooth through the multi-valued regions. Note the magnitude of diameter shift for one particle size after the refractive index correction is applied (Figure C.1.1).

Table C.1.2 shows the index of refraction corrected bin diameters used in this study. For $D_p > 1.0 \mu\text{m}$ the bin diameter limits revert to the manufacturer's diameter limits (ASASP-X operating manual), based on the assumption that particles larger than $1 \mu\text{m}$ do not necessarily have the same hygroscopicity, and therefore the same RH dependence in refractive index, as accumulation mode aerosol. Also, the Mie resonances at larger particle sizes make it difficult to define refractive index based corrections for those sizes. In any case, the data interpretation in this work has been restricted largely to accumulation mode aerosol, rendering size corrections to particles larger than the accumulation mode cut off unimportant.

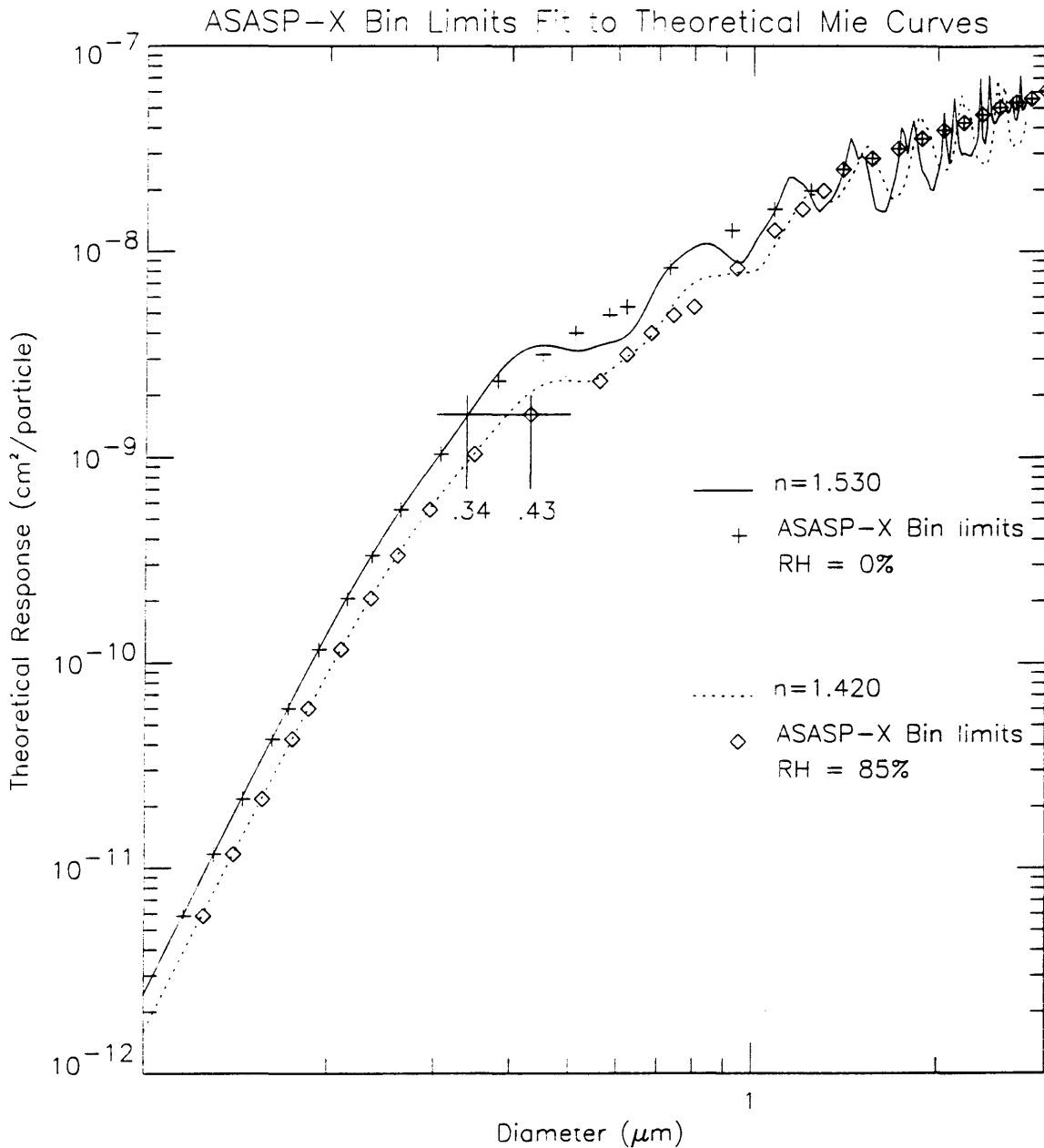


Figure C.1.1. Mie scattering curves for two data inversion refractive indices used in this report corresponding to ambient aerosol with RH of 0 and 85%. The ASASP-X bin diameters that correspond to the Mie curves are superimposed. An example of the refractive index induced size shift for equivalent scattering response at the two RH values is indicated.

Bin #	Response cm ² /particle	Dry n=1.530 Dp (μm):	RH =50% n=1.520	70% n=1.501	75% n=1.469	80% n=1.443	85% n=1.420
1	5.845E-12	0.116	0.117	0.118	0.121	0.123	0.125
2	1.171E-11	0.13	0.131	0.133	0.135	0.138	0.14
3	2.174E-11	0.145	0.146	0.147	0.15	0.153	0.156
4	4.269E-11	0.162	0.163	0.165	0.169	0.172	0.175
5	5.998E-11	0.172	0.173	0.175	0.179	0.183	0.186
6	1.162E-10	0.193	0.195	0.197	0.202	0.206	0.21
7	2.053E-10	0.215	0.216	0.219	0.225	0.23	0.235
8	3.323E-10	0.236	0.238	0.241	0.248	0.254	0.26
9	5.545E-10	0.263	0.266	0.27	0.278	0.286	0.294
10	1.035E-09	0.306	0.31	0.316	0.326	0.338	0.348
11	1.608E-09	0.338	0.344	0.36	0.38	0.41	0.44
12	2.336E-09	0.38	0.39	0.44	0.47	0.51	0.55
13	3.142E-09	0.45	0.46	0.50	0.53	0.57	0.61
14	3.993E-09	0.51	0.52	0.57	0.61	0.65	0.69
15	4.880E-09	0.58	0.59	0.63	0.66	0.70	0.74
16	5.360E-09	0.62	0.63	0.68	0.72	0.76	0.80
17	8.270E-09	0.73	0.74	0.81	0.84	0.87	0.90
18	1.260E-08	0.92	0.93	0.95	0.96	0.97	0.98
19	1.600E-08	<i>1.08</i>	<i>1.08</i>	<i>1.08</i>	<i>1.08</i>	<i>1.08</i>	<i>1.08</i>
20	1.970E-08	<i>1.24</i>	<i>1.24</i>	<i>1.24</i>	<i>1.24</i>	<i>1.24</i>	<i>1.24</i>
21	2.500E-08	<i>1.40</i>	<i>1.40</i>	<i>1.40</i>	<i>1.40</i>	<i>1.40</i>	<i>1.40</i>
22	2.830E-08	<i>1.56</i>	<i>1.56</i>	<i>1.56</i>	<i>1.56</i>	<i>1.56</i>	<i>1.56</i>
23	3.160E-08	<i>1.72</i>	<i>1.72</i>	<i>1.72</i>	<i>1.72</i>	<i>1.72</i>	<i>1.72</i>
24	3.540E-08	<i>1.88</i>	<i>1.88</i>	<i>1.88</i>	<i>1.88</i>	<i>1.88</i>	<i>1.88</i>
25	3.910E-08	<i>2.04</i>	<i>2.04</i>	<i>2.04</i>	<i>2.04</i>	<i>2.04</i>	<i>2.04</i>
26	4.250E-08	<i>2.20</i>	<i>2.20</i>	<i>2.20</i>	<i>2.20</i>	<i>2.20</i>	<i>2.20</i>
27	4.660E-08	<i>2.36</i>	<i>2.36</i>	<i>2.36</i>	<i>2.36</i>	<i>2.36</i>	<i>2.36</i>
28	5.040E-08	<i>2.52</i>	<i>2.52</i>	<i>2.52</i>	<i>2.52</i>	<i>2.52</i>	<i>2.52</i>
29	5.330E-08	<i>2.68</i>	<i>2.68</i>	<i>2.68</i>	<i>2.68</i>	<i>2.68</i>	<i>2.68</i>
30	5.560E-08	<i>2.84</i>	<i>2.84</i>	<i>2.84</i>	<i>2.84</i>	<i>2.84</i>	<i>2.84</i>
	6.060E-08	<i>3.00</i>	<i>3.00</i>	<i>3.00</i>	<i>3.00</i>	<i>3.00</i>	<i>3.00</i>

Plain text: Direct fit to Mie curve

Bold text: Smooth fit through Mie curve multi-valued region

Italics: Bin diameters taken from PMS calibration

Table C.1.2. ASASP-X channel threshold response as scattering cross section and equivalent RH dependent refractive index bin diameters in μm.

C.2 Transformation of Bin Data to Aerosol Distributions

The bin diameter limits given in Table C.1.2 represent, in some cases, combinations of the 60 channels defined by the ASASP-X PHA. The 30 channels used in this work result from discarding channel one and two in amplification range 3, from lumping together counts in either two or three adjacent channels in amplification ranges 2 and 3, and from employing an overlapping scheme in regions of equivalent response in adjacent amplification ranges.

Table C.2.1 illustrates how the 60 original PHA channels are boiled down to 30 bins for presentation of size distributions in this work. The channel number corresponds to the PHA channel for a respective amplification range. The bin number corresponds to the lumped bins shown in Table C.1.2. The overlap column is described later, as are the scale factors for the overlap regions. Note that the bin which precedes the first overlap region in a given amplification range must be scaled since all overlapping plotting bins are scaled to the threshold response range of the next lower (numerically) amplification range. Bin limits for refractive index of 1.58, as well as the manufacturer's bin limits (ASASP-X operation manual) are included in Table C.2.1. The PSL size(s) used to calibrate the ASASP-X in each amplification range are shown, with the PHA channel in which maximum counts were observed. Relative amplification range gains are also shown, and are simply the respective amplification range calibration constants divided by the calibration constant for range 0.

The data reduction scheme used in this work averages counts in amplification range overlap regions where counts in equivalent response regions are redundant. PHA channels with the nearest matching calibrated response are used to define overlap regions. In the event that overlap in adjacent ranges does not match precisely, the closest overlapping channels are multiplied by the ratio of Δ (log of threshold response) for the overlap regions. Once the response range of respective overlap regions are equated, the counts in the matching overlap regions are averaged for use in some of the final 30 ASASP-X bins.

Comparison of total counts in the overlap regions allows a confidence check in the overlapping scheme since respective overlapping regions should have nearly equivalent

counts. An example of particle counts in overlapped bins is given in Table C.2.2 for a representative aerosol size distribution using the OPC calibration constants and field data from this work. As an example of one overlap region, Upper range 3 overlap region one, or Upper R3 OL 1 in Table C.2.2, corresponds to PHA channels 14 and 15 for amplification range 3. Lower R2 OL 1 corresponds to PHA channels 1 and 2 from amplification range 2. The TR spanned by each of these overlap regions is given in the second column of Table C.2.2, and indeed the response ranges overlap, although not precisely. As indicated in the Δ log TR column, the Upper R3 OL 1 spans a slightly greater response range than Lower R2 OL 1. Thus, in order to equate the particle counts contained in each overlap region, the Upper R3 OL 1 is scaled by 0.15/0.21 to give the resulting particle number concentration shown in the right most column. The upper overlap regions are always scaled to the TR range of the lower (numerically) amplification range overlap region. Finally, the particle counts in the upper and lower overlap regions are averaged to give the particle counts in the respective overlap region for adjacent amplification ranges. In the example described here, the overlap region corresponds to bin 4 in Table C.1.2. If all this seems like it was a pain in the neck to figure out, you're right, it was.

ASASP-X calibration using observed PSL channel(s)
and CSU derived relative channel threshold voltages.

		Calibration				Scale n = 1.58 PMS			
Range 3		Channel	Voltage	Response	Bin	Overlap	Factor	Dp	Dp
Gain	341.82	1	0.00		0				0.09
		2	0.20	3.596E-12	0			0.11	0.10
PSL Calibration size(s)		3	0.33	5.854E-12	1			0.12	0.10
channel 14, .19um		4	0.46	8.196E-12	1			0.12	0.11
		5	0.66	1.171E-11	2			0.13	0.12
<u>V/cm^2</u>	<u>5.64E+10</u>	6	0.92	1.631E-11	2			0.14	0.13
		7	1.23	2.174E-11	3		.30/.34	0.14	0.13
		8	1.59	2.823E-11	3			0.15	0.14
		9	2.09	3.701E-11	3			0.16	0.15
		10	2.64	4.684E-11	4	UR3OL1	.15/.21	0.16	0.15
		11	3.29	5.834E-11	4	UR3OL1		0.17	0.16
		12	4.29	7.611E-11	5	UR3OL2	.28/.36	0.18	0.17
		13	5.26	9.325E-11	5	UR3OL2		0.19	0.17
		14	6.46	1.146E-10	5	UR3OL2		0.19	0.18
		15	7.92	1.405E-10	5	UR3OL2		0.20	0.19
			9.72	1.723E-10				0.21	0.20

		Calibration				n = 1.58 PMS			
Range 2		Channel	Voltage	Response	Bin	Overlap		Dp	Dp
Gain	51.27	1	0.36	4.264E-11	4	LR2OL1	1	0.16	0.15
		2	0.51	5.991E-11	5	LO2OL2	1	0.17	0.16
PSL Calibration size(s)		3	0.70	8.258E-11	5	LO2OL2		0.18	0.17
channel 7/8, .25um		4	0.98	1.160E-10	6			0.19	0.18
channel 5, .19um		5	1.30	1.533E-10	6			0.20	0.19
channel 15, .30um		6	1.74	2.051E-10	7			0.21	0.20
		7	2.25	2.658E-10	7			0.23	0.21
<u>V/cm^2</u>	<u>8.46E+09</u>	8	2.81	3.319E-10	8		.22/.19	0.24	0.22
		9	3.58	4.237E-10	8			0.25	0.23
		10	4.32	5.101E-10	9	UR2OL1	.28/.31	0.26	0.24
		11	5.11	6.045E-10	9	UR2OL1		0.27	0.25
		12	5.80	6.855E-10	9	UR2OL1		0.28	0.26
		13	6.85	8.096E-10	9	UR2OL1		0.29	0.27
		14	7.76	9.176E-10	9	UR2OL1		0.30	0.28
		15	8.77	1.036E-09	10		not used	0.30	0.29
			9.68	1.144E-09				0.31	0.30

Table C.2.1. This table describes how the 60 PHA channels were reduced to the 30 plotting bins shown in Table C.1.1. Channels that are scaled to a response region corresponding to the next (lower) amplification range are offset by solid lines.

ASASP-X calibration using observed PSL channel(s)
and CSU derived relative channel threshold voltages.

		Calibration				Scale n = 1.58 PMS			
		Channel Voltage	Response	Bin	Overlap	Factor	Dp	Dp	
Range 1		1	0.37	5.545E-10	9	LR1OL1	1	0.26	0.24
Gain	4.02	2	0.69	1.035E-09	10			0.30	0.28
		3	1.07	1.608E-09	11			0.34	0.32
PSL Calibration size(s)		4	1.57	2.366E-09	12			0.38	0.36
channel 5, .41um		5	2.08	3.142E-09	13			0.45	0.40
channel 5, .47um		6	2.65	3.993E-09	14			0.51	0.44
channel 2, .30um		7	3.24	4.880E-09	15		1	0.57	0.48
		8	3.90	5.878E-09	16	UR1OL1	1	0.62	0.52
		9	4.61	6.950E-09	16	UR1OL1		0.66	0.56
<u>V/cm²</u>	<u>6.63E+08</u>	10	5.32	8.022E-09	16	UR1OL1		0.70	0.60
		11	6.10	9.205E-09	17	UR1OL1	1	0.73	0.64
		12	6.84	1.031E-08	17	UR1OL2		0.77	0.68
		13	7.55	1.139E-08	17	UR1OL2		0.81	0.72
		14	8.28	1.250E-08	17	UR1OL2		0.85	0.76
		15	9.02	1.360E-08	17	UR1OL2		0.88	0.80
			9.61	1.449E-08				0.92	0.84

		Calibration				Scale n = 1.58 PMS			
		Channel Voltage	Response	Bin	Overlap	Factor	Dp	Dp	
Range 0		1	0.88	5.358E-09	16	LR0OL1	1	0.60	0.60
Gain	1	2	1.36	8.271E-09	17	LR0OL2	1	0.76	0.76
		3	2.08	1.259E-08	18			0.92	0.92
PSL Calibration size(s)		4	2.64	1.603E-08	19			1.08	1.08
channel 2, .87um		5	3.25	1.969E-08	20			1.24	1.24
		6	4.13	2.503E-08	21			1.40	1.40
<u>V/cm²</u>	<u>1.65E+08</u>	7	4.66	2.825E-08	22			1.56	1.56
		8	5.22	3.162E-08	23			1.72	1.72
		9	5.85	3.543E-08	24			1.88	1.88
		10	6.45	3.909E-08	25			2.04	2.04
		11	7.00	4.245E-08	26			2.20	2.20
		12	7.68	4.655E-08	27			2.36	2.36
		13	8.31	5.036E-08	28			2.52	2.52
		14	8.79	5.329E-08	29			2.68	2.68
		15	9.18	5.563E-08	30			2.84	2.84
			10.00	6.061E-08				3.00	3.00

Table C.2.1 (continued). This table describes how the 60 PHA channels were reduced to the 30 plotting bins shown in Table C.1.1. Channels that are scaled to a response region corresponding to the next (lower) amplification range are offset by solid lines.

PHA Overlap Region	Channel Threshold Response (cm ² /particle)	$\Delta \log TR$	Counts cm ⁻³
			081195 Run #3
Upper R3 OL 1	4.68E-11 to 7.61E-11	0.21	58.8
Lower R2 OL 1	4.27E-11 to 5.99E-11	0.15	56.3
Upper R3 OL 2	7.61E-11 to 1.72E-10	0.36	98.6
Lower R2 OL 2	5.99E-11 to 1.16E-10	0.28	98.9
Upper R2 OL 1	5.10E-10 to 1.04E-9	0.28	70.6
Lower R1 OL 1	5.55E-10 to 1.04E-9	0.31	65.6
Upper R1 OL 1	5.88E-9 to 9.21E-9	0.19	1.2
Lower R0 OL 1	5.36E-9 to 8.27E-9	0.19	0.6
Upper R1 OL 2	9.21E-9 to 1.45E-8	0.20	0.6
Lower R0 OL 2	8.27E-9 to 1.26E-8	0.18	0.2

Table C.2.2. An example of particle counts in overlap regions of the four ASASP-X amplification ranges for one aerosol size distribution using the calibration in this work. Counts in corresponding overlap regions should be about the same. Counts in the upper overlap region are scaled to the TR range of the corresponding lower overlap region.

C.3 Presentation of Aerosol Size Distributions

Aerosol size distributions in Section 4 are plotted as the appropriate density function, obtained by dividing the aerosol number or volume concentration in each bin, ΔN or ΔV , by the width of the respective bin, $\Delta \ln D_{pm}$ versus the log of the bin midpoint diameter, $\log D_{pm}$. This type of presentation ensures that the area under the size distribution curve is proportional to the integrated number or volume concentration for that size distribution.

The aerosol volume concentration time line shown in Figure 4.1.2, and the D_{pg} and σ_g time lines in Figures 4.1.3 and 4.1.4, are intended to represent accumulation mode aerosol. The upper size limit of the accumulation mode changed throughout the course of the study due to fluctuations in ambient aerosol size distribution characteristics, and the cutoff diameter was adjusted accordingly. A section of the data processing code used for this work to adjust the floating cutoff parameter is included below. The cutoff parameter was set by looking at all the aerosol size distributions from this study and setting the upper limit of the accumulation mode with the variable 'xgend', corresponding to the upper size bin used to calculate statistics for a given aerosol size distribution. The cutoff parameter changes for a given day or group of days and is occasionally adjusted as a function of RH.

```

if startdate ge 195 then begin
xgend = 15
if rh ge 40 then xgend = 16
if rh ge 60 then xgend = 17
endif
if startdate ge 199 then xgend = 14
if startdate ge 200 then xgend = 15
if startdate ge 201 then xgend = 16
if startdate ge 202 then xgend = 14
if startdate ge 203 then begin
xgend = 14
if rh ge 65 then xgend = 16
endif
if startdate ge 205 then xgend = 12
if startdate ge 208 then begin
xgend = 13
if rh ge 65 then xgend = 16
endif
if startdate ge 210 then xgend = 13
if startdate ge 211 then xgend = 14
if startdate ge 212 then xgend = 13
if startdate ge 215 then xgend = 12
if startdate ge 216 then xgend = 11
if startdate ge 219 then begin
xgend = 14
if rh ge 40 then xgend = 16
endif
if startdate ge 221 then begin
xgend = 15
if rh ge 40 then xgend = 16
if rh ge 60 then xgend = 17
endif
if startdate ge 224 then xgend = 16
if startdate ge 225 then xgend = 15
if startdate ge 229 then xgend = 16
if startdate ge 232 then xgend = 15

```

Figure C.3.1. Section of code from data processing program ‘asasp.pro’ that determines the floating cutoff parameter with respect to JD and RH.

The floating accumulation mode cutoff is important since aerosol distribution parameters, as calculated by Equations 2.4.1 and 2.4.2 for accumulation mode aerosol, are sensitive to the presence of large mode aerosol that may be present in the upper size tail of the accumulation mode. Chemical signatures consistent with large mode aerosol occur during the dust period, at the onset of synoptic flow from Hurricane Erin on JD 215, and

during the transition period. During these times, a large mode is clearly observed in the OPC size distributions. The presence of significant amounts of large mode aerosol will skew the integrated aerosol volume concentration, MMD and σ_g towards larger values if the accumulation mode cutoff is overestimated.

C.4 Data Acquisition and Processing Programs

The ASASP-X used software, written in C, and an interface card from the Spec 1D company to transfer signals from the PHA to corresponding particle counts on a personal computer (PC). The data acquisition program was set to gather raw particle counts accumulated by the ASASP-X every second. Data files were written every minute in hexadecimal format. The raw data from this study therefore resides in one minute files with one second time resolution. However, the ASASP-X only collects data in one of its four amplification ranges at a given time requiring that data files be combined, as described in section C.2, to construct a size distribution.

An intermediate program, written by Dr. Dave Rogers in C, converted the Spec 1D program hexadecimal output to more conventional Arabic format. This intermediate program allowed for combination of any number of specified raw data files into one file containing data for a specified time period. Also, this program provided the option of averaging the data so that output was reduced to one line of data for each minute of raw data, reducing the size of the working OPC data base. In this averaged form particle counts in a given channel had units of #/sec., and represented a one minute average.

The Spec 1D program introduced some quirks in the stored files, however. For example, if the amplification range was changed while a data file was being written, only data subsequent to the range change was saved, and any previous data in that file would be

overwritten by zeros. Also, following a change in the ASASP-X amplification range a large number of spurious particle counts occurred in the data, presumably due to electronic noise. For this reason, only data files, or their averages, subsequent to the files where the amplification range was changed were used in data processing for this work. Unfortunately, some good data is excluded by this approach. Since the aberrations in data acquisition were not systematic, the highest quality of processed data is ensured by this method.

To process the ASASP-X data to its final form, a third program, written by myself in the IDL language, reads the one minute averaged data files and performs the remainder of the data processing tasks necessary for this work with respect to the OPC data set. A description of this program, called 'asasp.pro', follows.

The program 'asasp.pro' is set up to read from three separate data files (or sets of data files) while it runs. One set of data files contain the ASASP-X data, which resides in one file for each day the OPC operated. These files are named with the sampling date as a prefix, such as 072595av.dat, which stands for July 25, 1995 one minute averaged data. Another set of files 'asasp.pro' reads contain daily descriptions of the size distribution scans, including the run number, the start and stop times for each scan, experimentally conditioned RH, flow rate data, indexes to plotting routines, and a string descriptor. These files are also named with a date prefix followed by run.file, such as 072595run.file. Another single file 'asasp.pro' reads contains the RH dependent bin limits and is named 'rudplist.txt', which more or less stands for rural aerosol model bin diameter list and is essentially Table C.1.2. If at some point different $n(\text{RH})$ parameters are applied to ASASP-X data then this file should be changed accordingly.

The program 'asasp.pro' forms size distributions by accumulating all the data between the start and stop times given in the run.file file. The distribution data is sorted by

amplification range and channel number to the 30 plotting bins described in Table C.1.2. At this point, corrections for depositional loss are applied (Section 3.3.1), the accumulation mode is defined (Section C.3), statistical calculations for number and volume accumulation mode distributions are performed (Section 2.4), and number and volume concentration uncertainties are calculated (Section 4.4). A large portion of 'asasp.pro' is devoted to plotting aerosol size distributions and writing to files that contain size distribution data. The main data output files are prefixed by date, such as 072595summary.dat, which contains about 30 variables pertinent to each size distribution recorded on that day. These data summary files are conveniently read by other programs, such as 'volumeav.pro' that generated the plots for dry aerosol distribution statistics in Chapter 4.

Other IDL programs used in this work to process data sets from SEAVS are: 'chem.pro' which reads the IMPROVE and HEADS chemical data sets and is used to reconstruct aerosol fine mass during SEAVS (Figures in Section A.3) as well as produce some of the plots in Chapter 5. 'cnc.pro' and its analogues read the [CN] data set taken by CSU during SEAVS (Figure A.1.1). One version of the cnc.pro program reads the size distribution run.files and computes the average ambient [CN] over the period ASASP-X size distribution data were collected. Plenum data from the CSU/NPS special study, which contains the plenum and ASASP-X temperature and RH data, is read by 'plenum.pro'. 'plenum.pro' calculates RH and temperature averaged over the time period ASASP-X size distribution data were collected (for example, Figure 3.4.1), and these averaged data are included in Table 4.2.1. 'met.pro' and its analogues read the meteorological data set from the CSU/NPS special study (Figures A.2.1 and A.2.2).

APPENDIX D

Partial Molar Refractive Index Calculations

Aerosol water contents derived in this work are used to calculate the ambient aerosol refractive index as a function of RH. The extra trouble of reconstructing refractive index may seem unnecessary, since RH dependent refractive indices from the literature was used in the to process the ASASP-X data initially. The reconstructed refractive indices presented here are useful as a check the appropriateness of the initial refractive index choices used in the OPC data inversion. Also, the partial molar refractive index approach allows for assessment of the effect solute composition has on particle refractive index. The possibility that this technique may somehow be used in conjunction with the OPC data set to arrive at the actual RH dependent refractive index for ambient aerosol is considered.

D.1 Partial Molar Refractive Index Calculations for Dry and Humidified Aerosol

The partial molar refractive index is used to reconstruct ambient particle refractive index by assuming internal aerosol mixtures and applying the partial molar refractive index of each primary chemical component. Chemical data from the IMPROVE samplers was used to reconstruct daily averages of the dry aerosol composition during SEAVS. The calculations in this section assume the ambient particles are composed of sulfate and ammonium ions, organic and elemental carbon, and water. The soil fraction is ignored since only accumulation mode aerosol are used to determine water uptake. This rationale is in part substantiated by the presence of a large mode is the aerosol volume distributions recorded by the ASASP-X during times when a significant soil chemical mass fraction is also present.

The partial molar refractive index used for sulfate ions is $13.45 \text{ cm}^3 \text{ mole}^{-1}$, for ammonium ions, $4.89 \text{ cm}^3 \text{ mole}^{-1}$ (Tang and Munkelwitz, 1994), for organic carbon $19.11 \text{ cm}^3 \text{ mole}^{-1}$, and for water $3.71 \text{ cm}^3 \text{ mole}^{-1}$ (Stelson, 1990). The ionic fraction density is taken as that of dry ammonium sulfate, 1.76 g cm^{-3} , corresponding to refractive indices of $n = 1.53$ for ammonium sulfate and $n = 1.47$ for ammonium bisulfate. The partial molar refractive index for organic and elemental carbon corresponds to a density of 1.4 g cm^{-3} , MW of 84 g mole^{-1} and $n = 1.55$. Water is assumed to have unit density with a MW of 18 g mole^{-1} and $n = 1.33$. R_i , the partial molar refractive index, is given by equation D.1.1 where n_i is the refractive index and ρ_i the density for component i .

$$R_i = V_i \left(\frac{n_i^2 - 1}{n_i^2 + 2} \right) \quad \text{D.1.1}$$

$$V_i = \frac{MW_i}{\rho_i} \quad \text{D.1.2}$$

The partial molar volume of component i is given by V_i in equation D.1.2.

The real component of refractive index for the composite mixed phase aerosol was calculated following equations D.1.3 and D.1.4 as presented in Stelson (1990).

$$\frac{R}{V} = \frac{\sum \frac{R_i S_i}{MW_i}}{A_v} \quad \text{D.1.3}$$

$$n = \left(\frac{(1 + 2 \frac{R}{V})}{(1 - \frac{R}{V})} \right)^{\frac{1}{2}} \quad \text{D.1.4}$$

S_i ($\mu\text{g m}^{-3}$) is the aerosol mass concentration for component i , and A_v ($\mu\text{m}^3 \text{ cm}^{-3}$) is the integrated aerosol volume. In equation D.1.4, n is the composite solute refractive index. When S_i is taken directly from chemical data, equations D.1.1 to D.1.4 make n independent of particle density. This approach is subject to uncertainty introduced, for example, by organic and elemental carbon mass reconstruction and their optical properties during SEAVS since these quantities are not yet well characterized. Also, this method is used to reconstruct

the refractive index of accumulation mode aerosol for which size resolved chemistry is not yet available from SEAVS data sets.

Figure D.1.1 shows the reconstructed aerosol refractive index during SEAVS on a daily basis. Chemical mass concentrations are apportioned to the components described above, with the notable exception being the soil fraction, as this reconstruction is intended to represent accumulation mode aerosol. The mean aerosol refractive index for SEAVS is 1.51 (JD 196 to 233) with a range from 1.53 to 1.47. Note that the refractive index approaches that of ammonium bisulfate during the polluted SEAVS period when the aerosol were more acidic, and the refractive index approaches that of ammonium sulfate when the aerosol were more neutralized. Mean refractive indices for a early SEAVS (JD 196 to 219) and late SEAVS (JD 220 to 233) were 1.52 and 1.50, respectively.

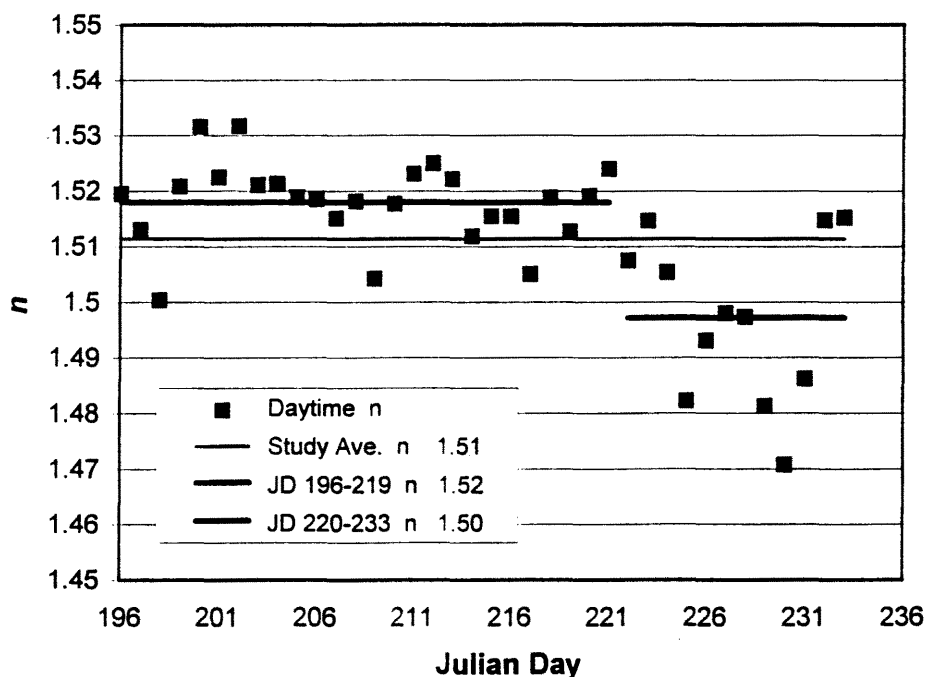


Figure D.1.1. Refractive index reconstructed for accumulation mode aerosol during SEAVS. A study mean refractive index of $n = 1.51$ is indicated, with higher refractive index values in the early part of SEAVS and lower values towards the end of the study.

In application of the partial molar refractive index approach to humidified aerosol, A_V was taken from the dry aerosol volumes used in the water uptake determinations (presented in Section 4.3). For this reason, component chemical mass, S_i , was calculated from the dry aerosol volume recorded by the ASASP-X, and not daily averages from chemical data, since daily fluctuations in dry aerosol mass were considered. S_i , therefore, was calculated by multiplying the ASASP-X dry aerosol volume by the component mass fraction, obtained from chemical data, and an average mixed phase density. Dry sulfate mass concentration, for example, is given by:

$$S_{SO_4} = \bar{\rho} A V_o \chi_{SO_4} \quad \text{D.1.5}$$

$$\bar{\rho} = \frac{1}{\frac{\chi_1}{\rho_1} + \frac{\chi_2}{\rho_2}} \quad \text{D.1.6}$$

The volume conserved mixture density, $\bar{\rho}$, was calculated from equation D.1.3 using sulfate and organic carbon mass fractions, and respective pure component densities given in the beginning of this Appendix. For humidified aerosol, the added water mass fraction and density were added to Equation D.1.6. The mass of added water ($\mu\text{g m}^{-3}$), needed to calculate component mass fractions, is given by:

$$M_{H_2O} = (\rho_w V_w - \rho_o V_o) \quad \text{D.1.7}$$

Figure D.1.2 shows reconstructed n following the procedure outlined above for the pre-hurricane period. Included in Figure D.1.1 are the initial refractive index values used to process the ASASP-X data. Also included is an empirical curve for pure ammonium sulfate refractive index. Figure D.1.3 is a similar graph for the transition and polluted periods.

Figure D.1.2

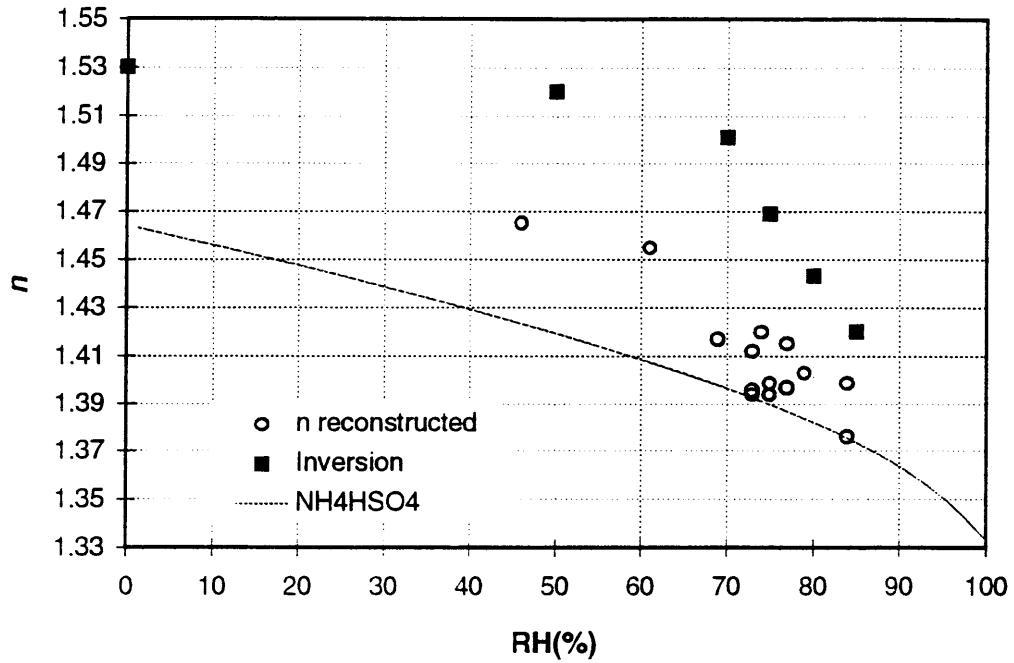
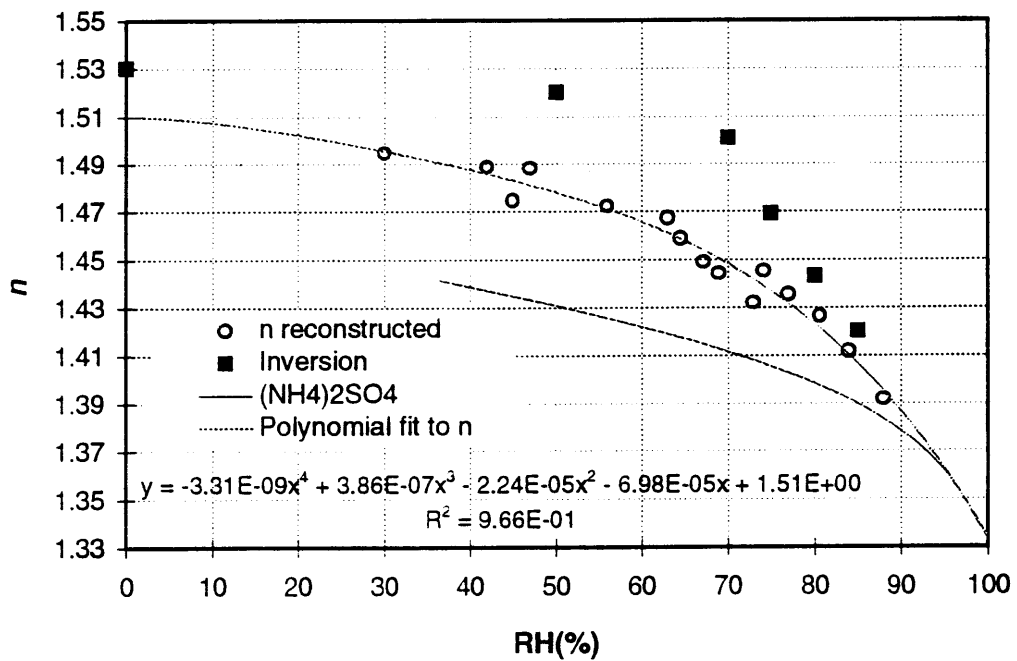


Figure D.1.3



Figures D.1.2 and D.1.3. Refractive index as a function of RH reconstructed for the pre-hurricane and polluted periods. Curves for pure ammonium sulfate and ammonium bisulfate $n(RH)$ are included as are the OPC data inversion $n(RH)$ for reference.

D.2 Conclusions

Figure D.1.2 indicates that the initial refractive indices are reconstructed fairly well during the pre-hurricane period using observed water uptake and the partial molar volume approach. However, Figure D.2.2 shows that during the transition and polluted periods the reconstructed indices of refraction are significantly lower than the initial choices of refractive index. This is a somewhat comforting result in that it suggests the initial choice of refractive index used to process the OPC data do not entirely constrain water uptake estimated by the ASASP-X. On the other hand, it implies the inversion refractive indices used in the water uptake analyses were inappropriate for the ambient aerosol during this period of SEAVS. Figures D.1.2 and D.1.3 suggest consistent trends in refractive index as a function of RH, and moreover that the trends are unique to meteorological periods during SEAVS.

An interesting question is whether the RH dependence of the actual refractive index for ambient aerosol sampled during SEAVS is in some way alluded to by Figures D.1.2 and D.1.3. In order to answer this question an iterative procedure might be employed, in which the $n(\text{RH})$ values determined using experimental aerosol water content are used to reprocess the OPC data, leading to new estimates of water content. Ultimately, these iterations should converge to yield a self consistent set of $n(\text{RH})$ and water contents.

Upon initial mental inspection it appears that using reconstructed refractive indices to reprocess the OPC data could add successively more water to the aerosol size distributions until the reconstructed refractive indices simply approach a lower allowable limit. If the reconstructed refractive indices converge to the refractive index of water, the lower theoretical limit, then clearly the iteration hypothesis is unreasonable. If, in application of this iteration technique, the shape of the aerosol distributions become discontinuous then a reasonable lower limit on the set of refractive indices that can be applied to the data would result.

It should be pointed out that uncertainty in water uptake based on experimental considerations alone will produce uncertainty in any set of refractive indices obtained through partial molar reconstruction. It is possible that the uncertainty in reconstructed refractive indices based on uncertainty in water uptake would exceed the reasonable range of refractive indices obtained from iteration. If the iteration technique is of any use, a set of refractive indices obtained by iteration can only approximate the actual refractive indices for ambient aerosol during SEAVS within the range of experimental uncertainty in water uptake.

Another simpler, and perhaps more direct approach would be to process the OPC data with the best estimate of $n(\text{RH})$ from other researchers during SEAVS. Then, the partial molar refractive index approach could be used to reconstruct an experimental $n(\text{RH})$. One would then check whether the initial refractive index values are returned by the refractive index reconstruction. If they were, then initial choices of refractive index are supported. If the initial refractive index values are not returned by the partial molar refractive index reconstruction, then microphysical and optical parameters of the constituent chemical species, such as organic carbon density and refractive index, could be adjusted within reasonable ranges to return the experimental estimates of refractive index.

It is practically unreasonable to derive experimental $n(\text{RH})$ from OPC size distribution data alone since the RH dependent OPC size distributions depend on some initial choices of RH dependent refractive index. Nonetheless, such reconstructions of refractive index using OPC data are useful consistency checks.

Oversized Table 4.2.1

Mid JD: The midpoint time of the size distribution, in Julian Day.

Run #: The sequential run number of the size distribution.

RH: The experimentally conditioned RH measured just downstream of the ASASP-X laser cavity. This represents an average during the size distribution scan.

Volume:

$D_p < 2.5 \mu\text{m}$: The integrated aerosol volume concentration for aerosols measured by the ASASP-X below $2.5 \mu\text{m}$.

Acc. Mode: Integrated aerosol volume for the ASASP-X accumulation mode.

Uncertainty: The accumulation mode volume concentration percent uncertainty as calculated by Equation 4.4.6.

$D_{p,g}$: The accumulation mode MMD.

σ_g : The accumulation mode geometric standard deviation.

Dry Run #(s): The run number(s) of the dry aerosol size distribution from that JD used to calculate R . If two runs are present, the dry volume concentration used in the water uptake calculation is the average of the two dry aerosol volume concentrations.

$f(\text{RH})$ Run #: The humidified run number used to calculate R .

Total D/Do: R calculated by Equation 4.3.1 for particles below $2.5 \mu\text{m}$.

Acc. Mode D/Do: R calculated by Equation 4.3.1 for accumulation mode particles.

D/Do Uncertainty: Percent uncertainty in R calculated by Equation 4.4.8.

MMD D/Do: R calculated for accumulation mode aerosol by Equation 4.3.2.

Table 4.2.1

Aerosol Distribution Statistics and Water Uptake

Mid JD	run #	RH (%)	Volume:		Uncertainty (%)	Dp,g (μm)	σg	Dry Run #(s)	f(RH) Run #	Total	Acc. Mode	D/Do	MMD D/Do
			Dp < 2.5 μm ($\mu\text{m}^3/\text{cm}^3$)	Acc. Mode ($\mu\text{m}^3/\text{cm}^3$)						(V/Vo) ^{1/3} D/Do	(V/Vo) ^{1/3} D/Do	Uncertainty (%)	
195.474	3	14	20.88	19.88	9.5	0.324	1.66						
195.497	4	67	31.48	30.42	9.6	0.372	1.78	3,6	4	1.16	1.17	6.4	1.14
195.538	5	67	30.04	29.21	9.8	0.373	1.76	3,6	5	1.14	1.15	6.5	1.15
195.561	6	7.6	19.79	18.54	9.8	0.327	1.67						
196.353	1	18	16.36	15.59	9.5	0.338	1.68						
196.371	2	84	28.18	27.66	12.1	0.484	2.02	1,3	2	1.22	1.23	7.3	1.44
196.392	3	16	14.88	14.35	9.9	0.334	1.66						
196.414	4	69	24.20	23.85	10.4	0.385	1.78	3,5	4	1.18	1.20	7.0	1.16
196.438	5	11	14.29	13.47	11.0	0.333	1.67						
196.453	6	63	24.33	23.70	10.5	0.382	1.81	5,7	6	1.20	1.21	7.2	1.15
196.478	7	11	13.85	13.07	11.2	0.333	1.68						
196.641	8	14	15.01	14.45	11.3	0.327	1.67						
196.683	9	12	15.74	14.88	10.9	0.326	1.67						
196.701	10	66	26.41	25.78	10.4	0.378	1.77	9,11	10	1.22	1.23	7.2	1.16
196.726	11	11	13.52	12.67	11.8	0.326	1.67						
196.744	12	59	17.50	16.88	10.6	0.341	1.68	11,13	12	1.18	1.19	8.1	1.06
196.767	13	11	7.77	7.39	15.8	0.315	1.65						
196.790	14	58	6.93	6.71	16.9	0.341	1.65	13	14	0.96	0.97	10.9	1.08
197.331	1	56	14.34	14.00	10.5	0.352	1.66						
197.361	2	10	9.69	9.07	14.0	0.334	1.63						
197.396	3	23	10.54	10.08	13.2	0.335	1.66	2	3	1.03	1.04	9.0	1.00
197.413	4	35	13.38	12.59	11.6	0.330	1.65						
197.435	5	48	15.10	14.77	11.1	0.341	1.70						
197.452	6	50	15.53	14.83	11.2	0.340	1.67						
197.562	10	17	15.50	14.84	10.7	0.329	1.68						
197.579	11	38	18.44	17.49	10.3	0.335	1.67	10	11	1.06	1.06	7.0	1.02
197.624	12	60	23.15	22.47	8.9	0.358	1.69						
197.646	13	56	21.22	20.55	9.7	0.351	1.71						
197.732	14	65	27.74	26.80	10.0	0.387	1.82						
198.372	1	75	31.05	31.05		0.417	1.83						
198.393	3	68	17.79	17.79		0.369	1.77						

Table 4.2.1

Aerosol Distribution Statistics and Water Uptake

Mid JD	run #	Volume:		Acc. Mode ($\mu\text{m}^3/\text{cm}^3$)	Uncertainty (%)	Dp,g (μm)	σ	Dry Run #(s)	f(RH) Run #	Total	Acc. Mode	D/Do	MMD D/Do
		RH (%)	Dp < 2.5 μm ($\mu\text{m}^3/\text{cm}^3$)							(V/Vo) ^{1/3} D/Do	(V/Vo) ^{1/3} D/Do	Uncertainty (%)	
199.549	1		12.96	7.46	18.6	0.280	1.78						
199.628	2		12.33	8.48	17.6	0.268	1.63						
199.652	3		9.79	9.16	17.2	0.261	1.59						
199.705	4		10.71	10.05	16.3	0.263	1.61						
199.724	5		10.91	10.26	15.4	0.265	1.60						
199.741	6		9.96	9.15	16.3	0.265	1.60						
200.358	1	63	9.57	7.90	23.3	0.250	1.79						
200.420	4	52	6.00	5.74	22.1	0.228	1.60						
200.444	5	52	7.24	6.40	20.6	0.236	1.67						
200.491	6	52	6.40	5.83	22.0	0.226	1.59						
200.529	7	49	8.73	5.86	21.7	0.232	1.65						
200.601	8	48	8.45	7.68	15.8	0.226	1.61						
200.618	9	50	7.19	7.16	18.5	0.223	1.58						
201.410	2	60	17.97	17.09	11.3	0.293	1.75						
201.432	3	61	21.55	20.47	12.9	0.307	1.85						
201.457	4	64	21.29	20.37	13.1	0.302	1.85						
201.501	5	57	17.46	16.64	12.0	0.273	1.74						
201.644	6	51	16.74	16.74	11.8	0.273	1.71						
201.704	8	40	13.37	13.37	12.5	0.260	1.69						
201.736	9	35	12.02	10.97	14.2	0.266	1.73						
201.762	10	35	12.29	11.50	14.0	0.263	1.70						
201.786	11	35	10.30	9.86	15.7	0.260	1.70						
202.438	2	12	11.35	10.91	13.8	0.257	1.59						
202.454	4	67	14.51	13.67	17.0	0.285	1.63	2,5	4	1.09	1.09	10.3	1.11
202.481	5	11.7	10.83	10.43	14.3	0.257	1.60						
202.520	7	77.1	21.65	20.34	15.9	0.303	1.66	7	5	1.26	1.25	10.1	1.18
202.530	8	77.3	18.78	17.91	18.2	0.298	1.64	8	5	1.20	1.20	10.8	1.16
202.556	9	67	9.62	8.77	19.3	0.284	1.63						
202.569	10	67	9.87	8.81	19.4	0.290	1.64						
202.587	11	57	8.18	7.70	17.0	0.273	1.57						
202.598	12	57	8.98	8.04	16.7	0.272	1.57						
202.613	13	47	8.79	8.28	16.5	0.274	1.59						

Table 4.2.1

Aerosol Distribution Statistics and Water Uptake

Mid JD	run #	RH (%)	Volume:			Dp,g (μm)	σg	Dry Run #(s)	f(RH) Run #	Total	Acc. Mode	D/Do	MMD D/Do
			Dp < 2.5μm (μm ³ /cm ³)	Acc. Mode (μm ³ /cm ³)	Uncertainty (%)					(V/Vo) ^{1/3} D/Do	(V/Vo) ^{1/3} D/Do	Uncertainty (%)	
202.659	17	24	6.70	6.33	17.6	0.268	1.60	18	17	0.99	0.99	11.7	1.00
202.680	18	10	6.97	6.48	17.6	0.267	1.61						
203.475	3	13	2.80	2.79	31.2	0.220	1.43						
203.497	5	77	4.60	4.48	37.3	0.278	1.77	3,6	5	1.21	1.21	23.2	1.14
203.531	6	8.5	2.41	2.22	33.6	0.270	1.65						
203.554	7	41	3.09	2.76	30.4	0.278	1.66	6,8	7	1.07	1.06	20.9	1.03
203.577	8	10	2.68	2.44	31.0	0.271	1.67						
203.604	10	77	5.99	5.99	29.1	0.346	1.94	8,12	10	1.27	1.32	19.9	1.31
203.649	12	10	3.12	2.71	30.1	0.258	1.65						
203.676	14	69	5.88	5.58	26.0	0.298	1.79	12	14	1.23	1.27	18.7	1.16
203.745	16	85	9.56	9.39	25.4	0.359	1.99	17	16	1.34	1.37		1.37
203.766	17	13	4.01	3.69	24.9	0.262	1.65						
204.439	3	13	6.28	5.32	19.2	0.265	1.65						
204.455	4	60	7.42	6.88	18.0	0.263	1.64	3,5	4	1.11	1.13	12.9	1.01
204.480	5	11	4.72	4.30	22.0	0.254	1.64						
204.495	6	79	6.97	6.97	30.6	0.314	1.86	5	6	1.14	1.17		1.24
204.504	7	79	6.93	6.50	32.0	0.308	1.85	8	7	1.30	1.31	19.8	1.25
204.539	8	24	3.16	2.90	27.5	0.246	1.62	9	8	1.00	0.99	18.4	0.99
204.565	9	7	3.17	2.96	27.7	0.248	1.65						
204.583	10	45	4.67	4.19	24.8	0.252	1.64	10	9	1.14	1.12	17.5	1.02
204.603	11	77	6.76	6.34	30.5	0.285	1.77	9	11	1.29	1.29	19.4	1.15
204.849	12	74	6.66	6.20	27.9	0.289	1.74	13	12	1.14	1.19	17.7	1.17
204.885	13	10	4.46	3.70	25.1	0.247	1.60						
205.493	5	7	7.09	4.79	21.7	0.245	1.61						
205.525	6	15	5.21	3.02	26.2	0.241	1.58	5,7	6	0.93	0.92	16.7	0.99
205.549	7	10	5.75	3.05	26.0	0.243	1.60						
205.566	8	30	5.82	3.17	28.3	0.241	1.58	7	8	1.00	1.01	18.1	0.99
205.740	9	7	2.92	2.79	29.7	0.228	1.59						
205.764	10	50	5.12	3.85	26.4	0.235	1.55	9	10	1.21	1.11		1.03
205.800	11	7	2.62	1.75	38.3	0.224	1.59						
205.825	12	43	3.23	2.28	33.5	0.231	1.58	11,13	12	1.06	1.07	23.5	1.02
205.860	13	7	2.83	1.98	35.9	0.228	1.60						

Table 4.2.1

Aerosol Distribution Statistics and Water Uptake

Mid JD	run #	RH (%)	Volume:			Dp,g (μm)	σg	Dry Run #(s)	f(RH) Run #	Total	Acc. Mode	D/Do	MMD D/Do
			Dp < 2.5μm (μm ³ /cm ³)	Acc. Mode (μm ³ /cm ³)	Uncertainty (%)					(V/Vo) ^{1/3} D/Do	(V/Vo) ^{1/3} D/Do	Uncertainty (%)	
206.533	6	64	14.01	6.81	23.3	0.269	1.65	6	8	1.05	1.18	15.3	1.09
206.578	8	8	12.11	4.12	22.5	0.246	1.58						
206.619	9	73	14.90	5.66	26.9	0.274	1.62	10,8	9	1.09	1.10	16.5	1.13
206.658	10	7	11.12	4.46	22.9	0.240	1.56						
206.694	11	65	17.97	7.65	22.2	0.271	1.59	10	11	1.17	1.20	15.0	1.13
206.776	13	73	20.49	8.84	20.6	0.277	1.59	14	13	1.15	1.28	14.7	1.11
206.815	14	8	13.35	4.24	26.2	0.250	1.61						
207.417	5	45	8.63	4.26	26.0	0.244	1.59						
207.438	6	75	13.86	8.36	25.0	0.288	1.67	7	6	1.12	1.28	16.6	1.17
207.473	7	9	9.89	4.01	24.8	0.247	1.60						
207.496	8	69	14.22	7.68	22.2	0.279	1.63	7,9	8	1.08	1.20	15.3	1.11
207.525	9	10	12.84	4.88	22.7	0.254	1.61						
207.551	10	67	15.52	7.37	23.3	0.280	1.65	9,11	10	1.11	1.19	15.7	1.10
207.583	11	9	10.10	3.91	24.9	0.256	1.61						
207.611	12	69	10.45	5.84	25.9	0.286	1.65	11	12	1.07	1.17	16.9	1.15
207.659	13	11	7.14	3.34	28.3	0.241	1.60						
207.755	15		10.88	6.25	21.0	0.257	1.53						
207.781	16		10.32	5.31	22.5	0.244	1.54						
207.810	17	55	11.11	6.96	20.6	0.257	1.52	18	17	1.07	1.10	14.3	1.06
207.837	18	10	8.95	5.24	22.2	0.243	1.55						
207.861	19	50	10.35	6.14	21.3	0.253	1.55	18	19	1.05	1.05	14.5	1.04
208.508	2	88	17.24	15.58	21.6	0.390	1.97	2	5	1.42	1.51	15.1	1.54
208.519	3	88	15.16	13.89	22.9	0.376	1.94	5	3	1.36	1.45	15.5	1.48
208.555	5	9	5.98	4.52	23.7	0.253	1.58						
208.570	6	8	5.32	4.31	24.0	0.254	1.58						
208.595	7	73	8.96	7.88	21.9	0.300	1.73	6	7	1.19	1.22	15.3	1.18
209.396	2	12	2.82	2.09	33.8	0.261	1.59						
209.417	3	45	2.88	2.17	37.1	0.266	1.61	2,4	3	1.06	1.06	25.1	1.04
209.445	4	9	2.07	1.52	42.7	0.251	1.61						
209.474	5	9	1.33	1.19	44.5	0.288	1.59						
210.352	1	18	7.35	2.41	33.3	0.236	1.54						
210.422	5	5	3.06	1.54	41.9	0.226	1.58						

Table 4.2.1

Aerosol Distribution Statistics and Water Uptake

Mid JD	run #	RH (%)	Volume:			Dp,g (μm)	σg	Dry Run #(s)	f(RH) Run #	Total	Acc. Mode	D/Do	MMD D/Do
			Dp < 2.5 μm ($\mu\text{m}^3/\text{cm}^3$)	Acc. Mode ($\mu\text{m}^3/\text{cm}^3$)	Uncertainty (%)					(V/Vo) ^{1/3} D/Do	(V/Vo) ^{1/3} D/Do	Uncertainty (%)	
210.536	9	8	3.86	2.80	30.8	0.241	1.63						
210.577	10	81	6.89	5.47	40.0	0.297	1.80	9,11	10	1.22	1.24	23.9	1.25
210.695	11	6	3.80	2.90	32.7	0.234	1.63						
210.718	12	67	5.53	4.51	31.5	0.259	1.70	11	12	1.13	1.16	21.4	1.10
211.436	3	10	2.72	2.49	30.1	0.247	1.63						
211.454	4	63	4.21	3.54	35.4	0.271	1.70	3,6	4	1.15	1.11	22.3	1.09
211.479	6	10	2.78	2.74	32.6	0.249	1.64						
211.499	8	84	9.07	8.20	31.1	0.333	1.89	6,10	8	1.35	1.33	19.5	1.35
211.540	10	8	4.60	4.25	22.2	0.245	1.64						
211.562	11	7	5.39	4.58	23.9	0.247	1.64						
212.401	3	6	4.78	4.07	25.2	0.246	1.60						
212.433	4	77	9.06	8.09	27.4	0.288	1.67	3,6	4	1.20	1.22	17.0	1.16
212.465	6	9	5.62	4.81	22.2	0.251	1.59						
212.502	7	47	6.95	6.20	20.6	0.257	1.59	6,8	7	1.06	1.07	14.4	1.02
212.528	8	9	6.08	5.32	22.8	0.253	1.59						
212.543	9	8	5.80	5.09	22.0	0.250	1.60						
212.646	10	9	5.38	4.90	22.2	0.251	1.59						
212.656	11	6	5.78	5.21	21.8	0.254	1.60						
212.678	12	56	7.78	7.03	19.4	0.262	1.58	11,13	12	1.09	1.11	13.7	1.03
212.708	13	7	6.07	5.15	21.6	0.255	1.60						
213.417	3	5	5.34	4.32	23.9	0.261	1.56						
213.444	4	69	8.66	7.87	22.7	0.291	1.60	3,6	4	1.17	1.18	14.6	1.12
213.481	6	10	5.56	5.15	18.4	0.258	1.58						
213.499	7	6	5.97	5.21	21.5	0.260	1.59						
213.525	8	42	7.97	7.24	17.8	0.268	1.61	7,9	8	1.06	1.06	12.8	1.04
213.566	9	5	7.35	6.83	19.6	0.255	1.61						
213.578	10	5	7.68	6.88	18.9	0.263	1.63						
213.594	11	30	8.81	8.00	17.6	0.256	1.62	10	11	1.05	1.05	12.2	0.97 a
213.604	12	30	8.42	7.98	16.5	0.257	1.61	12	13	0.98	0.97	11.1	1.00
213.625	13	10	8.99	8.62	16.7	0.257	1.64						
214.414	3	47	6.62	5.88	22.2	0.268	1.55	4	3	1.05	1.05	14.7	1.02
214.440	4	10	5.73	5.04	21.8	0.261	1.59						

Table 4.2.1

Aerosol Distribution Statistics and Water Uptake

Mid JD	run #	RH (%)	Volume:			Dp,g (μm)	σg	Dry Run #(s)	f(RH) Run #	Total	Acc. Mode	D/Do	MMD D/Do
			Dp < 2.5μm (μm ³ /cm ³)	Acc. Mode (μm ³ /cm ³)	Uncertainty (%)					(V/Vo) ^{1/3} D/Do	(V/Vo) ^{1/3} D/Do	Uncertainty (%)	
214.555	9	38	8.03	6.71	19.3	0.267	1.59	8	9	1.12	1.10	13.7	1.02
214.570	10	39	8.43	7.54	17.9	0.263	1.59	11	10	1.09	1.10	12.9	1.00
214.595	11	8	6.48	5.70	20.8	0.263	1.62						
214.628	13	52	5.41	4.89	23.8	0.267	1.61	11	13	0.94	0.95	14.9	1.01 a
214.643	14	52	5.68	4.95	22.7	0.269	1.58	15	14	1.22	1.18	18.1	1.17 a
214.793	15	5	3.16	3.01	31.6	0.230	1.49						
214.803	16	5	2.96	2.93	32.4	0.226	1.49						
214.826	18	86	11.42	10.69	27.9	0.322	1.67	16	18	1.57	1.54	20.1	1.42
214.839	19	87	13.08	11.95	25.4	0.325	1.66	21	19	1.56	1.59	19.0	1.45
214.871	21	12	3.43	2.98	31.7	0.224	1.52	16	21	1.05	1.00	21.4	0.99
215.424	4	43	4.19	1.10	52.2	0.252	1.48	5	4	1.10	1.12	36.0	1.02
215.465	5	7	3.14	0.79	55.7	0.246	1.51						
215.501	7	78	4.85	2.13	58.1	0.330	1.60	5,9	7	1.11	1.24	35.9	1.31
215.539	9	9	4.02	1.42	43.4	0.259	1.54	5	9	1.08	1.22	33.0	1.05 a
216.375	1	7	2.14	1.13	47.8	0.270	1.43]	
216.395	2	7	2.44	1.07	48.6	0.272	1.44	1	2	1.05	0.98	32.1	1.01
216.413	3	42	2.38	1.30	44.4	0.284	1.42	2	3	0.99	1.07	31.0	1.05
219.439	3	10	3.08	2.57	29.5	0.277	1.59						
219.469	5	80	7.16	6.82	31.6	0.369	1.99	3,7	5	1.31	1.36	20.1	1.33
219.516	7	12	3.27	2.88	27.9	0.276	1.61	3	7	1.02	1.04		1.00
220.418	4	45	2.69	2.69	31.7	0.274	1.60	4	5	0.96	1.03	19.9	1.01
220.439	5	12	3.03	2.47	29.9	0.270	1.60						
220.470	6	81	7.73	7.56	30.1	0.395	2.06	5,7	6	1.33	1.40	19.5	1.42
220.512	7	10	3.48	3.02	27.0	0.286	1.67						
220.551	8	46	2.41	2.21	33.5	0.291	1.77	7,9	8	0.96	0.98	21.9	1.07
220.591	9	10	1.96	1.73	37.7	0.258	1.64						
221.488	3	5	2.82	2.66	37.7	0.284	1.80						
221.518	4	6	5.13	4.26	23.7	0.304	1.77						
221.577	5	84	16.90	16.37	18.9	0.505	2.44	4,7	5	1.43	1.48	13.5	1.64
221.643	7	7	6.48	5.91	19.2	0.312	1.87						
222.316	2	7	6.18	6.06	21.4	0.306	1.73						
222.346	3	7	5.88	5.77	19.4	0.306	1.74						

Table 4.2.1

Aerosol Distribution Statistics and Water Uptake

Mid JD	run #	RH (%)	Volume:		Uncertainty (%)	Dp,g (μm)	σg	Dry Run #(s)	f(RH) Run #	Total	Acc. Mode	D/Do	MMD D/Do
			Dp < 2.5μm (μm ³ /cm ³)	Acc. Mode (μm ³ /cm ³)						(V/Vo) ^{1/3} D/Do	(V/Vo) ^{1/3} D/Do	Uncertainty (%)	
222.453	7	7	6.79	6.68	18.3	0.301	1.75						
222.480	8	7	7.04	6.94	17.9	0.293	1.70						
222.702	9	7	5.05	4.80	22.2	0.287	1.67						
222.739	10	73	15.39	14.76	15.0	0.366	1.87	9,11	10	1.43	1.44	12.2	1.27
222.794	11	8	5.49	5.14	21.2	0.289	1.69	9	11	1.03	1.02	14.5	1.01
223.421	3	7	6.31	5.73	19.8	0.292	1.74						
223.462	4	75	17.07	16.35	16.7	0.386	2.05	3,5	4	1.36	1.40	12.1	1.35
223.512	5	7	7.21	6.06	19.2	0.281	1.78						
223.553	6	79	19.34	18.65	18.6	0.369	2.08	5,7	6	1.33	1.37	12.3	1.34
223.604	7	7	9.27	8.30	17.1	0.271	1.74						
223.643	8	6	8.24	7.62	17.9	0.273	1.72						
223.681	9	7	8.43	7.59	18.6	0.273	1.70						
223.723	11	6	9.17	8.55	17.0	0.265	1.69						
223.785	12	10	8.78	8.30	17.1	0.270	1.73						
224.467	3	6	9.99	8.95	16.3	0.275	1.67						
224.523	4	6	9.94	9.47	15.6	0.271	1.61						
224.551	5	6	10.58	9.98	15.0	0.275	1.59						
224.605	6	6	10.73	9.99	15.1	0.278	1.61						
224.673	7	74	20.24	19.38	16.0	0.349	1.69	6	7	1.24	1.25	10.4	1.26
225.413	2	11	17.74	15.61	12.0	0.285	1.52						
225.445	4	73	37.05	34.13	11.9	0.362	1.67	2,6	4	1.30	1.33	8.1	1.26
225.492	6	7	15.72	13.31	12.6	0.287	1.52						
225.530	7	7	17.28	15.26	12.2	0.289	1.52						
225.564	8	7	15.66	15.54	11.9	0.292	1.50						
225.608	9	8	16.68	14.44	12.2	0.293	1.51						
226.406	2	8	17.28	14.96	12.0	0.297	1.53						
226.429	4	84	59.05	54.79	9.7	0.475	1.82	2,6	4	1.51	1.54	7.3	1.59
226.504	6	8	17.35	14.83	12.1	0.300	1.54						
226.529	7	7	18.18	15.19	11.9	0.302	1.54						
226.551	8	7	17.67	15.35	11.8	0.302	1.54						
226.586	9	7	19.17	16.57	11.2	0.306	1.56						
226.624	11	6	19.70	16.55	11.4	0.303	1.56						

Table 4.2.1

Aerosol Distribution Statistics and Water Uptake

Mid JD	run #	Volume:		Acc. Mode ($\mu\text{m}^3/\text{cm}^3$)	Uncertainty (%)	Dp,g (μm)	σg	Dry Run #(s)	f(RH) Run #	Total	Acc. Mode	D/Do	MMD D/Do
		RH (%)	Dp < 2.5 μm ($\mu\text{m}^3/\text{cm}^3$)							(V/Vo) ^{1/3} D/Do	(V/Vo) ^{1/3} D/Do	Uncertainty (%)	
227.559	5	7	16.39	13.57	12.5	0.305	1.55						
227.600	6	7	15.19	13.60	12.5	0.307	1.55						
227.622	7	7	14.71	12.69	12.9	0.308	1.54						
227.646	8	46	17.30	15.68	11.9	0.321	1.53	7	8	1.06	1.07	8.3	1.04
227.667	9	61	22.13	20.47	12.7	0.351	1.60	10	9	1.07	1.10		1.17
227.714	10	9	18.17	15.21	11.7	0.302	1.57						
227.747	11	77	41.31	38.69	11.8	0.424	1.80	10	11	1.31	1.37	7.8	1.41
228.472	3	8	16.37	14.53	11.9	0.310	1.58						
228.526	4	14	15.86	14.00	12.1	0.311	1.57	3	4	0.99	0.99	8.0	1.00
228.562	5	11	16.70	14.44	11.8	0.311	1.55						
228.603	6	7	16.71	14.57	11.8	0.313	1.58						
228.652	7	77	30.92	28.79	12.2	0.401	1.78	6	7	1.23	1.25	8.0	1.28
229.405	2	7	21.08	19.52	10.1	0.321	1.63						
229.436	3	73	38.47	36.51	10.7	0.404	1.76	2,4	3	1.22	1.23	6.9	1.26
229.488	4	8	21.73	19.78	10.0	0.320	1.60	2	4	1.01	1.00	6.7	1.00
229.523	5	6	24.74	22.82	9.2	0.330	1.61						
229.566	6	6	22.44	20.74	9.7	0.328	1.61						
229.605	7	6	21.29	20.27	9.7	0.330	1.62						
229.648	8	69	37.03	35.37	8.9	0.402	1.73	7	8	1.20	1.20	6.2	1.22
230.380	2	8	28.97	27.37	8.2	0.343	1.60						
230.396	3	7	28.44	27.37	8.2	0.344	1.60						
230.417	4	7	29.26	27.98	8.1	0.345	1.60						
232.522	2	8	8.32	6.02	18.8	0.323	1.80						
232.613	4	8	6.04	5.58	19.9	0.313	1.74						
233.476	2	49	7.81	6.28	19.0	0.326	1.77						
233.492	3	55	7.80	6.04	19.7	0.324	1.76						

a Data coincide with rapid change in ambient [CN]